ENERGY AND EXERGY BASED IMPACT OF AVIONICS THERMAL MANAGEMENT SYSTEMS ON TACTICAL AIRCRAFT PERFORMANCE

by

Joseph Terranova Hedspeth

A Thesis

Submitted to the Faculty of Purdue University

In Partial Fulfillment of the Requirements for the degree of

Master of Science in Mechanical Engineering

School of Mechanical Engineering

West Lafayette, Indiana

December 2020

THE PURDUE UNIVERSITY GRADUATE SCHOOL
STATEMENT OF COMMITTEE APPROVAL

Dr. Eckhard A. Groll, Co-Chair
School of Mechanical Engineering

Dr. Davide Ziviani, Co-Chair
School of Mechanical Engineering

Dr. Justin A. Weibel
School of Mechanical Engineering

Approved by:
Dr. Nicole L. Key

Dedicated to my wife Alexa, son Grant and our cat Ranger.

ACKNOWLEDGMENTS

I would like to thank my thesis committee members for providing guidance throughout this process, it would not have been possible without their valuable insight and knowledge. I would also like to thank my family for supporting my education, as well as all the colleagues that have helped me along the way to completing this work. This thesis was funded through the Naval Air Systems Command Naval Innovative Science & Engineering Basic and Applied Research program.

TABLE OF CONTENTS

LIST OF TABLES

LIST OF FIGURES

NOMENCLATURE

Acronyms

ACS	air cooling system
AFRL	Air Force Research Laboratory
ATTMO	AFRL transient thermal modeling and optimization
BAV	bleed air valve
CFC	chlorofluorocarbon
COP	coefficient of performance
ECU	environmental control unit
EES	Engineering Equation Solver
EGW	ethylene-glycol water
GPM	gallons per minute
GPS	global positioning system
GUI	graphical user interface
GWP	global warming potential
HCFO	hydrochlorofluoroolefin
HFC	hydrofluorocarbons
HFO	hydrofluoroolefin
HX	heat exchanger
LCS	liquid cooling system
LHX	liquid heat exchanger
LRSA	long range strike aircraft
MIL-HDBK	military handbook
NIST	National Institute of Standards
ODP	ozone depleting potential
PAO	polyalphaolefin
PHX	primary heat exchanger
RBC	reversed Brayton cycle
REFPROP	Reference Fluid Thermodynamic and Transport Properties Database
RPM	revolutions per minute
SAE	Society of Aeronautical Engineers
SFC	specific fuel consumption
SHX	secondary heat exchanger
TMS	thermal management system
TXV	thermostatic expansion valve
V&V	verification and validation
VCC	vapor compression cycle
VCSRF	Vapor Cycle System Research Facility

W/S	water separator

Symbols

A	area (m^2)
amp	amplitude (mm)
C	heat capacity rate (kW/K)
C_d	coefficient of drag (-)
Chan	number of flow channels (-)
C_L	coefficient of lift (-)
c_p	heat capacity at constant pressure (kJ/(kg-K))
g	gravitational constant (m/s^2)
h	specific enthalpy (kJ/kg)
height	height (m)
h_t	fin height (mm)
$\dot{I}$	exergy destroyed (kW)
k_{pwr}	power factor (-)
length	length (m)
L/D	lift-over-drag ratio (-)
L_{off}	length of fin offset (mm)
L_w	wavelength (mm)
M	Mach number (-)
m	mass (kg)
$\dot{m}$	mass flow rate (kg/s)
P	pressure (kPa)
p	fin pitch (mm)
Pass	number of flow passes (-)
P_r	pressure ratio (-)
$\dot{Q}$	heat transfer rate (W)
R	specific gas constant (J/(kg-K))
s	specific entropy (kJ/(kg-K))
SFC	specific fuel consumption (kg/(N-s))
T	temperature (^oC)
t	fin thickness (mm)
t_p	thickness of plates between fins (mm)
V	velocity (m/s)
$\dot{V}$	volumetric flow rate (m^3/s)
width	width (m)
$\dot{W}$	power (W)
β	chevron angle (rad)
γ	heat capacity ratio (-)
ε	effectiveness (-)

η	efficiency (-)
ρ	density (kg/m^3)
τ	time (s)
$\dot{\psi}$	exergy flow (W)
ψ	exergy (kJ/kg)
ω	humidity ratio (kg_{water}/kg_{air})

Subscripts

0	surroundings
1,2,3,…	state point
air	air conditions
amb	ambient
avionics	avionics
BAV	bleed air valve
bleed	bleed air
cold	cold side
comp	compressor
component	component parameter
cond	condenser
cool	cooling
dest	destroyed
ds	discharge
engine	engine conditions
evap	evaporator
ex	exergy
expend	expendable material
fo	fuel penalty
hot	hot side
HX	heat exchanger
in	inlet
inlet	inlet conditions
liq	liquid
max	maximum value
min	minimum
out	outlet
overboard	overboard the aircraft
pwr	power
PHX	primary heat exchanger
pto	power take-off
r	refrigerant
RBC	reversed Brayton cycle
rev	reversible

rhtr	reheater
s	isentropic
sat	saturation
SC	subcooling
SHX	secondary heat exchanger
sink	sink conditions
source	source conditions
suc	suction
sys	system
TH	thrust
tot, ram	ram total condition
turb	turbine
VCC	vapor compression cycle
water	water
wf	working fluid

ABSTRACT

Thermal management systems for tactical aircraft electronics cooling were studied in this work. The systems consisted of an HFC-134a based vapor compression cycle (VCC) and an air-based reversed-Brayton cycle (RBC). The heat loads consisted of aircraft electronics, including avionics. The system models were built using detailed component-level models. The models underwent verification and validation to check mass and energy conservation, as well as ensuring the model's behavior reflected the actual system's behavior. Both models were run through a matrix of boundary conditions that represented specific segments of two tactical aircraft missions with next generation thermal loads. These segments included typical tactical aircraft operating conditions: ground idle, cruise, combat, dash, and loiter. The resulting system performance of both models was analyzed using a first law energy-based fuel impact and second law exergy-based irreversibility method to determine their respective impact to the aircraft. Component level irreversibilities were also analyzed.

The VCC cooling system met or exceeded cooling performance goals, while the RBC fell short during some mission segments. The VCC also had a lower fuel impact than the RBC from an energy perspective and lower system and component level irreversibilities from an exergy perspective for most mission segments. The opposite trend was observed during the ground idle segment, where the VCC's fuel impact was larger but irreversibilities were lower than the RBC's.

The VCC's lower fuel impact was due to the engine power take-off having less of an impact on engine fuel flow than the RBC's bleed air. The VCC's lower irreversibilities were due to the system's use of phase change in the heat exchangers, which tended to be more efficient than the single-phase heat transfer in the RBC's heat exchangers.

Some limitations of the study should be addressed in future work, including electrical power generation losses and an improved air humidity model that operates better at low temperatures and incorporates moisture evaporation. Alternative VCC refrigerants with higher critical temperatures should also be explored to ensure the system does not limit the aircraft operationally. New architectures should be explored that combine RBC cooling and VCC cooling.

Overall, the VCC cooled the thermal load more efficiently with a lower overall impact to the aircraft than the RBC from both energy and exergy based perspectives.

1. INTRODUCTION

1.1 Background and Motivation

1.1.1 Tactical Aircraft Electronics Heat Loads

Electronics are vital to the operation of modern aircraft. From avionics such as inertial and global positioning system (GPS) based guidance systems, stability and control systems, and airborne radar, to electro-mechanical systems such as electro-harmonic actuators and all electric fluid pumps, electrical components are found throughout an aircraft. Since these electronics are not 100% efficient, some of the power inputted to these components is lost to waste heat. This waste heat must be removed via the aircraft's thermal management system (TMS) to prevent electronics temperatures from increasing beyond acceptable limits.

Tactical military aircrafts, such as the fourth generation F-15 Eagle, present a unique challenge for TMS' when compared to civilian commercial aircraft or military transport aircraft due to their high ram air recovery temperatures, and is caused by high Mach number operations, as well as strict size, weight and power constraints. Ram air is airflow that is induced by the moving aircraft, while the recovery temperature is the temperature rise caused by the rise in the ram air flow's pressure. Furthermore, the quantity and energy density of the aircraft electronic systems tends to increase for each new generation of tactical military aircraft as end users desire increased capability. Figure 1.1 illustrates this grown in power requirements for military aircraft from the 1940's to the 2010's.

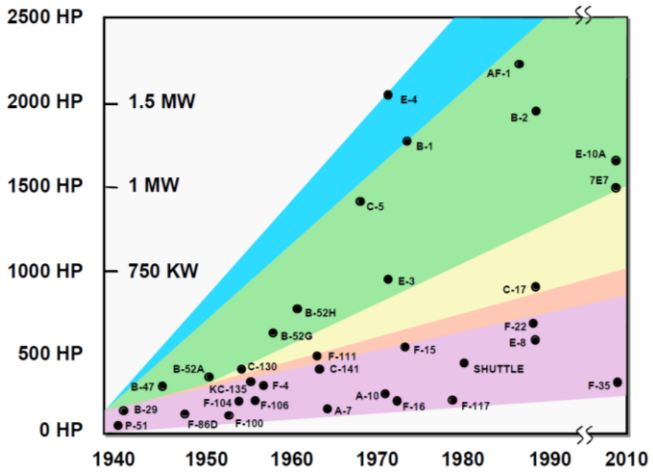

Figure 1.1. Trends in Military Aircraft Power Requirements [1]

Power electronics growth is leading to an exponential increase in heat loads for next generation tactical aircraft. Figure 1.2 demonstrates this trend by highlighting the heat loads for select third, fourth, fifth and sixth generation aircraft. In the figure, the overall aircraft heat load, which is broken down into heat loads from the various subsystems, is combined into a single fuel cooling requirement. This heat load requirement doubles between the third generation F-4 Phantom and fourth generation F-15 Eagle, increase 2.5 times for the fifth generation Advanced Fighter, and increases nearly three times for the sixth generation long range strike aircraft (LRSA).

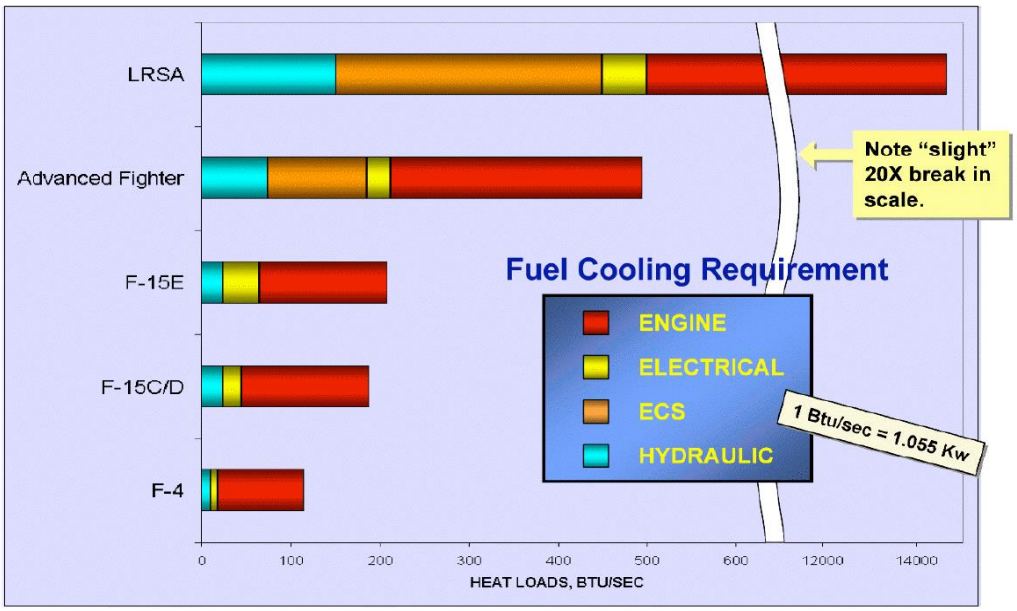

Figure 1.2. Heat Loads for Select Tactical Aircraft [1]

These heat loads can range from 100kW to 1000kW, with component heat fluxes on the order of 100 W/cm^2 to 750 W/cm^2, and can greatly exceed the thermal capacity of contemporary TMS', which are on the order of 10 kW. Furthermore, the next generation avionics and electronics that are causing these higher heat loads tend to require stringent temperature control for proper operation [2], [3], [4].

The transition from fluid based mechanical systems to electric based systems, such as hydraulic actuators to electric actuators, may also increase aircraft heat loads. This increase is two-fold since the fluids used in hydraulic systems, such as polyalphaolefin (PAO) oil, are also used to transport thermal loads and must be replaced by other transport fluids if they are removed. In addition, though electric-based systems can be more tolerant to higher temperatures than fluid-

based systems, they may also have more stringent temperature requirements than fluid based systems [5]. These increased thermal loads, which exceed the capacity of conventional TMS', lead to electronics payload limitations and can negatively affect electronics and aircraft performance [1].

Tactical aircraft TMS selection must consider these electronics growth trends to correctly size the system for next generation heat loads, as well as other factors, such as the aircraft operating conditions, to ensure the optimal system is chosen for the application.

1.1.2 Tactical Aircraft Operating Conditions

Since ram air is used as the primary heat sink for tactical aircraft TMS', the system performance is heavily influenced by both the ambient and operational conditions. At low altitudes below 3.048 km (10kft), ambient air temperatures are high, which reduces the temperature delta between the TMS and the air. Conversely, at high altitudes above 12.192 km (40kft), ambient temperatures are low, which creates a larger temperature delta between the TMS and the air than at lower altitudes. However, the air density is lower, which reduces the cooling capacity of the air [6].

High ram air temperatures that occur during tactical aircraft operations, including high speed dashes and transonic/supersonic cruise, further degrade the effectiveness of ram air as a heat sink since it reduces the temperature delta between the system and air. Coupled with low altitudes, ram air recovery temperatures can exceed specification maximums for electronics. As an example, MIL-HDBK-5400: General Guidelines for Electronic Equipment, Airborne specifies a maximum air temperature of 55^{o}C (131^{o}F) for Class 1 military electronics [7]. As seen in Figure 1.3, this temperature is exceeded at speeds as low as 0.45 Mach at sea level/0 km, around 0.65 Mach at 1.524 km (5kft), and around 0.8 Mach at 3.048 km (10kft).

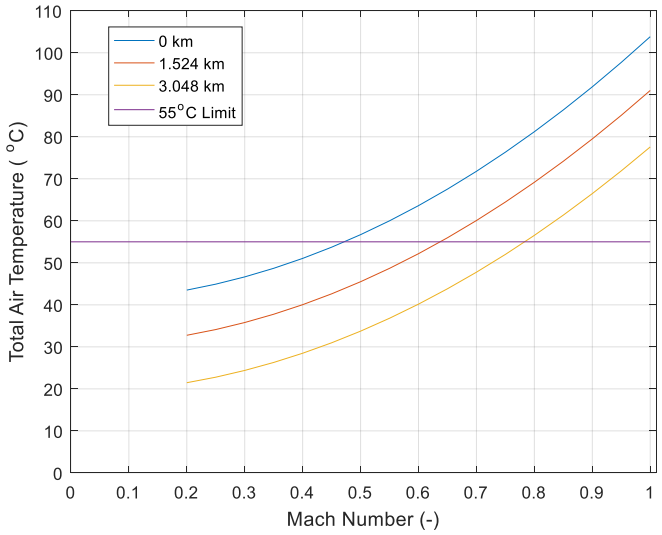

Figure 1.3. Total Air Temperature versus Mach Number at 0 km, 1.524 km (5kft) and 3.048 km (10kft)

Stationary or low speed ground operations, which occur during preflight checkout, taxiing, and ground maintenance, also impose significant demands on the aircraft TMS. Ground hot soak temperatures tend to be very high due to the low altitudes and solar loading. According to MIL-HDBK-310 Global Climatic Data for Developing Military Products, sea level temperatures can be as high as 49ºC, which corresponds to the hottest 1% of the temperatures recorded at the hottest point in the world. Even in less demanding environments, the air temperatures near the ground may be 15ºC to 30ºC higher than the ambient temperature due to the ground reradiating solar radiation [8]. Additionally, airflow rates though heat exchangers are low since the aircraft is stationary, which requires additional components to induce airflow, such as external cooling carts, electric fans, or pressure driven ejectors. Because ground operations tend to last for 30 minutes to several hours, they cannot be treated as a transient condition and the TMS must be designed to handle the load continuously [9].

1.1.3 Tactical Aircraft Thermal Management Systems Overview

The previously discussed head loads and operating conditions must be taken into account when selecting between the three main types of TMS for aircraft electronics cooling: passive/pumped systems, thermal storage systems, and active/compression systems.

Passive/pumped TMS', such as liquid cooling systems (LCS) and air cooling systems (ACS), tend to be the simplest type of TMS'. This simplicity is due to the nature of their operation, which is sensible heat transfer between the source and the sink via an intermediary working fluid without external power input to raise or lower the working fluid temperature. The only power input required for these systems is mechanical work to pump the intermediary fluid from the source and sink heat exchangers, which is in the form of fan power for ACS' or pumping power for LCS'.

One of the main drawbacks to passive TMS' is due to their simplicity. Since energy exchange in this type of system is driven by the difference between the source temperature and the sink temperature, and the power input to the system is only used to move the fluid, they can theoretically only bring the source temperature to the sink temperature. In practice, the source temperature must be higher than the sink temperature since heat exchangers tend to have lower than 100% effectiveness. These systems have limited usage on tactical aircraft since their ability to cool reduces as sink temperature increases. At the high sink temperatures that occur during high speed flight, the systems may be unable to cool if the sink temperature exceeds the maximum electronics temperature, which can be as low as 55^{o}C for MIL-HDBK-5400 Class 1 electronics [7].

Passive TMS can be enhanced by incorporating phase changes, and are known as pumped two-phase cooling loops [9]. These systems take advantage of constant temperature latent heat absorption during phase change to enhance the heat transfer in the heat exchangers. While this type of passive TMS can be more efficient than a simple passive TMS, they have similar drawbacks. This includes the sink temperature needing to be higher than source temperature since the power input is only used to move the working fluid throughout the system.

Thermal storage TMS' that utilize a thermal mass, such as fuel, tend to be time limited because the amount of energy the system can absorb is dependent on the properties of the material used as the thermal storage sink. One property of interest for fuel heat thermal storage is max allowable temperature, which changes based on the fuel's thermal stability. As an example, the recommended maximum temperature for tactical military aircraft JP-8 fuel is 163^{o}C to prevent coking on the fuel nozzle [10]. Another property is the mass of fuel that can be used for cooling, which decreases over the course of a mission as it is used by the engine. Another consideration for fuel is the mass flow rate since it is set by engine fuel consumption demands. If a higher flow rate is needed to dissipate the generated electronics heat, the fuel flow above what is needed by the

engine must be recirculated back to the fuel tanks and possibly cooled if the fuel is heated above 163^{o}C [4]. Phase change materials (PCMs) are an improvement over a thermal mass since the energy exchange occurs at a constant temperature during the phase change, which improves the efficiency of the sink. Both types of thermal storage systems have the same limitations as passive systems since the energy exchange can only occur if the source temperature is higher than the sink temperature.

Thermal storage TMS' have limited usage for tactical aircraft cooling due to their temperature limitations, as well as their time-limited and mass-dependent nature. As a result, tactical aircraft level heat loads require large amounts of material to provide cooling for extended periods. This weight increase reduces the weight of the payload the aircraft can carry since tactical aircraft tend to be highly weight limited.

Active/compression based TMS', such as vapor compression cycle (VCC) systems and Reversed Brayton Cycle (RBC) systems, provide an advantage over passive/pumped TMS' since they can bring the source outlet temperature below the sink inlet temperature. These systems operate on the principle of external power being used to raise and lower the temperature of the working fluid, which facilitates the energy exchange between the source and the sink. This energy exchange is beyond what is possible using a passive system's sensible heat transfer driven approach. However, active systems tend to be heavier, more complex, and require more power input than passive systems. These systems are commonly used for tactical aircraft cooling due to their ability to cool at the high sink temperatures that occur during high-speed flight. However, active TMS' can be limited at extremely high sink temperatures; RBC's may draw excessive amounts of bleed air and reduce engine performance, while VCC maximum temperature cannot exceed the refrigerant critical temperature (as an example, HFC-134a has a critical temperature of 101.1^{o}C) and may draw excessive amounts of power [11]. Unlike thermal storage systems, active systems can operate continuously when provided with a continuous source of input energy, which allows them to cool electronics throughout an entire mission [12].

1.1.4 Active Thermal Management System Details – Vapor Compression Cycle Refrigeration Systems

The first type of active system that will be explored are VCCs'. VCC's operate on the principle of energy input via compression and rapid expansion to increase or decrease the

temperature of a refrigerant to create the temperature difference required for energy exchange from a heat source and to a heat sink, as well as phase change in the heat exchangers to enhance heat transfer. A process diagram for a VCC is presented in Figure 1.4 and is as follows:

1. State 1 to 2 - The refrigerant exiting the evaporator is compressed in an electrically driven compressor to a superheated vapor at a pressure with a saturation temperature higher than the sink temperature to facilitate energy exchange.
2. State 2 to 3 - The refrigerant rejects heat to the sink at a constant pressure in the condenser, which results in desuperheating from a superheated vapor to a saturated vapor. After desuperheating, the refrigerant undergoes a phase change to a saturated liquid, which allows the heat to be rejected to the sink at a constant temperature and pressure. Further heat rejection results in subcooling of the refrigerant below the saturation temperature, which occurs at a constant pressure.
3. State 3 to 4 - The refrigerant undergoes expansion to a liquid/vapor mixture at a pressure with a saturation temperature lower than the heat source to facilitate energy exchange from the source to the working fluid.
4. State 4 to 1 - The two-phase refrigerant undergoes a phase change to a saturated vapor in the evaporator. During this process, heat is absorbed from the source at a constant pressure and temperature. Further heat absorption results in superheating of the refrigerant above the saturation temperature at a constant pressure. The refrigerant is then directed to the compressor to complete the cycle.

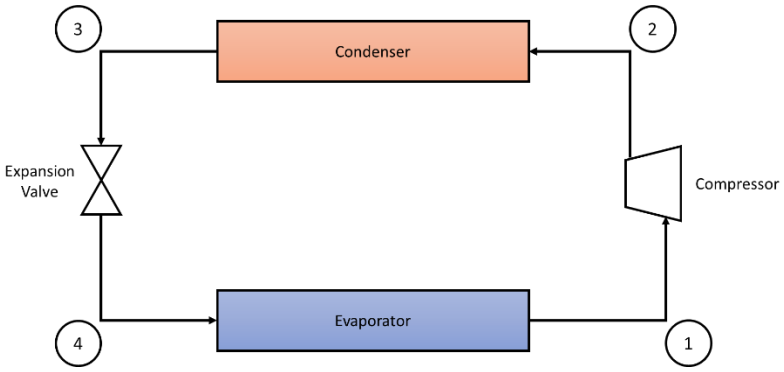

Figure 1.4. Simple VCC Process Diagram

A T-s schematic diagram for a generic VCC is presented in Figure 1.5. The dashed lines denote an ideal process with no subcooling or superheating. The solid lines shown the actual process with compressor losses, as well as an amount of subcooling and superheating.

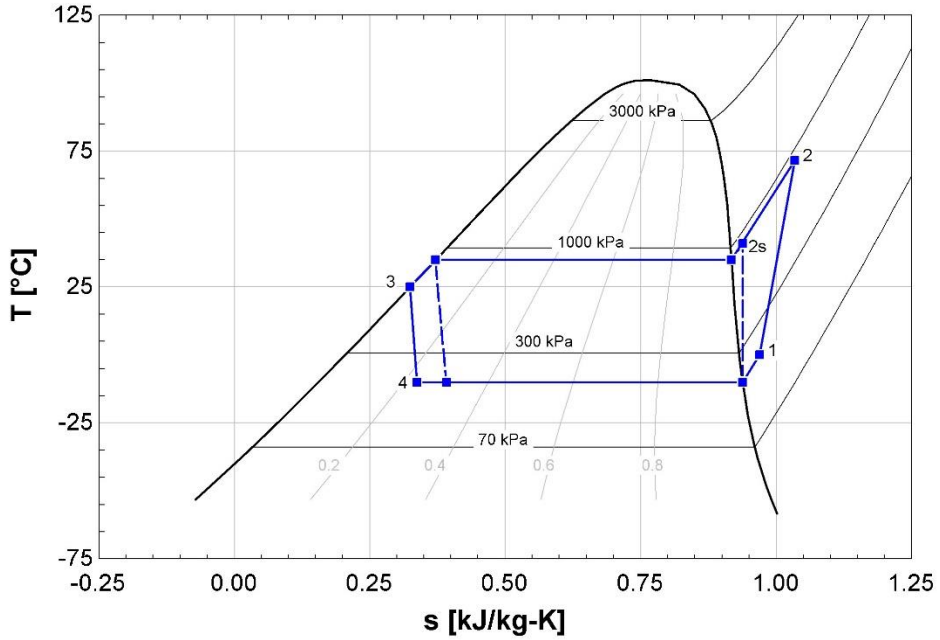

Figure 1.5. T-S Schematic Diagram of a Simple VCC

VCC refrigerant plays a significant role in cycle performance, and there are specific criteria that must be addressed when selecting a suitable refrigerant for tactical aircraft VCC's, such as thermodynamic, practical, and environmental considerations. Thermodynamic criteria include low specific volume, which corresponds with higher efficiency, high thermal conductivity to enhance heat transfer, critical temperature greater than the highest condenser sink temperatures, and high liquid and vapor density with low liquid and vapor viscosity to reduce compressor requirements and pressure drop. Practical considerations include low solubility in oil, chemical stability, no toxicity in case of a leak, minimally reactive to water, oil or other VCC or aircraft materials, nonflammable, and inexpensive [12]. Finally, environmental considerations play a role since they preclude the use of certain types of refrigerant; CFC's are banned due to their high ozone depleting potential (ODP), while HFC's are being phased out due to their high global warming potential (GWP) [13].

HFC-134a is the most commonly used refrigerant in aircraft applications since it meets most of the previously discussed thermodynamic and practical criteria and considerations [14]. However, HFC-134a is deficient in some aspects for tactical aircraft applications; it has a relatively low critical temperature of 101.1^{o}C, which can be exceeded during high Mach and low altitude

operations, and does not meet environmental considerations due to its' high GWP. Alternative low ODP/GWP VCC refrigerants that may be suitable for this application are being explored, such as HFO-1234yf, HFO-1336mzz(Z/E), HCFO-1233zd(E) and natural refrigerants such as CO_2 [3] [13]. However, this work will focus on an HFC-134a based VCC due to the availability of data to validate the system performance models

1.1.5 Active Thermal Management System Details – Reversed Brayton Cycle Refrigeration Systems

The second type of active TMS that will be explored is the RBC. An RBC refrigeration system, also known as an air cycle refrigeration system, works on a similar principle of operational to a VCC, except the air used as the working fluid does not undergo a phase change. For aircraft applications, the source of this air is the intermediate or high-pressure stages of the turbine engine's compressor and is known as engine bleed air. A RBC refrigeration cycle schematic diagram is presented in Figure 1.6 and is as follows [12] [15]:

1. State 1 to 2: Ambient air enters the engine inlet. Since the aircraft is moving, the air undergoes isentropic compression due to the ram air effect and the temperature and pressure is raised.
2. State 2 to 3: The ram air is compressed in the engine main compressor, which further increases the air's temperature and pressure.
3. State 3 to 4: A small amount of the compressor engine air is bled off for the RBC refrigeration system. This valve controls the system capacity by setting the RBC inlet air flow rate and pressure.
4. State 4 to 5: The high-pressure, high temperature engine bleed air rejects heat to the sink in the primary heat exchanger at a constant pressure.
5. State 5 to 6: The bleed air again undergoes compression in an air compressor that is mechanically linked to the expansion turbine. The air must exit the compressor at a temperature higher than the sink to facilitate heat transfer.
6. State 6 to 7: The compressed bleed air then rejects heat to the sink again in the secondary heat exchanger at a constant pressure.
7. State 7 to 8: If turbine exit temperatures are anticipated to be below freezing, entrained moisture removal is needed after the air is cooled in the secondary heat exchanger to prevent icing. Since this process occurs when the air is at the high compressor outlet pressure, it is known as high pressure water separation.
    a. As shown in Figure 1.7, the air enters the reheater heat exchanger, where it is cooled by the cooler dehumidified air

b. The cold turbine outlet air then further reduces the temperature of the air in the condenser heat exchanger. This temperature reduction condenses the moisture in the air.
c. The condensed moisture is then removed in a water collector. The water is either sent overboard or sprayed on the primary and/or secondary heat exchangers to enhance heat transfer

8. State 8 to 9: The dehumidified air then undergoes expansion in a turbine to bring the temperature lower than the source to facilitate heat transfer. The turbine and compressor are mechanically coupled, which allows the work generated during the expansion process to provide the work required for the compression process. Since the turbine powers the compressor, this specific RBC configuration is known is a “bootstrap air cycle”.
9. State 9 to 10: After expansion, the low temperature, dehumidified air is used to reduce the temperature of the moist air entering the water separation subsystem.
    a. After transferring heat in the water separation subsystem, the cold air is used to absorb energy from the source and pressurize the cabin. This heated air is then either sent overboard in an open cycle or is brought back through the air compressor in a closed cycle.

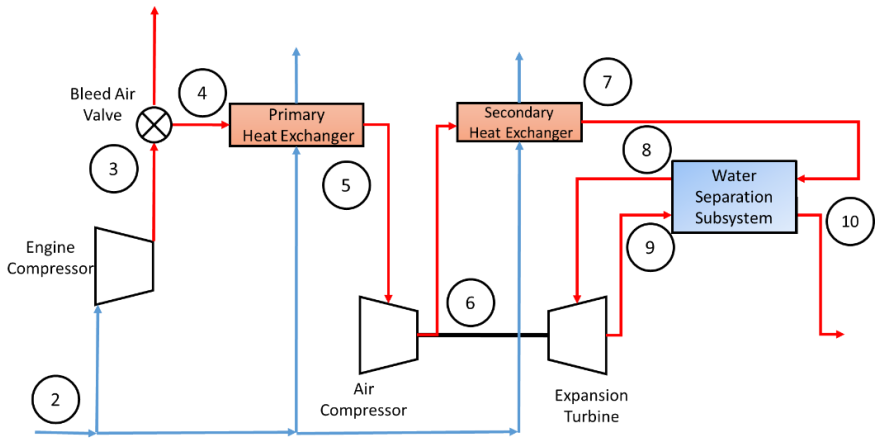

Figure 1.6. Bootstrap Air Cycle Process Diagram, Blue Represents Ram Air and Red Represents Hot Engine Air/Bleed Air

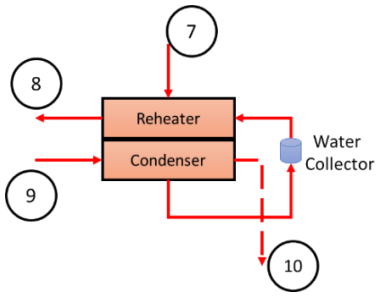

Figure 1.7. Water Separation Subsystem Details

Since this configuration has a single compressor and a single turbine on the same shaft, it is known as a “two-wheel” bootstrap air cycle system.

A T-s diagram for an open bootstrap RBC without water separation or bleed air valve capacity control is shown in Figure 1.8. The dashed lines denote an ideal isentropic process, while the solid lines shown the actual process with compression and expansion losses. Since water separation was not included, state point 7 represents the outlet of the expansion turbine.

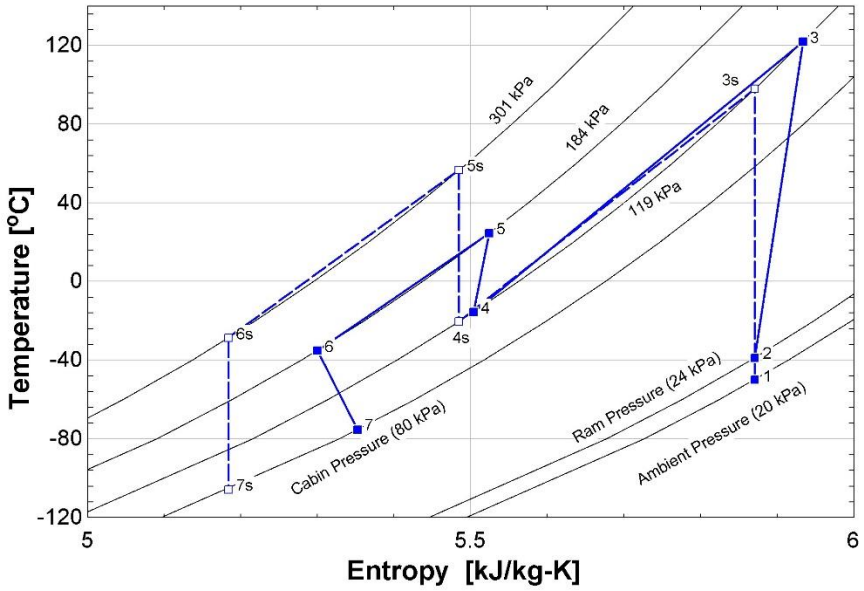

Figure 1.8. Open Bootstrap Air Cycle T-S Diagram

1.1.6 Thermal Management System Modeling

The need to cool high heat loads produced by electronics within tight temperature bounds with demanding sink conditions while simultaneously keeping within tight design constraints leads to conflicting systems requirements. In order to satisfy these requirements, careful TMS selection and optimization is necessary. As a result, quantifiable performance metrics must be generated to compare the TMSs under consideration.

The process to develop a comparison between RBC and VCC refrigeration, and each system’s impact on an aircraft involves first generating system performance data. The data is obtained from a system model that may be made up of detailed individual component models, including the heat exchangers, compressor, turbine, expansion valve, and flow lines. Component models can either be map based, or first-principles physics based, and selection of the model

depends on the application. These component models are then combined into the system model, with the components included and the connections made according to the system architecture. Once the component and system models are developed, verification and validation (V&V) at both the component level and the system level can be completed to ensure the model will provide accurate results. V&V involves demonstrating mass and energy conservation are not violated by performing mass and energy balances on each component and then on the entire system, and comparing the model results to experimental or previously validated model data.

Once the V&V process has been completed for the model, the source and sink boundary conditions can be changed to tactical aircraft relevant conditions. If the system is not properly sized for these new conditions, the component models and/or system architecture can be altered to better suit the conditions. If changes are made in the model, the V&V process must be repeated to ensure the model continues to provide accurate results. If data is not available for this new architecture, or if the source and/or sink conditions used for validation do not match the new conditions, uncertainty can be introduced in the model. However, this uncertainty can be reduced if the verification process shows the new model continues to satisfy conservation of mass and energy.

After system performance data has been generated for the RBC and VCC, the impact of each system on a fourth-generation tactical fighter can be determined by incorporating the model results into an energy and exergy based analysis.

1.1.7 Energy-Based Approach to Determining the Impact of a Thermal Management System on an Aircraft

There are a variety of quantitative methods to determine the impact of a TMS on aircraft performance. By applying these methods to a VCC and RBC for aircraft electronics cooling, a comparison can be drawn between both systems. Two methods to determine TMS impact on an aircraft during representative missions will be explored in this work, an energy-based approach and an exergy-based approach. The energy-based approach to determining the impact of a TMS incorporates a first law of thermodynamics analysis to determine the TMS' influence on the aircraft in terms of fuel weight. First, the energy required by the TMS is calculated using a performance model of the system at a specified flight condition. TMS parameters, such as heat exchanger effectiveness and turbomachinery performance, are varied in the model to determine

their impact on system energy usage. These parameters each impose a penalty on the aircraft, and are dependent on the type of system analyzed [16].

VCC systems require electrical power for the compressor. The source for this power is "take-off" power from the engine gearbox. Drawing this power creates additional load on the engine, which results in increased specific fuel consumption (SFC) to ensure thrust produced by the engine remains constant [16]. RBC systems require high-pressure air for the compressor. The source for this air is bleed air from the high-pressure or intermediate-pressure sections of the engine main compressor. Drawing this bleed air reduces thrust produced by the engine, and SFC and engine turbine temperatures must increase to account for the loss [17].

For both VCC's and RBC's, ram air is used as the primary heat sink for most tactical aircraft TMS'. This ram air usage increases the required engine thrust to compensate for the drag caused by the ram air ducts, which raises engine SFC. TMS weight also increases engine thrust requirements and SFC due to the drag produced by the weight of the system. Both the ram air and weight SFC impact are dependent on the lift-to-drag ratio of the aircraft [16].

After these SFC impacts are applied over an aircraft's entire mission profile, the total fuel weight required for the TMS at take-off can be established. The overall goal of this analysis is to minimize the TMS' impact on the aircraft's gross take-off weight [18].

1.1.8 Exergy-Based Approach to Determining the Impact of a Thermal Management System on an Aircraft

The exergy-based approach to determine the impact of a TMS incorporates a first and second law of thermodynamics analysis to determine the TMS' impact on the aircraft and is based on the "global" and "local" methods outlined by Oliveira (2013). For the global method, the exergy destroyed by the TMS is calculated via a performance model of the system at a specified flight condition. Then, the calculated losses of the TMS are summed over the aircraft's mission profile to determine the total exergy destroyed by the system. A reference point for the exergy destruction is selected based on a single static point, such as ground ambient conditions, or multiple dynamic points, such as ambient air conditions [19].

Usable energy flows into the TMS via high temperature and high pressure bleed air for an RBC, electrical power for a VCC, cool ram air, or hot avionics cooling fluid return flow. Usable energy leaves the TMS in the form of cold avionics send flow, but this flow stream is still usable

for cooling the avionics. Usable energy leaves the TMS in the form of the heated ram air flowing out of the source heat exchanger or air sent overboard after cooling, and is lost since it has no additional usage to the aircraft [20].

For the local method, the exergy destroyed by the TMS is broken down to the component level to determine the largest generator of entropy. Entropy generation in an RBC is caused by inefficiencies in the compressor and turbine, mechanical losses in the coupling between the compressor and turbine, nonreversible heat transfer in the heat exchangers, and pressure drop in the pipes, valves, and heat exchangers. Entropy generation in a VCC is caused by inefficiencies in the compressor, throttling losses in the expansion valve, nonreversible heat transfer in the condenser and evaporator and pressure drop in the pipes, valves and heat exchangers [21]. These component level losses can be used to find potential areas of optimization by determining the components that cause the most amount of exergy destruction in subsystem.

The overall goal of both the global and local exergy-based methods is to minimize the exergy destruction term, which minimizes the energy wasted. Minimizing wasted energy reduces the excess fuel required by the aircraft to overcome the TMS' inefficiencies [18].

1.2 Objective

The objective of this work is to evaluate the energy performance of a direct expansion vapor compression cycle refrigeration system for tactical aircraft electronics cooling using a detailed component-level modeling approach. The results of this model will be compared to the results of a reversed Brayton cycle refrigeration system using an energy-based and exergy-based analysis to determine each systems' impact on a fourth generation tactical aircraft.

1.3 Overview

Chapter 2 presents a literature review of active TMS' usage in cooling aircraft electronics and previous studies using energy and exergy based methods to assess aircraft systems.

Chapter 3 covers the methods used to develop the system models, as well the energy and exergy based methods' correlations that relate TMS performance to aircraft impact for comparison purposes.

Chapter 4 describes verification and validation of the TMS models, presents the impact data for the comparison by applying aircraft relevant boundary conditions to the validated system models, and discusses the RBC and VCC modeling and simulation effort results, the system comparison results.

Chapter 5 covers the conclusions of the study and recommendations for future work

2. LITERATURE REVIEW

2.1 Qualitative Comparison of Vapor Compression Cycle and Reversed-Brayton Cycle Systems

A qualitative comparison can be made between a VCC and RBC for aircraft cooling applications based on the characteristics of the respective systems. Patel et al., (2010) [22] discuss the ability of VCC's to increase the temperature differential between the refrigerant and heat sink in the condenser via additional work input to the compressor. They also contend that VCC's have an additional advantage over other types of TMS' due to the constant temperature phase changes in the heat exchangers. This constant temperature heat transfer produces a higher overall temperature differential when compared to the constantly decreasing temperature differential that occurs in passive and RBC system heat exchangers. Coupled with large heat fluxes that are produced during the phase changes, VCC's can use smaller heat exchangers when compared to RBC systems. However, the cost of these smaller heat exchangers is increased engine SFC since the additional compressor work input originates from power produced by the engine. The SFC per unit of power drawn depends on the engine and gearbox, but general correlations can be drawn for turbofan engines [23].

RBC's have the ability to decrease ram air heat exchanger size by increasing heat exchanger hot side temperature, but at the cost of increased bleed air flow since the compression ratio is dependent on the flow rate. This increase in bleed flow can affect engine performance. Evans (1991) [17] explored the impact of bleed air draw on the F-15 F100 turbofan engine's performance. The study found that engine turbine inlet temperature increased by around 11.1^{o}C (20^{o}F) per percent of compressor airflow drawn for bleed air, engine compressor pressure decreased by 15% at 2.6% bleed flow and engine SFC increased by as much as 1.5% for each percent of bleed flow. Higher engine turbine inlet temperatures increase wear and decrease engine life, lower pressure decreases net engine net thrust, and increased SFC requires the aircraft to carry additional fuel.

Homitz et al. [2] compared the scalability of various cooling systems, and concluded that VCC's tended to scale more effectively by having a lower volume, weight, and required power than passive TMS' and RBC's for a similar sized heat load due to the previously discussed heat transfer differences.

A disadvantage to VCC systems for tactical aircraft applications is that they have increased design difficulty over RBC systems related to the complexities brought on by phase changes. In a study to enhance VCC stability Chen et al. (2012) discuss some of the difficulties in working with two-phase TMS. These difficulties included evaporator dry out causing increased source temperatures and compressor liquid ingestion causing damage to the component. These issues are caused by oscillations in the system and transient operations, both of which are possible in a tactical aircraft with changing ambient conditions and heat loads [24]. Since RBC heat exchangers are single phase, there is no risk of dry out if the heat load suddenly changes. System transients are also a concern in RBC's due to the risk of flow surging and compressor stall. Additionally, Scaringe and Grzyll (1999) [9] discuss the system controls needed to operate VCC's off the design point to control system pressures. These controls tend to be more complex than RBC's, which only require bleed air flow valve and outlet temperature mixing valve control for traditional systems [9]. The study also includes a discussion of the critical temperature limitation of VCC's; the highest condenser temperature should be lower than the refrigerant critical temperature. Since tactical aircraft tend to operate at high ram air temperatures, the available refrigerant options are limited. RBC's do not have this concern since they use air as the working fluid and do not rely on phase change.

2.2 Previous Aircraft Thermal Management System Comparison Study – Energy-Based Method

Lui et al. [25] performed a comparative TMS study using an energy-based approach to increase the cooling capacity for the integration of a new radar on a tactical aircraft. The new radar's heat load was four times higher than the previous radar, increasing to 19kW in flight and 5kW on the ground, and had more stringent coolant inlet temperature requirements of 27 ± 3^{o}C. The TMS' options in the study were expanding the capacity of the aircraft's existing RBC and fuel cooling system, adding a VCC, adding an additional dedicated RBC system, or integrating the radar LCS with the existing RBC system. The study imposed a limitation that no additional ram air could be used for cooling, which restricted the VCC to sink to the fuel loop and limited its' capacity to 13kW. After sizing the four TMS' and modeling performance, the integrated ECS/LCS was selected since it had the lowest weight penalty on the aircraft while at the same time minimizing bleed demands. The VCC had the highest weight impact to the aircraft due to the

inefficient compressor selected, as well as the additional power and coolant loops required. Expanding the aircraft's existing cooling capacity had the lowest weight impact, but created excessive bleed air demands. The additional dedicated RBC system also coincided with excessive bleed air demands [25].

The heat loads in this study were relatively low, which is favorable towards RBC versus VCC systems as discussed by Zimmerman and Robinson [26]. Furthermore, since the study is focused on enhancing the TMS on an existing aircraft, it favored integration due to the limitations imposed on the TMS'. For example, requiring the VCC to sink to the fuel system limits system design trades that may reduce system impact on the aircraft, such as raising compressor power draw to increase condenser temperature and reduce sink heat exchanger size. Instead, system impact was highly depended on compressor efficiency alone [25].

2.3 Previous Aircraft Thermal Management System Comparison Study – Exergy-Based Method

Oliveira [19] covers multiple studies of exergy-based analyses for aircraft systems. The first study is for an exergy-based analysis of a commercial aircraft turbofan engine. The study is broken into two sections, a "global" analysis and a "local" analysis and the exergy reference point is either ground conditions or engine based air stagnation conditions. The global analysis considers the exergy flowing into and out of the engine to determine the total exergy destroyed at each flight condition, while the local analysis takes a more detailed look at the engine to determine how the total exergy destroyed is broken down at the component level. The results of the global analysis showed that the engine exergy efficiency was lowest at takeoff and landing, and was highest during cruise, which is the longest flight condition and the engine design point. The study also found that exergy lost from the air exiting the engine was greater than the exergy destroyed by the irreversibilities in the engine, suggesting that the efficiency could be improved by making better use of the air's usable energy before it leaves the engine.

The second study Oliveira [19] discusses covered a total aircraft analysis of multiple interdependent subsystems. These subsystems included the airframe, engine, bleed system, electric system, hydraulic and flight control (FC) systems, anti-ice, environmental control unit (ECU) and cabin. Each subsystem was modeled to capture the interdependencies between the systems, such as the effect of the ECU's bleed air demand on the engine's fuel flow rate. The aircraft model was

exercised over mission with multiple flight phases. The results of the analysis showed that the engine was the largest source of irreversibilities; at cruise the engine contributed 98.18% of the total, followed by the bleed system at 0.88%, the ECU at 0.66%, and the cabin at 0.28%. The study concluded that while the engine was the largest source of irreversibilities, the losses may be exacerbated by the fuel penalties the other subsystems impose on the engine, meaning improvements in the subsystems may reduce the exergy losses in the engine. It also concluded that exergy based evaluation can be used to compare aircraft with varying missions and architecture because the resulting exergy destruction term is a universal performance metric.

Pellegrini et al [20] performed an exergy based analysis of a TMS for a commercial aircraft to compare the performance of a conventional bleed driven RBC and electrically driven RBC at a single flight condition. The bleed driven system destroyed more exergy when compared to the electrically driven system since the former requires high exergy bleed air to function. The study concluded that even though the electrically driven system only decreased aircraft fuel consumption by 12%, it made better use of the available energy than the bleed driven system. The paper recommended including additional factors in future studies, such as the weight difference between the systems and an integrated aircraft model, to determine the overall impact to the aircraft fuel consumption.

In addition to comparing the performance of the systems, Pellegrini et al. [20] also examined the exergy destroyed by each individual component to determine which components contributed the most to the exergy destroyed by the system. For the conventional bleed driven system, the greatest source of losses was the bleed air system at 29%, followed by the primary heat exchanger at 17.8% and the mixing valve at 12.5%. Conversely, for the electric system, the losses were largest in the primary heat exchanger at 23.3%, the electric compressor at 12.0%, and the mixing valve at 16.5%. These results show that the bleed system is the largest source of losses when comparing both systems, and removing this component can reduce the total exergy destroyed by the system.

2.4 Assessment of Energy and Exergy Based Approaches

Figliola et al. [18] applied both an energy and exergy based analysis to the optimization of a TMS for a tactical aircraft and compared the results. The study used a simple component based TMS model that incorporated liquid loops to transport heat, a CFC-12 VCC, RBC, and a fuel system. The energy-based method was based on the aircraft impact approach covered in SAE

AIR1168-8 [16]. The exergy-based method was based on numerous previous studies and included a component non-dimensional exergy generation number. This number normalized the entropy generation rate based on both heat transfer and pressure drop related losses. The results of the study showed that both methods produced similar solutions, with the resulting weight only varying by around 8%. The study concluded that the optimal TMS design minimized both energy usage and entropy generation, but stressed the importance of reducing uncertainty when using the latter exergy-based method.

An interesting observation discussed by the study was that optimization for the exergy-based method was simpler than the energy-based method. Since the entropy term can be compared at both a component level and overall aircraft level, the exergy method shows an optimal solution and the operating point for each component that contributes to this solution. Conversely in the energy based-method, the component performance translates directly to the overall aircraft impact. As a result, the individual component performance results, such as pressure drop, power input, and heat transfer rate, cannot be directly compared and selection of an optimal solution requires background knowledge for each component.

3. RESEARCH METHODOLOGY

3.1 Thermal Management System Performance Modeling Overview

TMS performance modeling takes a variety of forms, and the complexity of the model depends on the level of detail required. For active TMS the simplest method involves assuming a constant coefficient of performance (COP), which is defined in Eq. (3-1)

$$COP = \frac{\dot{Q}_{cool}}{\dot{W}_{pwr,in}} \tag{3-1}$$

Since the COP and heat load are known, the power input can be determined. This method can be used as a preliminary analysis of an active TMS, but is too simplified to draw conclusions about the system's effectiveness. Furthermore, COP is highly dependent on source and sink conditions, as well as the system itself and is not constant throughout the operating envelope.

Some limitations of the COP method can be addressed by estimating the required system power input instead assuming a fixed COP. This method involves building a simplified system model that has assumed performance parameters for each component.

Heat exchanger effectiveness ε_{HX} is set to an assumed fixed value, and heat transfer is determined using Eq. (3-2).

$$\dot{Q}_{HX} = \varepsilon_{HX} * C_{min} * \left(T_{hot,in} - T_{cold,in}\right) \tag{3-2}$$

where C_{min} is the minimum of $\left(\dot{m}_{hot} * c_{p,hot}\right)$ and $(\dot{m}_{cold} * c_{p,cold})$. Once $\dot{Q}_{HX}$ is known, the outlet temperatures of the hot and cold fluid can be determined using Eqs. (3-3) and (3-4) respectively.

$$h_{hot,out} = h_{hot,in} - \frac{\dot{Q}_{HX}}{\dot{m}_{hot}} \tag{3-3}$$

$$h_{cold,out} = h_{cold,in} + \frac{\dot{Q}_{HX}}{\dot{m}_{cold}} \tag{3-4}$$

or Eqs. (3-5) and (3-6)for constant specific heat capacity:

$$T_{hot,out} = T_{hot,in} - \frac{\dot{Q}_{HX}}{\dot{m}_{hot} * c_{p,hot}} \tag{3-5}$$

$$T_{cold,out} = T_{cold,in} + \frac{\dot{Q}_{HX}}{\dot{m}_{cold} * c_{p,cold}} \tag{3-6}$$

A fixed pressure drop can be included for the heat exchangers and pipes to incorporate additional losses. The turbine isentropic efficiency is set to an assumed fixed value, and the work produced by the component is calculated using Eq. (3-7).

$$\dot{W}_{turb} = \dot{m}_{wf} * \left(h_{turb,in} - h_{turb,out}\right) \tag{3-7}$$

where the outlet specific enthalpy is defined using the turbine isentropic efficiency η_{turb}:

$$\eta_{turb} = \frac{h_{turb,in} - h_{turb,out}}{h_{turb.in} - h_{turb,out,s}} \tag{3-8}$$

Similar for a compressor, the isentropic efficiency is also set to an assumed fixed value and the work required is calculated using Eq. (3-9):

$$\dot{W}_{comp} = \dot{m}_{wf} * \left(h_{comp,out} - h_{comp,in}\right) \tag{3-9}$$

where the outlet specific enthalpy is defined using the compressor isentropic efficiency η_{comp}:

$$\eta_{comp} = \frac{h_{comp,out,s} - h_{comp,in}}{h_{comp,out} - h_{comp,in}} \tag{3-10}$$

Valves are assumed to exhibit ideal behavior and are correctly sized for the application, such as providing sufficient condenser superheating in a VCC or sufficient bleed air mass flow in an RBC.

Once performance is determined for each component, VCC compressor work and evaporator heat transfer or RBC compression work and sink heat transfer can be inputted into Eq. (3-1) to determine system COP.

This simple thermodynamics-based approach allows additional details to be used for the analysis, such as specific working fluids, and takes into account the inefficiencies in the system components. However, the analysis still assumes component performance is fixed, which may not be realistic since performance can vary depending on the operating parameters, inlet conditions, or outlet conditions. This method also assumes a simplified heat transfer model in the heat exchangers, and does not take into account the specifics of the heat transfer, such as phase change, or the geometry of the heat exchangers. Deficiencies in the simple component-level method can be addressed by building detailed models for each component in the system [27].

A detailed component-based system model provides a realistic method to quantify the performance of a VCC or RBC TMS. The component models take the place of the assumed values from the simple method, such as heat exchanger effectiveness and pressure drop, turbine and compressor efficiency, valve discharge coefficient, and pipe pressure drop. The type of component model varies depending on the specific type of analysis chosen, but generally is based on either first principle physics models or maps.

First principles physics models simulate the physical phenomenon occurring in the component. Heat exchanger models incorporate correlations to calculate the heat exchanger effectiveness from Eq. (3-2) and pressure drop. The model takes into account fluid properties, phase changes and component geometry [28]. Turbomachinery models use correlations to calculate efficiency from Eqs. (3-8) and (3-9) based on fluid properties and geometry [29]. Map based models incorporate lookup tables that input component inlet conditions, and output the required parameters. These tables are generated using either experimental data or the first principles physics models.

Selection of physics based or map-based component models depends on the application. Map based models are faster for small data sets and accurate if the input conditions are well captured by the data. However, map-based models can be slow for multivariable inputs and lookup tables made of large sets of data. Map-based models may also struggle with dynamics and "corner cases" where extrapolation is needed if conditions are outside the range of the table data. The accuracy of map-based models is dependent on the data used to generate the tables as well as the type of interpolation used if input conditions do not exactly match table data.

Physics based models may be faster than multivariable lookup tables of large sets of data if the model is simple. Additionally, physics-based models are better suited to capture dynamic behavior and do not require interpolation or extrapolation. However, physics based models may be slower than map based models depending on the number of calculations required to model the phenomenon, are dependent on the accuracy of the correlations in modeling the physical phenomenon occurring the component, and may require checks to ensure the correlations are valid for the component operating conditions [30].

The physics-based component models used in the thesis were indivudually built based on the results of simplified system models. The state points from the simple model were inputted into the

modeling software. The component physical parameters and heat transfer correlations were customized to produce specific component performance.

3.2 Thermal Management System Boundary Conditions

3.2.1 Model Validation Boundary Conditions

For the VCC model validation, the validation data were obtained from the Air Force Research Laboratory's (AFRL) Vapor Cycle System Research Facility (VCSRF). The heat sink was 75%/25% propylene glycol-water mixture cooled by a 60 kW chiller with a variable liquid flow rate. The pump flow rate was controlled to keep the condenser at a 51.67 ^{o}C (125 ^{o}F) saturation temperature.

The heat sources are two independently controlled polyalphaolefin (PAO) oil loops, each heated by a 12 kW inline heater. Liquid flow rate was fixed at 5.68E-4 m^3/s (9 GPM), and the heat load for each loop was varied according Figure 3.1. The actual measured heat loads into the source were 12.6 kW and 12.7 kW for loop one and loop two due to additional heat added by the pumps.

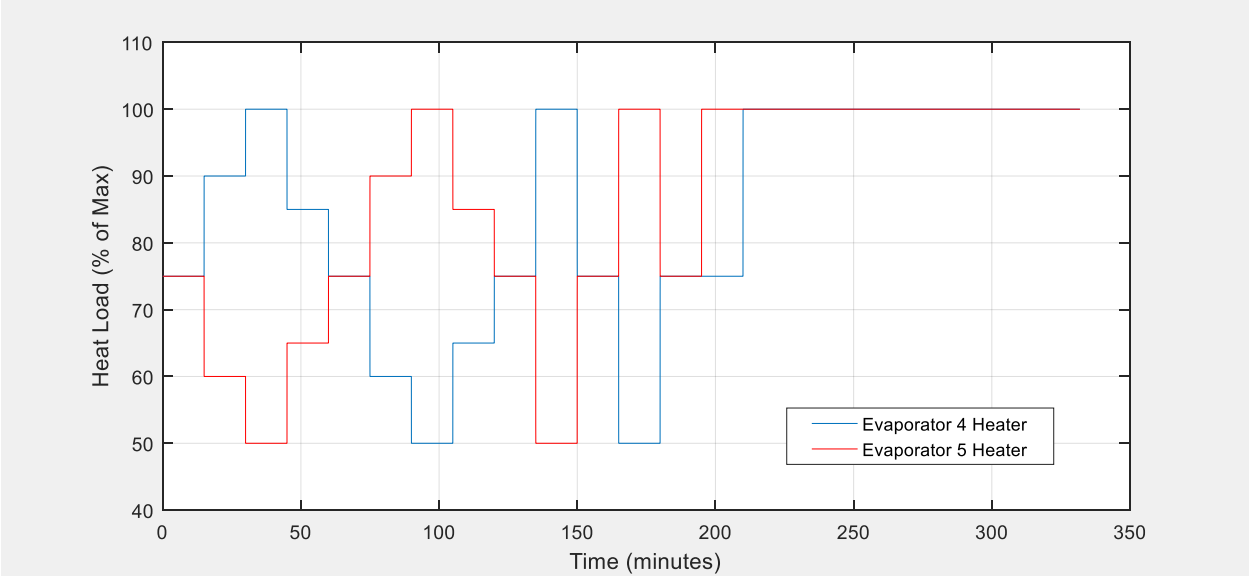

Figure 3.1. Evaporator Four and Five Heater Control Plot

For the RBC model V&V, the data were obtained from a fourth generation tactical aircraft RBC TMS. The heat sink was ram air, and the boundary conditions were generated using methods that will be discussed in the next section. The avionics in the system that generated the RBC V&V

data were direct impingement cooled and the system was open loop. As a result, the RBC cooling capacity was estimated using Eq. 3-11.

$$\dot{Q}_{cool,RBC} = \dot{m}_{RBC,out} * C_{p,air} * \left(T_{max} - T_{RBC,out}\right) \tag{3-11}$$

where $\dot{m}_{RBC,out}$ is the mass flow rate of the air at the outlet of the RBC, T_{max} is the maximum allowable avionics temperature and was set to 71°C for the V&V model, and $T_{RBC,out}$ is the air temperature at the outlet of the RBC.

3.2.2 Tactical Aircraft Model Boundary Conditions

For the tactical aircraft models, the heat sink was assumed to be ram air. The boundary conditions for the RBC and VCC refrigeration system comparison were selected based the tactical aircraft envelope shown in Figure 3.2 and the MIL-HDBK-310 20% hot day conditions in Table 3.1. The flight envelope extends from an altitude of 0 to 12.192 km (40 kft) and airspeed of 0 to 1.0 Mach. The minimum airspeed at specified altitudes is based on the F-16 tactical aircraft flight envelope, as discussed in [6]. The point at zero altitude and Mach number represents stationary ground operations.

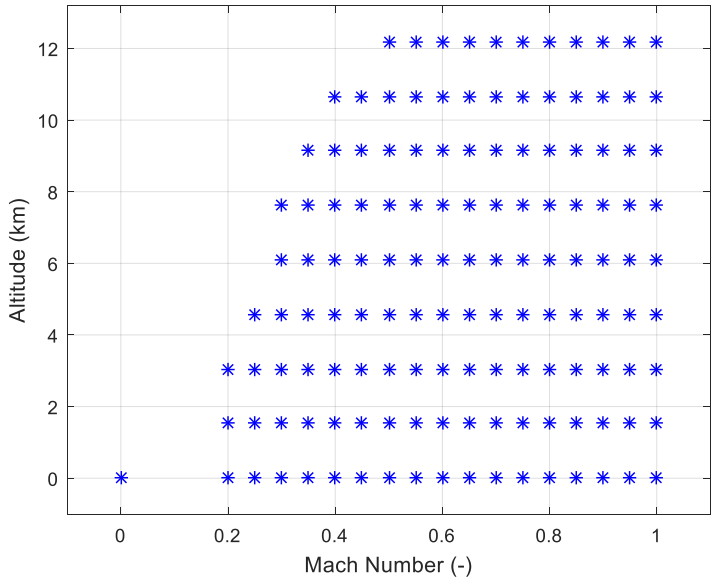

Figure 3.2. Tactical Aircraft Flight Envelope

Table 3.1. MIL-HDBK-310 20% Hot Day Ambient Conditions

Altitude, km (kft)	**T_{amb}, °C**	**P_{amb}, kPa**	**ρ_{amb}, kg/m^3**
0 (0)	41.00	101.33	1.225
1.524 (5)	30.33	84.31	1.056
3.048 (10)	19.13	69.68	0.905
4.572 (15)	8.55	57.18	0.771
6.096 (20)	-0.56	46.56	0.653
7.620 (25)	-8.96	37.60	0.549
9.144 (30)	-16.21	30.09	0.458
10.668 (35)	-23.77	23.84	0.380
12.192 (40)	-31.97	18.75	0.302

The total air temperatures shown in Figure 3.3 were obtained from the ambient temperatures at the corresponding altitudes from the flight envelope at MIL-HDBK-310 20% hot day conditions. Total air temperatures were calculated using Eq. (3-12), which assumes the ram air compresses isentropically, acts as a calorically perfect ideal gas, has a constant specific heat ratio γ of 1.4 and is fully stagnant [31].

$$T_{tot,ram} = T_{amb} * \left[1 + \frac{\gamma - 1}{2} * M^2\right] \tag{3-12}$$

where T_{amb} is in Kelvin.

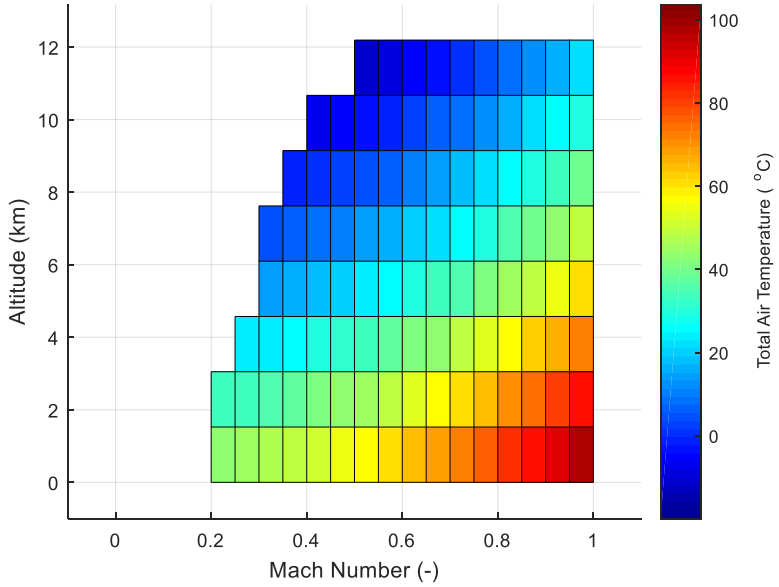

Figure 3.3. Total Air Temperatures at various Mach Numbers and Altitudes

As shown in Figure 3.4, Mach number was limited to 0.8 Mach at 0 km and at 0.9 Mach at 1.524 km (5 kft) to keep the maximum ram air total temperature below 81 ^{o}C, which provides 20 ^{o}C of margin from the 101.1^{o}C HFC-134a critical temperature. This margin allows for condenser subcooling and accounts for less than 100% condenser effectiveness.

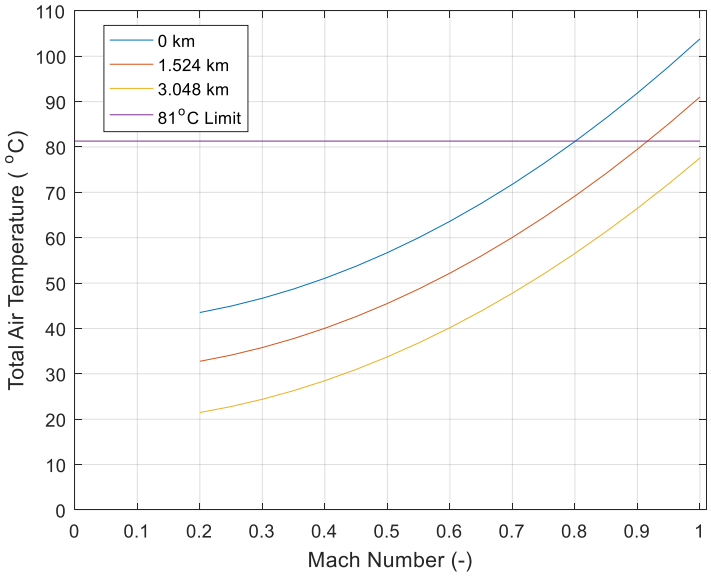

Figure 3.4. Total Air Temperature at 0 km, 1.524 km, and 3.048 km with 81^{o}C Air Temperature Limit

The final resulting flight envelope, taking into account maximum allowable temperature, is shown in Figure 3.5.

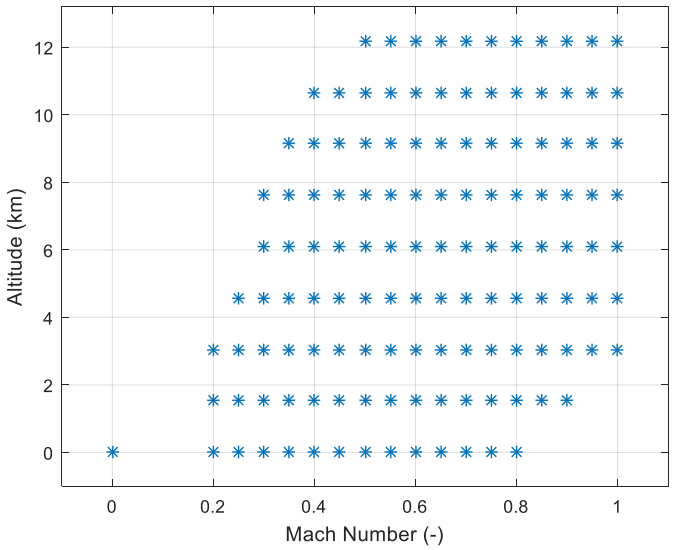

Figure 3.5. Tactical Aircraft Flight Envelope with High Temperature Limitations

Two tactical aircraft missions were developed based on example missions proposed by Raymer [32] to cover the majority of the envelope. The first mission, Air Superiority, includes high altitude cruise, mid altitude combat, and a single loiter section and is shown in Figure 3.6. The second mission, Low-Level Strike, includes mid-level cruise, low-level dash, and two loiter sections and is shown in Figure 3.7.

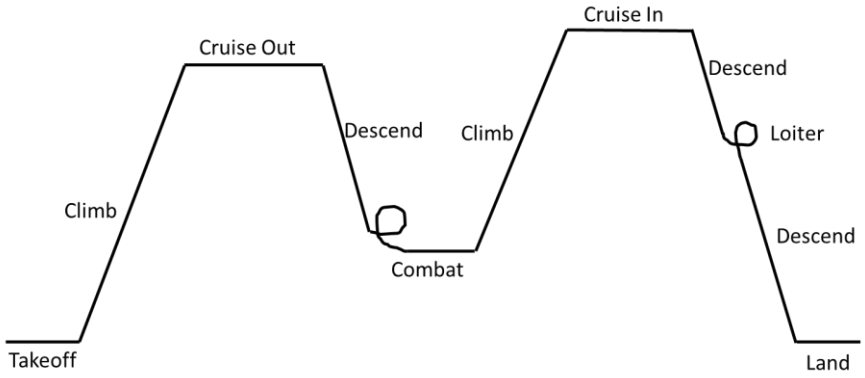

Figure 3.6. Air Superiority Mission

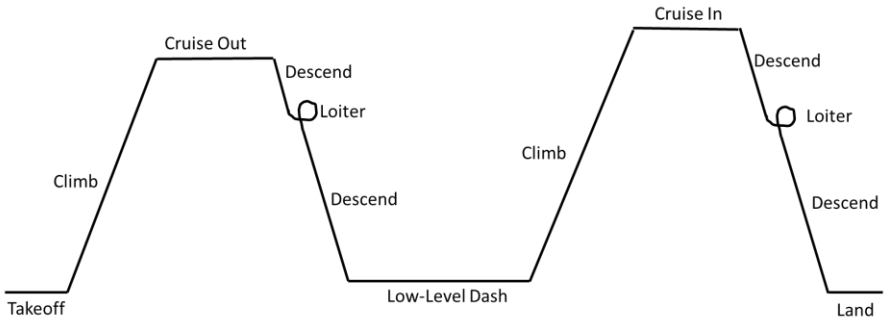

Figure 3.7. Low-Level Strike Mission

Run matrices of TMS boundary conditions were then developed based on the two missions and limited envelope from Figure 3.5 and are shown in Table 3.2 and Table 3.3 for missions one and two respectively. Takeoff, landing, climb and descend were not included in the analysis due to the transient nature of these points and the F-15's high rate of climb of 250 m/s, which allows it to ascend from 0 to 10.668 km in around 43 seconds. Times for the cruise and dash sections were calculated using the Mach number and suggested distances from the example missions. Loiter time was assumed to be 20-30 minutes and combat time was assumed to be 10 minutes [33].

Heat load for each section was varied by assuming each section had a specific percentage of the 150kW maximum heat load, assuming a 50kW minimum heat load. Heat loads were selected by assuming the percentage of the maximum heat load is similar to historical data. The heat load was not set to a fixed boundary condition, and was instead a goal since it refers to a specified source liquid flow rate and inlet temperature of 55°C, with a goal outlet temperature of 20°C.

Table 3.2. Mission 1 Run Matrix.

Section Number	Section Name	Mach Number (-)	Altitude (km)	Distance (km)	Time (Minutes)	$\dot{Q}_{cool}$ (kW)
1	Ground Idle	0	0	n/a	30.00	50
2	Cruise Out	0.85	10.668	463	26.68	100
3	Combat	1.00	6.096	n/a	10.00	150
4	Cruise In	0.85	12.192	463	26.68	100
5	Loiter	0.60	7.620	n/a	20.00	75

Table 3.3. Mission 2 Run Matrix

Section Number	Section Name	Mach Number (-)	Altitude (km)	Distance (km)	Time (Minutes)	$\dot{Q}_{cool}$ (kW)
1	Ground Idle	0	0	n/a	30.00	50
2	Cruise Out	0.85	9.144	926	53.37	100
3	Loiter	0.60	7.620	n/a	30.00	125
4	Low-Level Dash	0.75	0.100	185.2	12.10	150
5	Cruise In	0.85	9.144	926	53.37	100
6	Loiter	0.60	7.620	n/a	20.00	75

Ram air mass flow rate at each point was calculated using Eq. (3-13). This equation assumes the ram air acts as an ideal compressible gas, the flow is not chocked (velocity is less than one Mach), and has a specific gas constant of 287.058 J/(kg-K) [34]

$$\dot{m}_{ram} = \frac{A_{inlet} * P_{tot,ram}}{\sqrt{T_{tot,ram}}} \sqrt{\frac{\gamma}{R_{air}}} * M * \left(1 + \frac{\gamma - 1}{2} * M^2\right)^{-\frac{\gamma+1}{2(\gamma-1)}} \quad (3\text{-}13)$$

where $P_{tot,ram}$ is calculated using Eq. (3-14) with similar assumptions to Eq. (3-12).

$$P_{tot,ram} = P_{amb} * [1 + 0.2 * M^2]^{\frac{\gamma}{\gamma-1}} * \eta_{inlet} \quad (3\text{-}14)$$

where η_{inlet} is the inlet efficiency factor, and was set to 0.9 based on tactical aircraft inlet data.

The inlet area A_{inlet} was calculated by determining the minimum ram air mass flow rate required at the worst case air temperature design point (0.75 Mach at 0.1km, maximum heat load), and solving Eq. (3-13) for A_{inlet} as follows:

$$A_{inlet} = \frac{\dot{m}_{ram} * \sqrt{T_{total,ram}}}{P_{total,ram} * M} \sqrt{\frac{R_{air}}{\gamma}} \left(1 + \frac{\gamma - 1}{2} * M^2\right)^{\frac{\gamma+1}{2(\gamma-1)}} \quad (3\text{-}15)$$

For the tactical aircraft models, the heat source is a liquid cooled avionics loop. Ethylene glycol-water (EGW) at 60%/40% ratio by weight was selected as the coolant, which is commonly used in aircraft applications due to the low freeze point of -48.3 ^{o}C (-54.9 ^{o}F) [35]. The heat source inlet temperature was set to 55 ^{o}C, which is the maximum allowable electronics outlet temperature for MIL-HDBK-5400 Class 1A electronics [7]. The heat source outlet temperature goal for system control purposes was set to 20 ^{o}C.

The heat source flow rate was selected to provide between 50 kW to 150 kW of heat load at the 55 ^{o}C source inlet and 20 ^{o}C source outlet temperatures. These heat loads were chosen based on previously conducted studies, such as in Barta et al. [3], which assumed the next generation electronics cooling load may be as high as 150 kW. Whereas, Zimmerman and Robinson [26] used 100kW as the maximum heat load for future cooling loads. The resulting coolant flow rate ranges from 0.470 kg/s to 1.409 kg/s to account for the 50 kW to 150 kW electronics heat loads, assuming the minimum specific heat of 3.041 kJ/(kg-K) for the 60/40 EGW mix at 20^{o}C. These mass flow rates are approximately equal to volumetric flow rates of 4.271E-4 m^3/m to 0.0768 m^3/min (6.770 gal./min to 20.29 gal./min.), assuming a density of 1100.5 kg/m3 for the 60/40 EGW mix at 20^{o}C [35].

3.3 Detailed Vapor Compression Cycle Thermal Management System Model

The VCC model was built in MATLAB/Simulink using the PC Krause AFRL (Air Force Research Laboratory) Transient Thermal Modeling and Optimization (ATTMO) toolset. This toolset was developed to perform both steady state and dynamic analysis of aircraft thermal management, fuel, and electrical subsystems. It utilizes both first-principles physics based and

mapped based component models, and includes an algorithm that can size the component models for a specific design condition [30].

The VCC performance models were developed, verified and validated using HFC-134a refrigerant as the working fluid. The property data for these fluids was obtained from the National Institute of Standards (NIST) Reference Fluid Thermodynamic and Transport Properties Database (REFPROP) software converted to lookup tables [36].

3.3.1 Vapor Compression Cycle System Model Architecture

The architecture for the VCC V&V model is shown in Figure 3.8 and was a direct expansion cycle with one stage of compression and two parallel evaporators, each with an expansion valve and back pressure control valve.

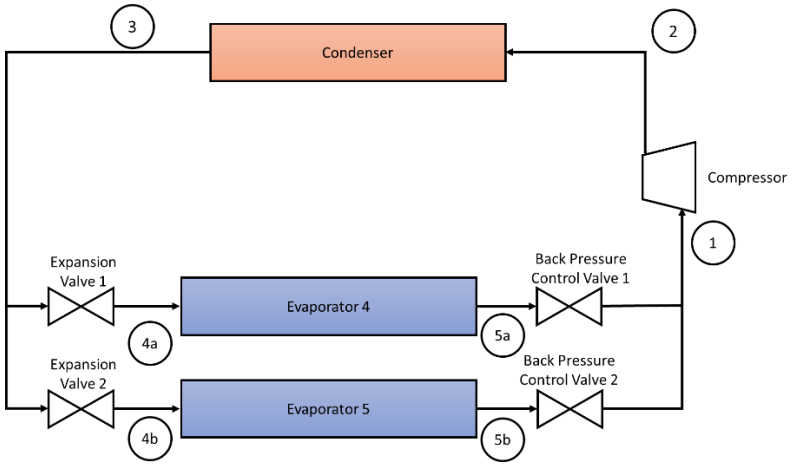

Figure 3.8. Vapor Compression Cycle Architecture for Model Verification and Validation

The architecture chosen for the VCC tactical aircraft study, shown in Figure 3.9, was a direct expansion cycle with two stages of compression and a hot gas bypass.

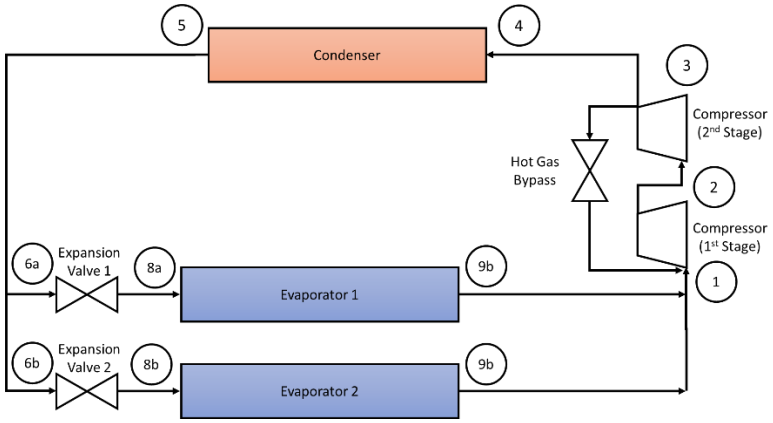

Figure 3.9. Vapor Compression Cycle Architecture for Tactical Aircraft Refrigeration

Due to the difference in saturation temperature between the condenser and evaporator, large compression ratios were required. Two stages of compression were needed to achieve these large compression ratios. Parallel evaporators were used to decrease the size of the heat exchanger required to achieve the maximum 150 kW heat load. A hot gas bypass was included to inject hot refrigerant from the outlet of the compressor to the inlet of the compression. This component ensures sufficient refrigerant superheating and prevent two-phase flow into the compressor. This component was necessary because the evaporator thermal load has large variations, which is common for aircraft since avionics may only operate during part of a mission.

3.3.2 System Model Assumptions

A thermostatic expansion valve (TXV) and hot gas bypass valve, were used to control the refrigerant superheating and protect the compressor from liquid ingestion. The valve controllers were set to provide a compressor inlet superheat of 5.6^{o}C and 8^{o}C (15^{o}F) for the V&V and tactical aircraft models respectively, as per the recommended practices for aircraft VCC from SAE [37]. Refrigerant charge was assumed to be fixed, and subcooling was dependent on operating conditions. Both back pressure control valves in Figure 3.8 were fully open during system operation.

Pressure drop was included in both models due to its influence on condenser and evaporator saturation temperatures. Pressure drop in the evaporator and suction line decreases compressor suction pressure, while pressure drop in the condenser and discharge line increases compressor

discharge pressure. These changes affect compressor mass flow rate, power, and outlet temperature/enthalpy. The pressure drop in each component is dynamically calculated depending on operating conditions.

Condenser and evaporator saturation pressure was allowed to vary depending on the source and sink boundary conditions. For the V&V model, the condenser saturation temperature is controlled to 51.67°C (125°F) by varying the 75/25 PGW flow rate. The tactical aircraft condenser saturation temperature is not controlled. A variable speed compressor is utilized in the model to control the heat source outlet temperature/coolant delivery temperature regardless of the heat sink temperature and flow rate. This variable speed compressor also increases system efficiency at points of lower than maximum system load [2]. The COP of the system is given by Equation (3-1), where the compressor power is the work term, and evaporator heat load is the cooling load term.

Using the simplified EES model, it was determined that 13.533 kg/s of ram air mass flow was required at the highest heat load and sink temperature. The inlet area was set to 0.05076 m^2 to achieve this ram air flow rate, and was calculated using the method discussed in Section 3.2.2.

For the V&V model, the compressor speed was varied to change the evaporator one saturation pressure to keep the PAO outlet temperature to either 18.3 °C, 15.6 °C, or 12.8 °C as seen in Figure 3.10. For the tactical aircraft model, the compressor was controlled in a similar manner to meet the EGW coolant outlet temperature set point of 20 °C.

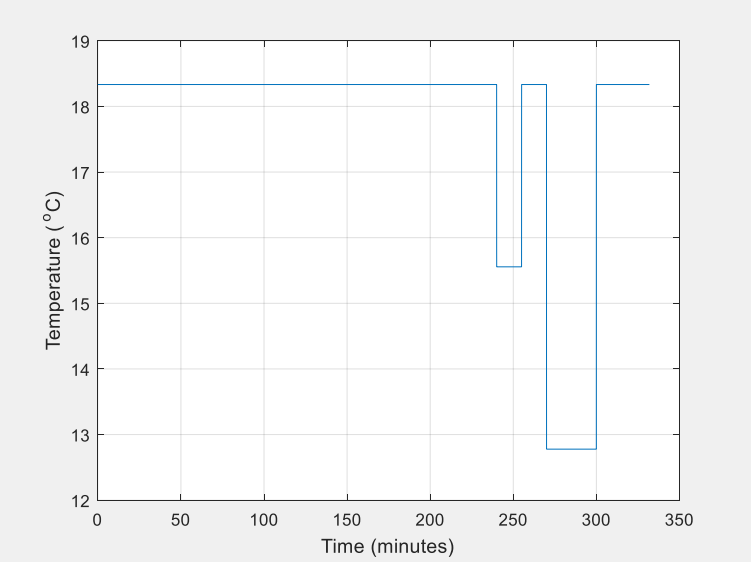

Figure 3.10. Evaporator Oil Outlet Temperature Control Point

3.3.3 Compressor Component Model

The refrigerant compressor model incorporates a first principles physics-based approach to generate the compressor maps that are used to determine component performance. The maps are built using the oil-injected twin-screw compressor correlations from Bommel [38] , using the leakage calculations from Seshaiah et al. [39]. These correlations include the physical geometry of the specific twin-screw compressor as an input, which allows them to be applied to multiple rotor and lobe sizes.

For the VCC model validation, the compressor was modeled based on a 54 mm Fairchild Controls Corporation variable-speed screw compressor. For the tactical aircraft VCC model, the compressor was also a variable-speed screw compressor. The geometry used to build the maps was determined using the two-phase screw compressor sizing GUI built in the ATTMO toolset. The resulting compressor maps are shown in Figure Error! **No text of specified style in document.**.5 through Figure Error! **No text of specified style in document.**.7. The weight and volume of the compressor were estimated by the ATTMO toolset using historical data that correlates weight with flow capacity as outlined by Howden [40].

3.3.4 Condenser Heat Exchanger Component Model

The performance of the refrigerant side of the condenser heat exchanger was calculated using a finite volume model. This model breaks up the condenser into sections and calculates the heat transfer conditions in each section. Each volume is assumed to incorporate the average heat transfer parameters at that location in the heat exchanger. Since each section makes up a fraction of the heat exchanger, all sections must add up to one.

The condenser used in the VCC V&V model is a 70kW Danfoss, B3-095-72-H liquid-refrigerant counter-flow plate heat exchanger. Details of the component geometry were estimated based on the manufacture data sheets and are presented in Table **Error! No text of specified style in document.**.2 [41].

On the liquid side, the model assumes the liquid is evenly distributed across the core of the heat exchanger. On the refrigerant side, the model assumes the flow is evenly balanced between all refrigerant circuits. In the single phase portions of the condenser on both the refrigerant and sink sides, the model uses the Martin plate heat exchanger heat transfer and pressure drop

correlations described by Garcia-Cascales et al. [42], which are valid for Reynolds numbers between 400 and 10,000. In the two-phase portion on the refrigerant side, the model uses the plate heat exchanger heat transfer and pressure drop correlations for HFC-134a described by Yanet al. [43], which are valid for Reynolds numbers between 2000 and 10,000.

The condenser model used in the tactical aircraft VCC is an air-refrigerant cross-flow plate fin heat exchanger. The fin geometric parameters on the refrigerant side and air side were assumed to be offset fins. It was assumed that the both the fins and core were made of aluminum. The condenser dimensions were determined using the ATTMO built in sizing GUI. The conditions for the sizing code were the worst-case boundary conditions, which represented the low altitude, high Mach number dash condition from Mission 2, Segment 4. Air and refrigerant parameters inputted to the sizing code were generated using a simplified model built in EES shown in 0.The resulting condenser dimensions are presented in Table **Error! No text of specified style in document.**.2.

On the air side, the model assumes the air is evenly distributed across the core of the heat exchanger. On the refrigerant side, the model assumes that the flow is evenly balanced between all refrigerant circuits. In the single phase portions of the heat exchanger on both the refrigerant and air sides, the model uses the heat transfer and pressure drop correlations described by Manglik and Bergles [44]. The correlations cover experimentally validated calculations for the Colburn factor (j) and Fanning friction factor (f) coefficients of rectangular strip fins, with Reynolds numbers ranging from 300 to 10,000. In the two-phase portion of the condenser on the refrigerant side, the model uses the heat transfer and pressure drop correlations described by Dobson and Chato [45]. Note that the correlations described in the reference are for smooth horizontal tube condensers, and that a Jakob number of 0.035 was assumed, which represents an average value from the study [45].

3.3.5 Expansion Valve Component Models

The model used for the V&V and tactical aircraft VCC expansion valves assume isenthalpic behavior, meaning enthalpy into the valve equals enthalpy out of the valve. The expansion valve is controlled to produce a specified evaporator superheat. Valve constants are determined by inputting the highest condenser temperature, lowest evaporator temperature and maximum evaporator heat load based on the worst case operating conditions into the valve GUI. Based on the inputs, the component model determines the required mass flow rate to achieve at

least 5.6°C (10°F) of superheating in the evaporator. It then calculates the combined valve discharge coefficient and opening area by solving Eq. (3-16).

$$\dot{m}_r = C_d * A_{valve} * \sqrt{2 * \rho_{r,in} \Delta P_r} \quad (3\text{-}16)$$

where C_d is the valve discharge coefficient, A_{valve} is the valve opening area, $\rho_{r,in}$ is the density of the refrigerant entering the valve, and ΔP_r is the refrigerant pressure drop across the valve

The valve model takes in a position input and translates the signal to a combined discharge coefficient and valve area to determine mass flow rate through the valve. In the VCC model, the translation from valve percentage open to combined discharge coefficient and valve area is assumed to be linear.

For the VCC model V&V, the expansion valves were sized using a 51.62 °C condenser temperature, 6.523 °C evaporator temperature, and a 17.5 kW evaporator heat load. For the tactical aircraft VCC model, the expansion valves were sized using a 95 °C condenser temperature, 5 °C evaporator temperature, and a 100kW evaporator heat load.

3.3.6 Evaporator Heat Exchanger Component Model

The evaporator used in the VCC V&V and tactical aircraft model was a refrigerant-liquid parallel-flow plate fin heat exchanger. For the VCC model validation, an 18kW Niagara Thermal Products heat exchanger was used for both evaporators. Details of the evaporator are contained in Table **Error! No text of specified style in document.**.3. For the tactical aircraft VCC model, the fin geometric parameters on the refrigerant side and liquid side were assumed to be offset fins, and have the same fin parameters as the V&V evaporator heat exchanger. It was assumed that the both the fins and core were made of aluminum.

The evaporator dimensions were determined using the ATTMO built in sizing GUI in a similar manner to the condenser. The conditions for the sizing code represented the worst-case boundary conditions for the heat source. The source return temperature was based on the 55 °C MIL-HDBK-5400 Class 1A maximum electronics temperature, the liquid flow rate was selected to provide 75 kW of cooling with an assumed source supply temperature of 20 °C. Resulting dimensions for the evaporators are presented in Table **Error! No text of specified style in document.**.2.

The model used the finite volume method in a similar manner to the condenser. On the liquid side, the model assumes the liquid is evenly distributed across the core of the heat exchanger. On the refrigerant side, the model assumes the flow is evenly balanced between all refrigerant circuits.

In the single phase portions of the heat exchanger on both the refrigerant and liquid sides, the model also uses the offset fin heat exchanger heat transfer and pressure drop correlations described by Manglik and Bergles [44]. In the two-phase portion of the heat exchanger on the refrigerant side, the model uses the heat transfer and pressure drop correlations described Wattelet et al. [46]. Note that the correlation described in the references is for horizontal tube evaporators, and is valid for heat fluxes between 2018.9 and 40378.8 W/m^2, max fluxes between 25.8 and 1017.2 $kg/s\text{-}m^{2,}$ refrigerant qualities between 5% and 95% and saturation temperatures between -20 and 15^oC.

3.3.7 Hot Gas Bypass Component Model

A hot gas bypass was not included in the VCC V&V model. The hot gas bypass in the tactical aircraft model utilized a similar model and assumptions to the expansion valve component. For the tactical aircraft VCC model, the hot gas bypass valve was sized by assuming a maximum 95^oC condenser temperature, 5^oC evaporator temperature, and 100kW valve capacity.

3.3.8 Line Set Component Model

The line set component model used a finite volume method and the loss coefficient equations outlined by Munson et al. [47] for fluid pressure drop in a pipe. The method assumes the flow is fully developed and compressible Since a line was not included between the expansion valve and evaporator, only single-phase flow was modeled.

For the VCC V&V model, a suction line, discharge line, and liquid line were included. The loss coefficient of all three lines was adjusted to provide close to the measured pressure drop at a single flow condition, but oscillations in the validation data impacted the variability of the pressure drop measurements. Pressure drop was approximately 2.1 kPa for the suction line, 16.0 kPa for the discharge line, and 19.6 kPa for the liquid line. The same three line locations were used for the tactical aircraft VCC model, but the dimensions and lengths of the lines were modeled, instead of an assumed discharge coefficient. For the suction line, the length was 1 m and the diameter was

0.0381 m (1.5 in.), for the discharge line, the length was 0.1 m and the diameter was 0.0254 m (1 in.), and for the liquid line, the length was 1 m and the diameter was 0.0254 m (1 in.). Dimensions are based on line lengths and sizes from the V&V setup, but scaled up to the higher refrigerant flow rates in the tactical aircraft model.

3.3.9 Verification and Validation Process

The data used for the VCC model V&V were obtained from the AFRL VCSRF. Three specific data points were used for verification to tune the model results to within 10% of the test data, the point at 140 minutes, the point at 250 minutes and the point at 300 minutes. These points were chosen to tune the model at multiple heat load and oil temperature set points. After tuning the model using these three points, the model was run for the entire heat load and temperature set points variations covered in Figure 3.1 and Figure 3.10 respectively for the validation process.

3.4 Detailed Reversed-Brayton Cycle Thermal Management System Model

The RBC model was built in MATLAB/Simulink using the PC Krause ATTMO toolset. The RBC performance models were developed, verified and validated using humid air as the working fluid. The property data for these fluids was obtained from the National Institute of Standards (NIST) Reference Fluid Thermodynamic and Transport Properties Database (REFPROP) software converted to lookup tables [36].

3.4.1 Reversed-Brayton Cycle System Model Architecture

The architecture for the RBC model V&V was a two wheel bootstrap air cycle system from a fourth generation tactical aircraft, and is shown in Figure 3.11. It is a modification of the Figure 1.6 architecture, and includes two additional system control valves and two additional liquid-air heat exchangers. The architecture used the water separation subsystem shown in Figure 1.7.

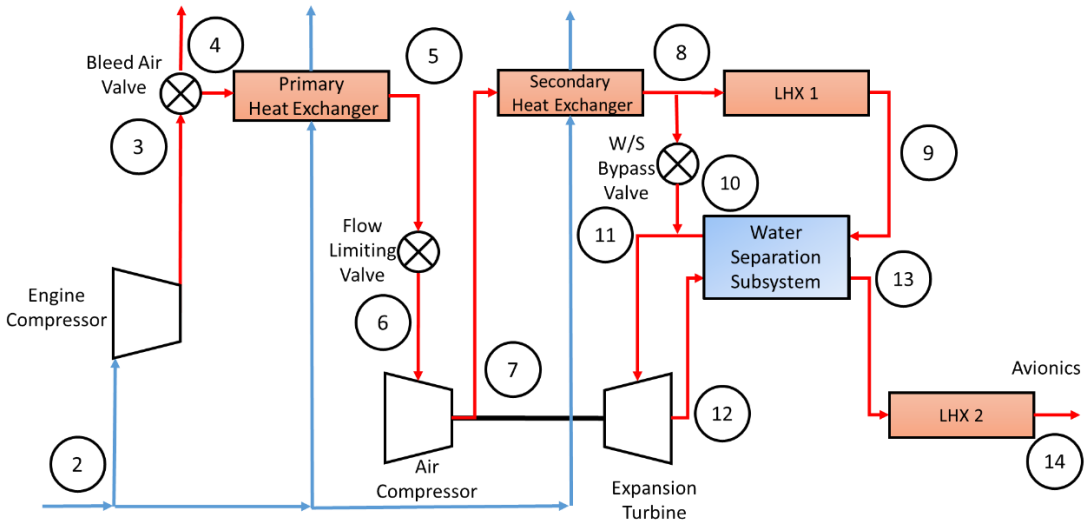

Figure 3.11. Modified Two Wheel Bootstrap Reversed Brayton Cycle Refrigeration System

The RBC architecture chosen for the tactical aircraft study was a three wheel bootstrap air cycle system and is shown in Figure 3.12. This architecture is similar to the previously discussed two wheel bootstrap air cycle, except it has an additional "wheel" in the form of an expansion turbine. This second expansion stage allows for a lower system outlet pressure, which drops the turbine discharge temperature lower than what is possible in a two-wheel system. This configuration increases the cooling capacity of an RBC, reduces bleed air and ram air usage, improves cycle efficiency, and improves moisture removal [48].

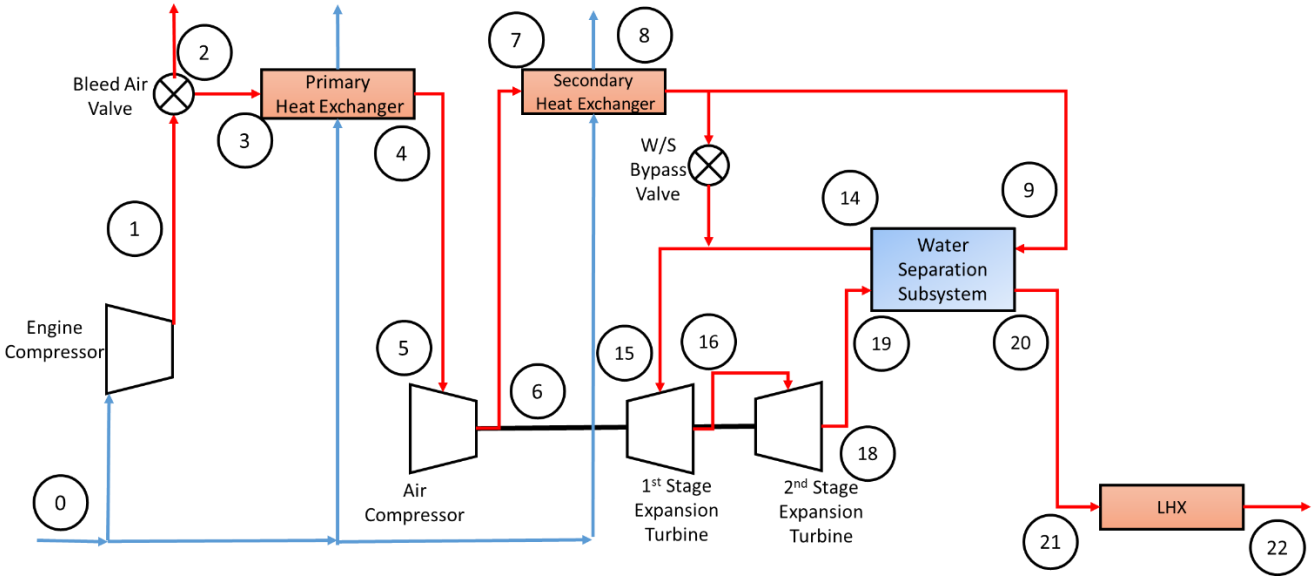

Figure 3.12. Three Wheel Bootstrap Reversed Brayton Cycle Refrigeration System

3.4.2 System Model Assumptions

The RBC system was assumed to operate in an open loop configuration, meaning that the air was sent overboard after absorbing energy from the heat source. Since the system uses a bootstrap configuration, the air compressor and expansion turbine work must be equal since they are mechanically coupled with no shaft losses. Heat transfer capacity of the system was a function of the bleed air flow rate and conditioned air delivery temperature. The COP of the system is given by Equation (3-1), where the work term is equal to the compression work on the ambient air entering the system, and the cooling load term is given by the avionics heat load.

Bleed air flow rate was set by the bleed air valve position. For the RBC V&V model, the valve position is controlled to provide a constant outlet pressure of 963.2 kPa (139.7 psia). For the tactical aircraft model, the valve position was controlled to produce a heat source outlet temperature of 20 ^{o}C. Pressure drop in the heat exchangers was included in both models, along with pressure drop in the ducts between components.

For the RBC V&V model, the system outlet pressure was assumed to be equal to the cabin pressure since the system directly cools both the cabin and avionics. For the tactical aircraft model, the system outlet pressure was assumed to be the ambient pressure since the system is open loop and cools the load via a single liquid-air heat exchanger.

For the RBC V&V model, humidity was modeled by assuming all liquid water in the air is in the form of water vapor, and entrained water increases the relative humidity above 100%. The water vapor and dry air were assumed to behave like an ideal gas mixture, and water was assumed to be removed as it condenses. This assumption simplifies the system model by eliminating the two-phase flow that occurs when entrained moisture is present, but requires bookkeeping the condensing water mass flow in each component to ensure mass continuity is satisfied. The tactical aircraft model was modeling assuming dry air due to inaccuracies discovered in the humidity model at subzero temperatures, which were much lower than the RBC V&V model.

Using the simplified EES model, it was determined that 11.187 kg/s of ram air mass flow rate was required at the highest heat load and sink temperature. The inlet area was set to 0.04196 m^2 to achieve this ram air flow rate, and was calculated using the method discussed in Section 3.2.2.

3.4.3 Engine Compressor Model

The engine compressor was not modeled in the RBC V&V model since the bleed air conditions are given in the provided data set for a specified condition. For the tactical aircraft model, the engine compressor was modeled as a simple isentropic ideal gas compression process. The pressure ratio $r_{p,engine}$ was assumed to vary for the V&V model based on the flight condition, and was as high as 28 for the tactical aircraft model, which is the overall pressure ratio for the F-15 PW-100 engine [49]. This pressure ratio was applied to the ram air total pressure to calculate the bleed air pressure:

$$P_{bleed} = P_{tot,ram} * r_{p,engine} \tag{3-17}$$

note that this pressure is the pressure into the bleed air valve

The bleed air temperature was calculated by determining the temperature for an isentropic compression process:

$$T_{bleed,s} = T_{tot,ram} * r_{p,engine}^{\frac{\gamma-1}{\gamma}} \tag{3-18}$$

The actual bleed air temperature can then be calculated by entering the result of Eq. (3-18) to Eq. (3-10). The engine compressor isentropic efficiency η_{engine} varies depending on the flight condition. Specific enthalpy is given as $T*c_p$ and the heat capacity c_p was assumed to be constant:

$$T_{bleed} = \frac{\left(T_{bleed,s} - T_{tot,ram}\right)}{\eta_{engine}} + T_{tot,ram} \tag{3-19}$$

3.4.4 Valve Models

The bleed air valve was modeled in a similar manner to the VCC expansion valve, except the model assumes single phase flow and that the valve has equal percentage globe behavior. The valve was sized using the ATTMO sizing GUI. For both the V&V and tactical aircraft models, conditions for the sizing code are the worst-case boundary conditions, which represented the sea level low altitude, high Mach number flight condition.

The V&V flow limiting valve was modeled assuming the valve is either fully open or partially closed. When the valve is fully open, it produces a limited pressure drop, while it limits the flow slightly when it is partially closed. The water separator (W/S) bypass valve was modeled in a similar fashion. The flow limiting valve was not included in the tactical aircraft model.

3.4.5 Primary Heat Exchanger Component Model

The primary heat exchanger (PHX) component model used in both the RBC V&V and tactical aircraft models was an air-air cross-flow plate fin heat exchanger. The model used a finite volume approach, in a similar manner to the VCC condenser, evaporator, and intercooler heat exchangers. The performance of the hot and cold side of the heat exchanger both assume the air is evenly distributed across the core of the heat exchanger.

For the RBC V&V model, the geometry and fin parameters were obtained from manufacture data sheets. The cold and hot side have a wavy fin structure, and the correlations used in the model were obtained from Ismail et al. [50]. The correlations were developed to calculate the j and f factors for a wide range of wavy fin parameters, and are valid for Reynolds numbers ranging from 1000 to 15000.

For the tactical aircraft RBC model, the fin geometric parameters were assumed to be the same as the parameters used in the RBC V&V model. For both models, it was assumed that the fins and core were made of a high temperature nickel alloy. The PHX dimensions were determined using the ATTMO built in sizing GUI. The conditions for the sizing code were the worst-case boundary conditions, which represented the sea level low altitude, high Mach number dash condition from Mission 2, Segment 4. Air parameters inputted to the sizing code were generated using a simplified RBC model built in EES and are presented in 0.

3.4.6 Air Compressor Component Model

The centrifugal air compressor model incorporates a first principles physics-based approach to generate the compressor maps using a combination of compressor analysis algorithms developed by Gravdahl and NASA [29]. This method begins by applying the ideal gas law and isentropic pressure rise across the compressor, and incorporating frictional, aero, and mechanical losses to estimate the performance of a non-ideal compressor. A control volume is built around the compressor to conserve mass, energy and momentum. The model takes into account fluid properties, as well as accounting for blade and housing geometry, flow angle, and blade angle. The final result of the model is compressor isentropic efficiency from Eq. (3-10), which can then be used to calculate the actual outlet enthalpy. Because the compressor algorithm is based on the work by Gravdahl and NASA, it has the same limitations, including difficulty in modeling compressor

stall behavior and unrealistic behavior when the inlet flow Mach number is much larger than one [51]. A more detailed description of the compressor loss calculations is contained in [29] and [51].

The compressor geometry used to build the maps were determined using the single-phase centrifugal compressor sizing GUI built in the ATTMO toolset. The weight and volume of the compressor were estimated by the ATTMO toolset using the mass correlations from Hale [52] and Xu and Amano [53] . These correlations were developed for compact engine turbomachinery, but are applicable to reversed-Brayton cycle systems due to the similar structure and size of the components. The calculations take into account the geometric properties and performance of the turbomachinery blades, and then size the supporting disk to handle the resulting forces appropriately.

For the RBC model validation, the compressor was sized using manufacturer data sheets and tuned using the V&V performance data. For the tactical aircraft RBC model, the compressor was sized using information from the V&V model, plus the results of the simplified RBC model results shown in 0. The resulting compressor dimensions are shown in Table **Error! No text of specified style in document.**.14.

3.4.7 Secondary Heat Exchanger Component Model

The secondary heat exchanger (SHX) component was an air-air crossflow plate-fin heat exchanger, and is modeled in a similar manner to the primary heat exchanger. For the RBC model V&V, the SHX geometry was obtained from manufacturer data sheets. Both the cold and hot side used wavy fins, and the correlations for heat transfer and pressure drop were the same as what was used in the PHX model. For the tactical aircraft RBC model, the fin geometric parameters were assumed to be similar to the parameters used in the RBC V&V model. The fins are core were assumed to be made of a high temperature nickel alloy. The SHX dimensions were determined using the ATTMO built in sizing GUI. The conditions for the sizing code were similar to the PHX model.

3.4.8 Water Separation Subsystem

The water separation subsystem incorporated two components, a reheater heat exchanger and condenser heat exchanger. The water collector was not modeled for reasons stated in the

system model assumptions section. The reheater and condenser were both crossflow air-air heat exchangers made of aluminum, and were modeled using the finite volume method and wavy fin correlations used in the PHX and SHX.

For the RBC V&V model, the condenser and reheater dimensions and fin parameters were obtained from manufacturer data sheets. For the tactical aircraft model, the fin parameters for both heat exchangers were assumed to be identical to the RBC V&V model. The dimensions for both heat exchangers were determined using the ATTMO built in sizing GUI. The conditions for the sizing code were similar to the PHX and SHX models.

3.4.9 First Stage Expansion Turbine Component Model

The first stage radial expansion turbine was modeled in a similar manner to the single-phase air compressor, and has similar assumptions. The basic formulation was also similar in that it applies losses to ideal gas assumptions and isentropic expansion equations. Similar to the compressor model, the final result of the model is turbine isentropic efficiency from Eq.(3-8), which can then be used to calculate the actual outlet enthalpy. The turbine model limitations are also similar in that it does not sufficiency capture stall behavior [54]. A more detailed description of the turbine loss calculations is contained in [29] and [54]. The turbine geometry used to build the maps was determined using the single-phase radial turbine sizing GUI built in the ATTMO toolset. The weight and volume of the turbine were estimated by the ATTMO toolset in a similar manner to the compressor.

For the RBC model V&V, the turbine was sized using manufacturer data sheets and tuned using the performance data. For the tactical aircraft RBC model, the first stage expansion turbine was sized using information from the V&V model, plus the results of the simplified RBC model results shown in 0. The resulting dimensions are shown in Table **Error! No text of specified style in document.**.14.

3.4.10 Second Stage Expansion Turbine Component Model

The RBC V&V model did not have a second stage expansion turbine. For the tactical aircraft model, the second stage radial expansion turbine was modeled in a similar manner to the first stage radial expansion turbine. The weight and volume of the turbine were estimated by the

ATTMO toolset in a similar manner to the first stage expansion turbine. The second stage expansion turbine was sized using the built in ATTMO sizing tool using similar conditions as the first stage turbine, and the resulting dimensions are shown in Table **Error! No text of specified style in document.**.14.

3.4.11 Liquid Load Heat Exchanger Component Model

Two liquid load heat exchangers were included in the RBC V&V model, both being air-liquid counter-flow plate fin heat exchangers in a parallel configuration. A single liquid load heat exchanger was used in the tactical aircraft RBC model. The liquid load heat exchanger model also used the finite volume method in a similar manner to the PHX and SHX.

For the RBC V&V model, the fin geometric parameters and dimensions for both liquid load heat exchangers were obtained from manufacturer data sheets. The fins on liquid and air sides were wavy, and the correlations for heat transfer and pressure drop were the same as the wavy fin correlations used in the PHX, SHX, and condenser/reheater. For the tactical aircraft RBC model, the fin geometric parameters were assumed to be the same as the RBC V&V model. It was assumed that both the fins and core were made of aluminum.

The tactical aircraft RBC model liquid load heat exchanger dimensions were determined using the ATTMO built in sizing GUI. The conditions for the sizing code represented the worst-case boundary conditions for the heat source, and were generated in a similar manner to the PHX and SHX conditions. The source return temperature is based on the 55^{o}C MIL-HDBK-5400 Class 1A maximum electronics temperature, the liquid flow rate was selected to provide 150 kW of cooling with an assumed source supply temperature of 20^{o}C. The resulting dimensions are presented in Table **Error! No text of specified style in document.**.16, and the fin information is presented in Table **Error! No text of specified style in document.**.17.

3.4.12 Duct Model

The duct model used a finite volume method in a similar manner to the VCC line set model. Pressure drop was calculated using the same single phase correlations as those used in the line set model. For the RBC V&V model, the ducts loss coefficients were modified to match the validation data pressure drop at the high flow condition in a similar manner to the VCC line set model. Five

ducts were modeled; the duct running from the bleed air valve to the PHX, the PHX to the compressor, the compressor to the SHX, the reheater to the turbine, and turbine to condenser. The pressure drops used to tune the duct model were as follows: 81.7 kPa, 16.4 kPa, 12.9 kPa, 4.9 kPa, and 3.6 kPa. For the tactical aircraft RBC model, the ducts were identical to the V&V model, except the length was set to 1.0 m for weight estimation purposes.

3.4.13 Verification and Validation Process

The data used for the RBC V&V were obtained from performance data from a fourth generation tactical aircraft RBC TMS. Due to the nature of the data, as well as the limited number of applicable flight conditions, only three data sets could be used for model V&V. The data sets were chosen to encompass the Mission 1 and Mission 2 flight conditions shown in Table 3.2 and Table 3.3 respectively. Descriptions of the data sets are presented in Table 3.4. The goal of the V&V process was to tune the model results to within 25% of the performance data.

Table 3.4. Data Set Descriptions for System Model Verification and Validation

Run Number	Flight Condition	Ambient Conditions	Altitude (km)	Mach Number (-)
1	Sea Level Dash	Hot Day	0	0.98
2	High Altitude Cruise	Hot Day	13.716	0.85
3	Sea Level Loiter	Hot Day	0	0.36

3.5 Vapor Compression Cycle and Reversed-Brayton Cycle Comparison

3.5.1 Aircraft Model

The aircraft model used for the TMS comparison was based on the fourth generation F-15 Eagle tactical aircraft with a F100-PW-100 engine. A schematic of the aircraft is presented in Figure 3.13.

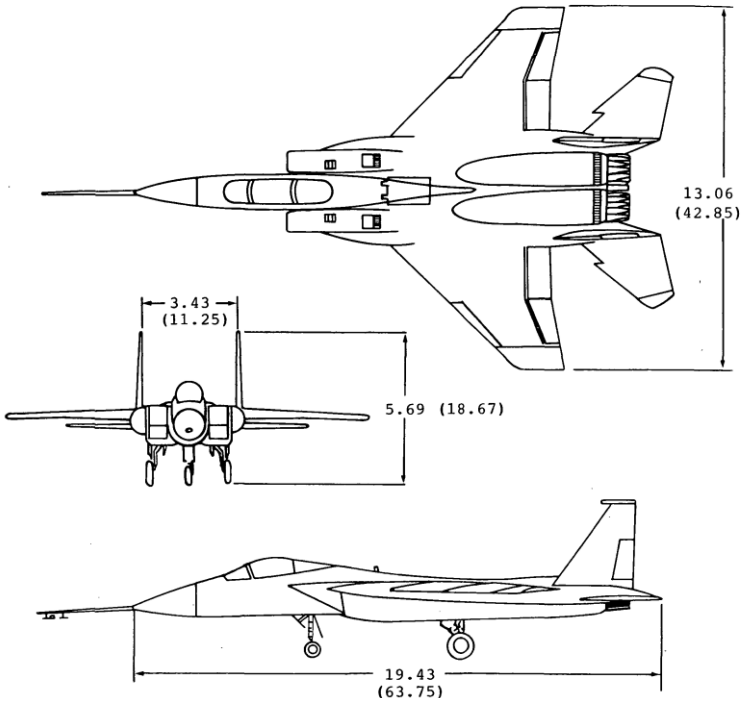

Figure 3.13. Three-View Drawing of F-15 Airplane. Dimensions in m (ft) [33]

The lift-to-drag coefficients for the aircraft were generated using the coefficient of lift and coefficient of drag data from the report. The drag polar is presented in Figure 3.14. Because the data from Mach 0 to Mach 0.9 were similar, only a single curve was plotted; the curve at Mach 1.0 differed and was plotted. The maximum lift-to-drag ratio of 10.67 was used for the impact correlations.

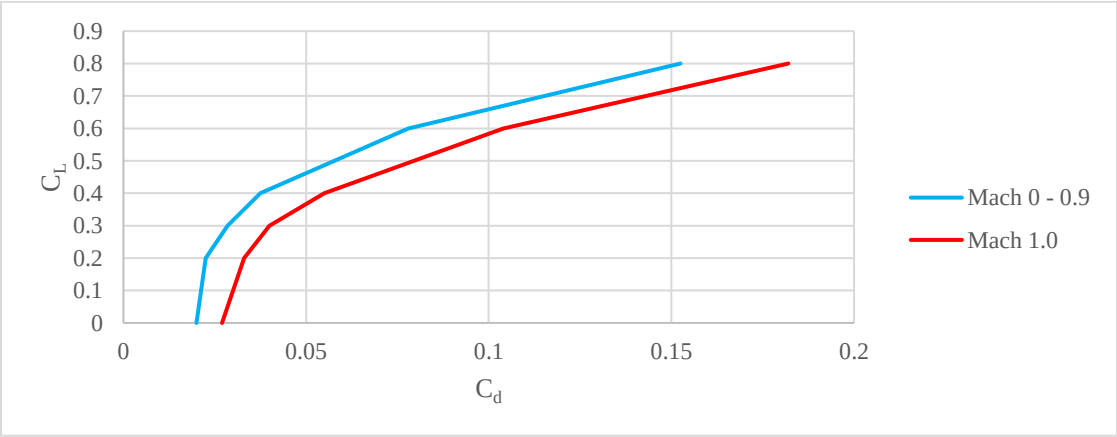

Figure 3.14. Drag Polar for the F-15 (modified from [33])

SFC for engine thrust was calculated by dividing total fuel flow rate data by the net thrust data in Figure 3.15 and Figure 3.16 respectively and is presented in Figure 3.17. The fuel flow data were generated with 48.47 kW (65 hp) of power take-off and 0.32 kg/s (0.7 lb/s) of bleed air extraction. However, the fuel increases due to both influences were kept in the fuel flow rate values as a worst-case condition.

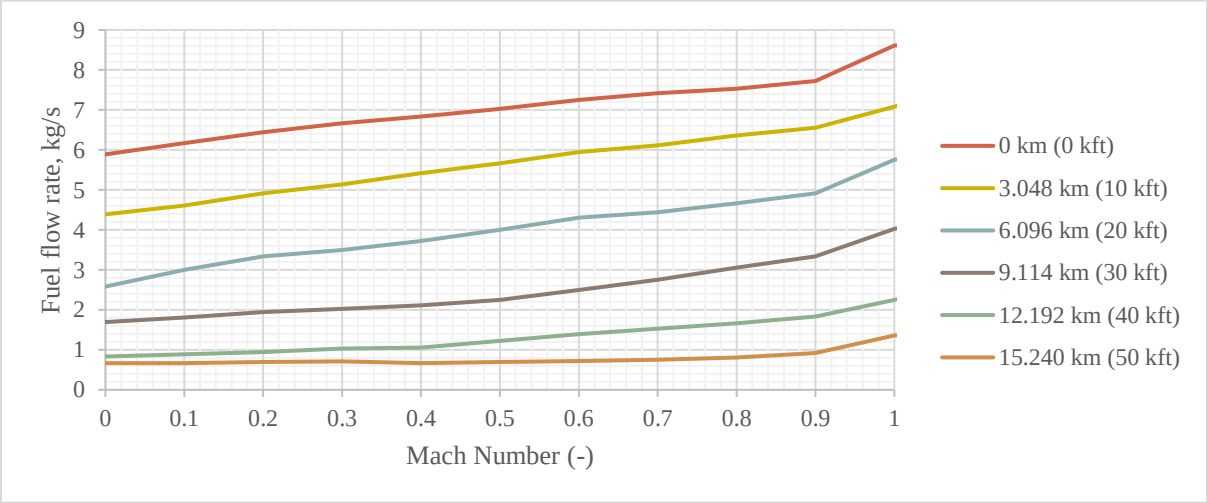

Figure 3.15. Total Fuel Flow Rate at maximum power for the F100 engines in the F-15 HIDEC (modified from [33])

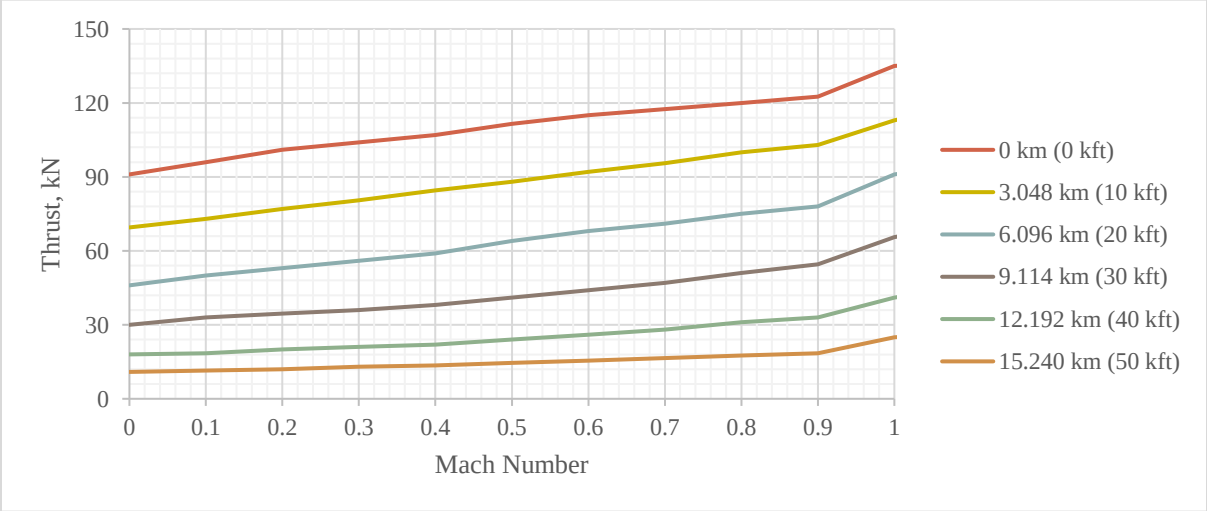

Figure 3.16. Net Thrust at maximum power for the F100 engines in the F-15 HIDEC (modified from [33])

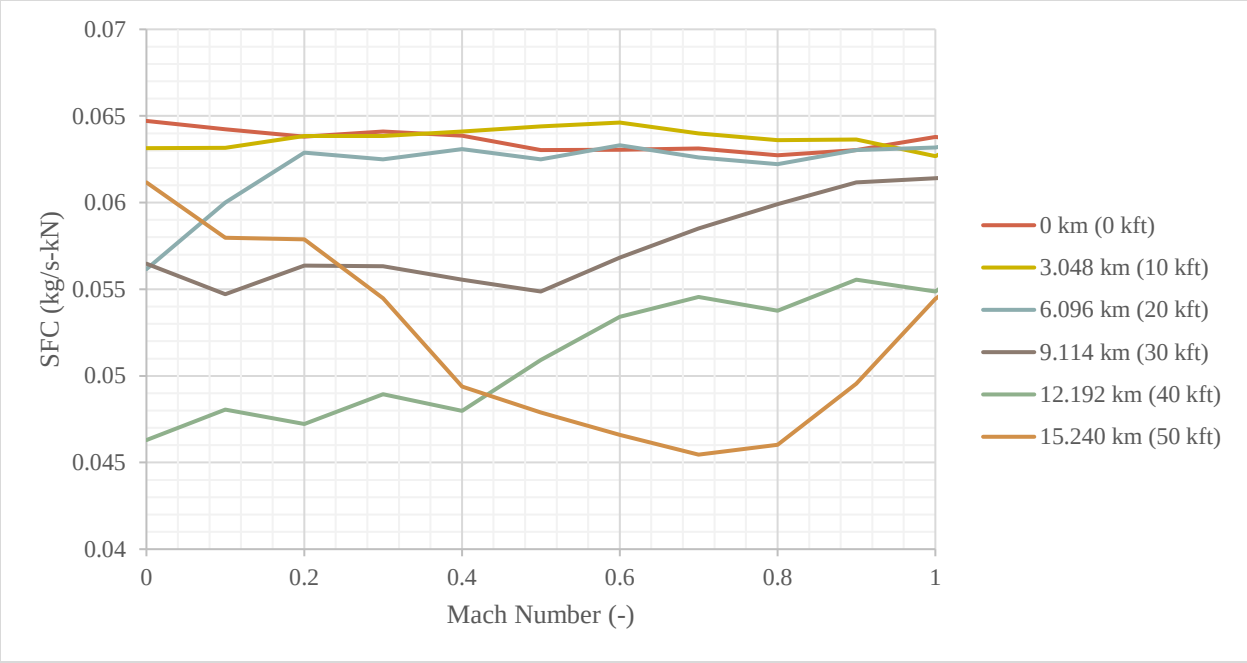

Figure 3.17. Specific Fuel Consumption for Thrust at maximum power as a function of Mach Number for the F100 engine (modified from [33])

SFC for power take off was calculated using the method for turbofan engines outlined in [23]. This method was applicable since the F-15 utilizes the F100 turbofan engine. The first step to calculate SFC for power take-off was to calculate the shaft power factor k_{pwr} of the engine using:

$$k_{pwr} = 0.0057 + 4.6 * 10^{-8} * \frac{1}{m} * H - 0.0106 * M - 4.44 * 10^{-13} * \frac{1}{m^2} * H^2 + 1.85 * 10^{-7} * \frac{1}{m} * H * M + 0.0049 * M^2 \quad (3\text{-}20)$$

where the units of k_{pwr} are N/W, H is the altitude in meters and M is the Mach Number.

The power factor from Eq. 3-20 can then be multiplied by the SFC value for thrust to determine the SFC for power take-off:

$$(SFC)_{pwr} = (SFC)_{Th} * k_{pwr} \quad (3\text{-}21)$$

3.5.2 Energy-Based Aircraft Penalty Method

The energy-based method fuel penalty equations were obtained from the SAE Aerospace Information Report (AIR)1168/8 Aircraft Fuel Weight Penalty Due to Air Conditioning. The AIR contains correlations that relate system parameters and performance to aircraft impacts via penalty equations. These correlations assume a fixed aircraft range, and that all weight penalties increase

the total aircraft weight [16]. Note that all weight penalties relations were originally in English units.

The first penalty included in the analysis is due to the fixed weight penalty of the TMS and the increase in take-off mass in kg is calculated using Eq. (3-22).

$$m_{fo,system} = m_{sys} * exp\left[\frac{(SFC)_{th} * \tau}{L/D}\right] - m_{sys} \tag{3-22}$$

where m_{system} is the mass of the system in kg, $(SFC)_{th}$is the specific fuel consumption for power in kg/(N*s), τ is the length of the mission under evaluation in seconds, and $L/D$is the aircraft lift to drag ratio.

The second penalty is due to expendable material used for cooling, and assumes a constant rate of consumption. Eq. (3-23) relates this penalty to the increase take-off fuel weight.

$$m_{fo,expend} = \left[\frac{L/D}{(SFC)_{th}}\right] * \left[\exp\left\{\frac{(SFC)_{th} * \tau}{L/D}\right\} - 1\right] * \dot{m}_{expend} - \dot{m}_{expend} * \tau \tag{3-23}$$

where $\dot{m}_{expend}$ is the rate of consumption of the expendable material in kg/s.

The third penalty is due to ram air usage, and the increase in take-off weight calculation is presented in Eq. (3-24); the equation assumes complete loss of air momentum.

$$m_{fo,ram} = \frac{\dot{m}_{ram} * V * (L/D)}{g} * \left[\exp\left\{\frac{(SFC)_{th} * \tau}{L/D}\right\} - 1\right] \tag{3-24}$$

where $\dot{m}_{ram}$ is the ram air mass flow rate in kg/s, V is the cruise velocity in m/s, and g is the gravitational constant in m/s^2

The fourth penalty is due to bleed air extraction, and first assumes the increase in fuel flow due to bleed air usage is given by Eq. (3-25). This equation is a first approximation that assumes fuel flow must increase to maintain constant engine thrust.

$$\Delta\dot{m}_{fuel} = 0.0335 * \left[\frac{(T_{turb,in} * 9/5 + 491.67)}{2000}\right] * \dot{m}_{bleed} \tag{3-25}$$

Where $T_{turb,in}$ is the engine turbine inlet temperature in ^{o}C and $\dot{m}_{bleed}$ is the bleed air mass flow rate in kg/s.

The fuel flow rate given in Eq. (3-25) can then be related back to increase in take-off fuel weight via Eq. (3-23). The second $\dot{m}_{expend} * \tau$ term cancels out since the increased amount of fuel is also the expendable material. The result is shown in Eq. (3-26).

$$m_{fo,bleed} = 0.0335 * \left[\frac{L/D}{(SFC)_{th}}\right] * \left[\frac{(T_{turb,in} * 9/5 + 491.67)}{2000}\right] * \left[\exp\left\{\frac{(SFC)_{th} * \tau}{L/D}\right\} - 1\right] * \dot{m}_{bleed} \quad (3\text{-}26)$$

The fifth and final penalty used in this analysis is related to shaft power take-off, and the increase in take-off weight due to this penalty is given in Eq. (3-27). This relation assumes the fuel flow rate must increase to maintain constant net thrust from the engine, and assumes the power is used at a constant rate during the mission phase analyzed.

$$m_{fo,pto} = \dot{W}_{TMS} * \left(L/D\right) * \left[\frac{(SFC)_{pwr}}{(SFC)_{th}}\right] * \left[\exp\left\{\frac{(SFC)_{th} * \tau}{L/D}\right\} - 1\right] \quad (3\text{-}27)$$

where $(SFC)_{th}$ is calculated per Eq. (3-21) and $\dot{W}_{TMS}$ is the TMS power usage in W

Summing the weight penalties from each relation gives the total TMS penalty in terms of increased take-off fuel weight required for the mission segment under analysis.

3.5.3 Exergy-Based Aircraft Penalty Method

The exergy-based aircraft penalty method was based on the studies performed by Pellegrini et al. [20] and Tona et al. [21] as summarized by Olivera [19]. Both the "global" and "local" methods were used. The global method relates TMS performance to aircraft impacts via exergy flow throughout the aircraft, which result in an exergy destruction term for each aircraft subsystem. This destroyed exergy relates to aircraft impact since inefficiencies in the TMS require the aircraft to input additional power in the form of fuel to overcome the losses [18]. The local method breaks the global method results down to the individual component level to determine the component(s) that contribute most to the overall subsystem exergy destruction term and help determine potential areas of improvement.

The first step of the global and local exergy-based methods was to draw a control volume around the region of interest and establish exergy flow between the subsystems, as shown in Figure 3.18.

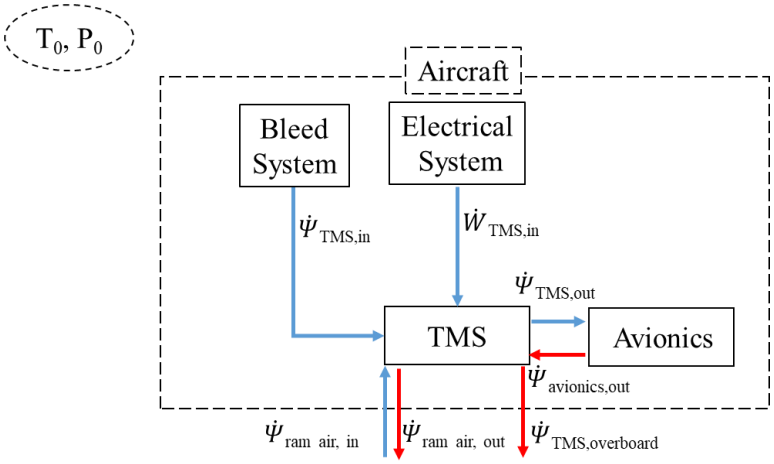

Figure 3.18. Control Volume for Exergy-Based Analysis (Modified from [19])

Note that exergy flows between other subsystems besides the TMS are not shown. For the open loop RBC model, the $\dot{W}_{TMS,in}$ power input to the TMS was zero. For the closed loop VCC model, the $\dot{\Psi}_{\text{TMS,in}}$ bleed air flow and $\dot{\Psi}_{\text{TMS,overboard}}$ were zero.

The next step was to establish environmental reference condition for the change in entropy, denoted by T_o and P_o in Figure 3.18. As discussed by Tona et al. [21], a constant reference may lead to negative exergy flow depending on the flight conditions. Therefore, a varying reference based on static conditions of the air around the aircraft was selected. After establishing the control volume and reference conditions, the exergy flowrate was then calculated using Eq. (3-28):

$$\dot{\Psi} = \dot{m}[h - h_o - T_o(s - s_o)] \tag{3-28}$$

where h_o and s_o refer to the specific enthalpy and specific entropy for the fluid at the reference conditions, respectively.

For the VCC model, the entropy difference was calculated using HFC-134a property tables. For the RBC model, the specific entropy difference was calculated using dry air property tables. The destroyed exergy rate was then calculated based on the exergy flows entering the system, as well as the flows leaving the subsystem that are not used for other purposes. For the TMS, this unused flow was the ram air leaving the TMS source heat exchanger and the air sent overboard and can be calculated using Eq. (3-29):

$$\dot{I}_{TMS} = \dot{\Psi}_{TMS,in} + \dot{\Psi}_{ram\ air,in} + \dot{\Psi}_{avionics,out} + \dot{W}_{TMS,in} - \left(\dot{\Psi}_{TMS,out}\right) \tag{3-29}$$

The exergy efficiency of the TMS, which is defined as the ratio of the exergy entering the system and the exergy used in the system, can then be calculated using Eq. 3-30:

$$\eta_{ex,TMS} = \left(\frac{\dot{\Psi}_{TMS,out}}{\dot{\Psi}_{TMS,in} + \dot{\Psi}_{ram\ air,in} + \dot{\Psi}_{avionics,out} + \dot{W}_{TMS,in}} \right) \tag{3-30}$$

The exergy destruction rate and exergy efficiency rate calculated for both the RBC and VCC TMS were then compared to determine the system that is more efficient and has a lower rate of exergy destruction.

For the local method, the component level exergy destruction can be calculated using a local exergy balance for a control volume around each component using Eq. (3-31) as follows:

$$\dot{I}_{component} = \sum_{i=0}^{n} \left(1 - \frac{T_0}{T_i}\right) \dot{Q}_i - \dot{W} + \sum_{in} \dot{\Psi} - \sum_{out} \dot{\Psi} \tag{3-31}$$

where T_i refers to the temperature at the heat transfer interface, $\dot{Q}_i$ refers to the heat transfer rate at the interface.

The destroyed exergy for each component can then be compared to determine which component is destroying the largest amount of exergy. The exergy efficiency for each component can also be compared to determine how efficiently each component utilizes supplied exergy to perform its' function. Exergy efficiency for the heat exchangers was calculated using Eq. (3-32)

$$\begin{aligned} \eta_{ex,HX} &= \frac{\dot{\Psi}_{cold,out} - \dot{\Psi}_{cold,in}}{\left|\dot{\Psi}_{hot,out} - \dot{\Psi}_{hot,in}\right|} \quad if\ T_{cold} \geq T_o \\ \eta_{ex,HX} &= \frac{\dot{\Psi}_{cold,out} + \dot{\Psi}_{hot,out}}{\dot{\Psi}_{cold,in} + \dot{\Psi}_{hot,in}} \quad if\ T_{cold} < T_o \end{aligned} \tag{3-32}$$

Compressor exergy efficiency was determined using Eq. (3-33)

$$\eta_{ex,comp} = \frac{\dot{\Psi}_{out} - \dot{\Psi}_{in}}{\dot{W}_{comp}} \tag{3-33}$$

Turbine exergy efficiency was determined using Eq. (3-34)

$$\eta_{ex,turb} = \frac{\dot{W}_{turb}}{\dot{\Psi}_{out} - \dot{\Psi}_{in}} \tag{3-34}$$

Valve, duct and line 2nd law efficiency was calculated using Eq. (3-35)

$$\eta_{ex,valve,duct,line} = \frac{\dot{\Psi}_{out}}{\dot{\Psi}_{in}} \tag{3-35}$$

4. RESULTS AND DISCUSSION

4.1 Verification and Validation

4.1.1 Vapor Compression Cycle Model Verification and Validation

Evaporator four oil outlet temperatures for the full heat load and oil temperature variations are presented in Figure 4.1. As seen in the figure, the model's steady state results closely match the test data, demonstrating that the system is controlled to the specified oil outlet temperature. The transient behavior is not as well captured during changes in evaporator heat load and oil outlet temperature, but the results become closer as the system stabilizes. A similar result is observed for the evaporator five oil outlet temperature shown in Figure 4.2, except higher steady state error is present since the outlet temperature is not controlled. This error decreases after 200 minutes, which coincides with both evaporator heat loads increasing to 100%.

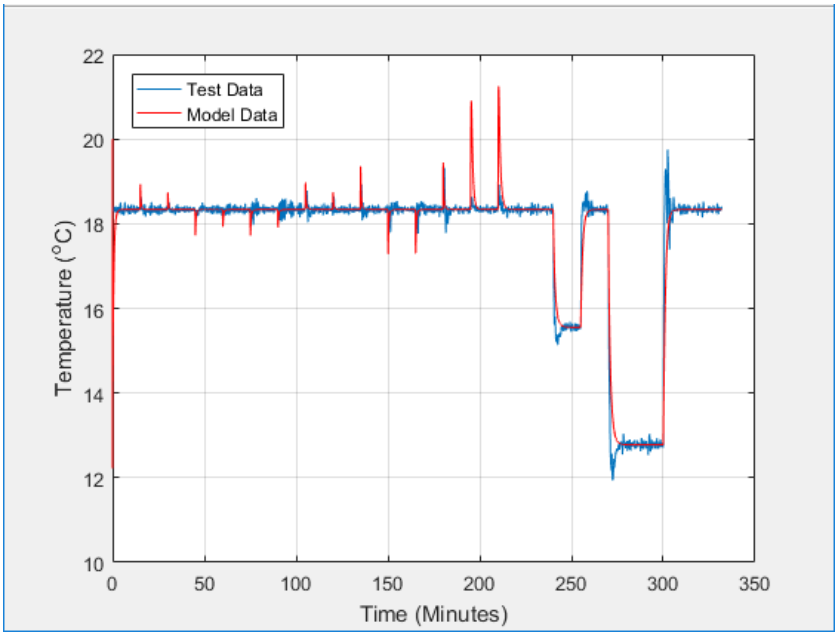

Figure 4.1. Evaporator Four Oil Outlet Temperature

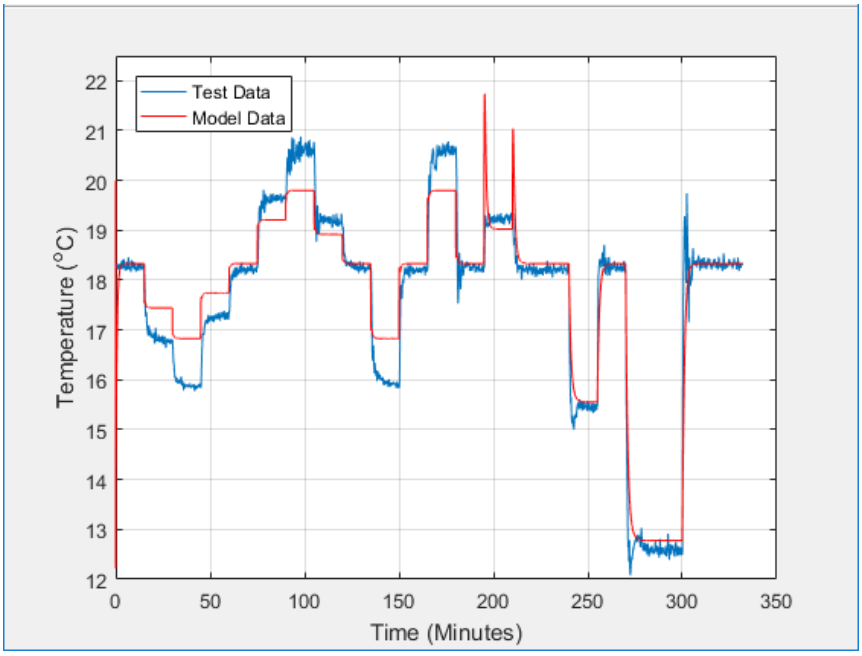

Figure 4.2. Evaporator Five Oil Outlet Temperature

The evaporator four and five heat loads shown in Figure 4.3 and Figure 4.4 respectively exhibit a similar trend, since the model's results match the test data's steady state results well. Some of the test data heat loads' transient behavior were not as well captured by the model, but the results tended to agree after a few minutes of simulation time. Transient error is observed between the model and test data during each of the heat load step changes, but the error decreases as the system adjusts to the changes. Transient error is also seen after 200 minutes in both figures, which coincides with the evaporator four oil outlet temperature cycling, but also decreases as the system adjusts to the temperature step changes.

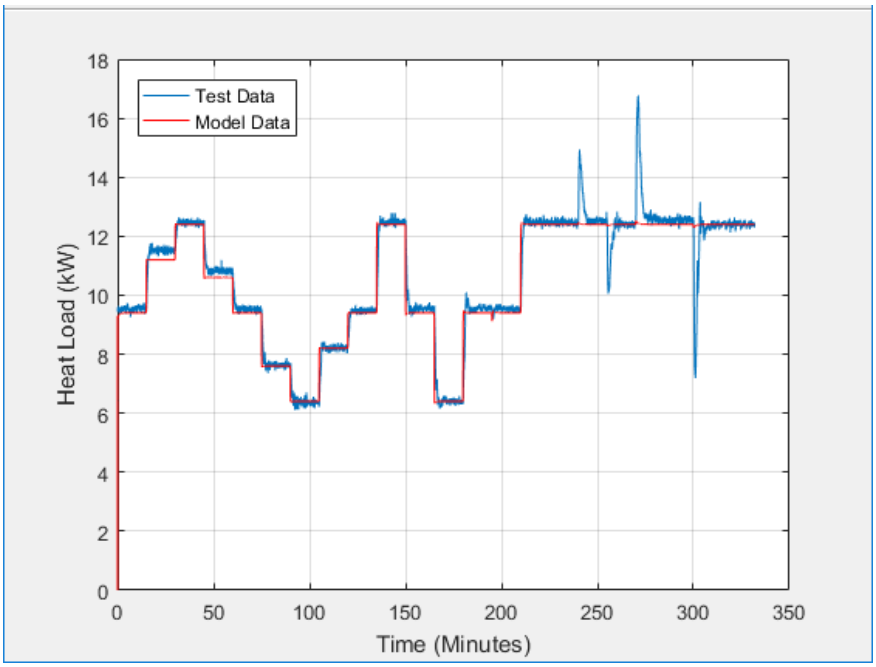

Figure 4.3. Evaporator Four Heat Load

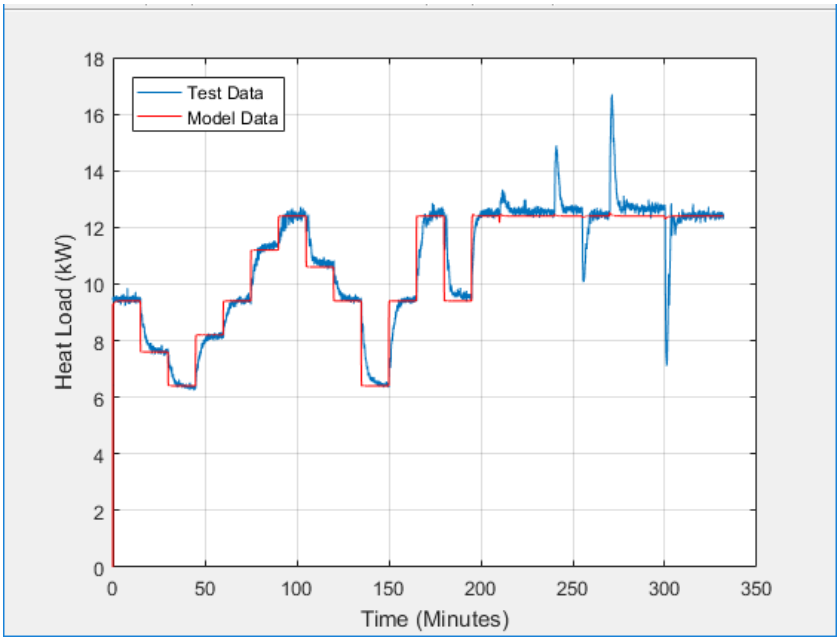

Figure 4.4. Evaporator Five Heat Load

Evaporator four and five superheat was held to a constant 5.6°C (10°F) during all points, and the condenser saturation temperature was controlled to a constant 51.64°C (125°F) during all points. Full results of the three model runs for the model verification are presented in 0, including

an error analysis, temperature-entropy diagrams, and pressure-enthalpy diagrams. For all three runs, all parameters matched the test data to within 10%, except for the suction line pressure drop, which was 17.3% lower.

4.1.2 Reversed-Brayton Cycle Model Verification and Validation

Boundary conditions for the RBC verification and validation model are presented in Table 4.1.

Table 4.1. Reversed Brayton Cycle System Validation Model Boundary Conditions

Parameter	Run 1	Run 2	Run 3
T_{amb} (ºC)	40.56	-33.33	40.56
P_{amb} (kPa)	101.33	14.748	101.33
ω_{amb} (kg/kg)	0.03	0.00143	0.03
$T_{total,ram}$ (ºC)	100.8	1.347	48.69
$P_{total,ram}$ (kPa)	158.0	20.80	105.6
T_{bleed} (ºC)	565.6	460.0	340.0
P_{bleed} (kPa)	2968	582.6	941.9
$\dot{m}_{ram,PHX}$ (kg/s)	5.739	0.4873	1.430
$\dot{m}_{ram,SHX}$ (kg/s)	5.739	0.5740	1.551

COP for the RBC V&V model is presented in Table 4.2. The COP for all three Runs was very low since the amount of compression work performed by the ram air effect and engine compression is much larger than the cooling capacity of the RBC system. The relative error for the RBC COP ranges from -0.107% to 38.6%.

Table 4.2. Reversed Brayton Cycle COP for All Validation Model Runs

Run Number	COP, Validation Data (-)	COP, Validation Model (-)	COP Relative Error (%)
1	0.0861	0.0955	10.9%
2	0.149	0.206	38.6%
3	0.183	0.183	-0.107%

Relative and absolute error comparisons are presented in Table 4.3 and Table 4.4 respectively. The relative error for the RBC outlet temperature ranges from -1.6% to 3.9% for the three runs, while absolute error ranges from -4.18^{o}C to 10.93 ^{o}C. The relative error for the RBC air outlet mass flow rate ranges from 25.3% to 28.5%, while the absolute error ranges from 0.0884 kg/s to 0.136 kg/s. The relative error for the RBC cooling capacity ranges from 5.89% to 32.5%, while the absolute error ranges from 1.82 kW to 8.75 kW.

The goal of the validation effort was to ensure the modeled RBC followed similar trends to an actual RBC system. The model reacted to changes in boundary conditions similar to a real RBC, such as the system flow rate changing proportionally with ambient pressure, which directly controls the cooling capacity of the system. Additionally, conservation of mass and energy were met for all model runs.

A likely source of error was the humidity model neglecting entrained water evaporation. For high humidity Runs 1 and 3, this caused the V&V model outlet temperature to trend higher than the V&V data, since entrained moisture evaporation in the heat exchangers tends to enhance heat exchanger performance. The heat exchanger model effectiveness had to be increased to compensate, which resulted in the temperature trending lower for low humidity Run 2. For Runs 1 and 3, which occurred in humid conditions, it was noted in the validation data that the SHX hot side outlet temperature is lower than the SHX cold side inlet temperature, which is likely due to the cold water aspirator on the SHX cold side, which further cools the air. This caused the model SHX hot side and cold side outlet temperatures to be higher than the validation data since it enhances the heat exchanger cooling.

In addition to the SHX cold side, the lack of entrained moisture evaporation is also noted in the reheater, condenser and LHX 2 cold side outlet temperatures. The condenser cold side temperature error was larger for the high humidity runs, being 10.8% and 18% higher for Runs 1 and 3 respectively, and only 1.8% for low humidity Run 2. The reheater cold side temperature error showed similar trends, being 4.6% and 8.9% for Runs 1 and 3 respectively, but 2.1% for Run 2. LHX 2 also demonstrates this trend, with the cold air outlet temperature error being 0.65% and 3.9% for Runs 1 and 3 respectively, but -1.6% for Run 2. This lower temperature, coupled with the higher mass flow rate, caused the system cooling capacity error to be higher for Run 2 than Runs 1 and 3. A similar trend was noted in the COP since it is a function of system cooling capacity.

Since the hot air stream did not undergo constant temperature latent heat transfer, the model temperature trended higher than the validation data for high humidity Runs 1 and 3. Conversely, Run 2 occurred in low humidity conditions, and as a result the model produced a lower delivery temperature since the system components overcooled to account for the lack of water aspiration and moisture evaporation in the high humidity condition.

Another likely source of error was the simplified system architecture and controls. Some system controls were not included due to insufficient system information or the complexity of the controls. The simplifications also contributed to the error since the system precisely controls flow through the interaction of multiple system valves, and directs flow to perform other functions, such as controlling compressor maximum outlet temperature, turbine minimum outlet temperature, and small thermal loads.

Though these two sources of error reduced the accuracy of the model compared to the validation data, they did not impact the ability of the model to capture the behavior of an RBC cooling system. The model's cooling capacity was larger than the validation data, but the system mass flow rate was also higher, indicating that the system may not be overperforming. Furthermore, the model delivery temperature, which is proportional to cooling capacity remained relatively close to the validation data. Because of these factors, the model was considered validated, despite the relative error being higher than 25% for some system parameters.

Table 4.3. Validation Data and Model Results Relative Error for All Model Runs

Run Number	$\boldsymbol{T_{RBC,out}}$ **Relative Error (%)**	$\boldsymbol{\dot{m}_{RBC,out}}$ **Relative Error (%)**	$\boldsymbol{\dot{Q}_{cool,RBC}}$ **Relative Error (%)**
1	0.932	25.3	19.3
2	-1.59	26.5	32.5
3	3.91	28.5	5.89

Table 4.4. Validation Data and Model Results Absolute Error for All Model Runs

Run Number	$\boldsymbol{T_{RBC,out}}$ **Absolute Error (°C)**	$\boldsymbol{\dot{m}_{RBC,out}}$ **Absolute Error (kg/s)**	$\boldsymbol{\dot{Q}_{cool,RBC}}$ **Absolute Error (kW)**
1	2.63	0.137	6.46
2	-4.18	0.0884	8.75
3	10.93	0.136	1.82

4.2 Tactical Aircraft Conditions

4.2.1 Tactical Aircraft Cooling System Boundary Conditions

The tactical aircraft model boundary conditions in Table 4.5, were determined by applying the atmospheric model to the run matrix from Table 3.2 and Table 3.3 for Missions 1 and 2 respectively.

Table 4.5. Tactical Aircraft Cooling System Boundary Conditions for Both Missions

Mission 1							
Segment	**T_{amb} (^oC)**	**P_{amb} (kPa)**	**$T_{tot,ram}$ (^oC)**	**$P_{tot,ram}$ (kPa)**	**$\dot{m}_{ram,\ RBC}$ (kg/s)**	**$\dot{m}_{ram,\ VCC}$ (kg/s)**	**$\dot{m}_{source}$ (kg/s)**
1	41.00	101.33	41.00	101.33	3.00	3.00	0.45
2	-23.77	23.84	12.26	32.17	3.38	4.09	0.90
3	-0.56	46.56	53.96	72.42	7.44	9.00	1.36
4	-23.77	23.84	12.26	32.17	3.38	4.09	0.90
5	-8.96	37.60	4.25	41.69	3.22	3.90	0.68
Mission 2							
Segment	**T_{amb} (^oC)**	**P_{amb} (kPa)**	**$T_{tot,ram}$ (^oC)**	**$P_{tot,ram}$ (kPa)**	**$\dot{m}_{ram,\ RBC}$ (kg/s)**	**$\dot{m}_{ram,\ VCC}$ (kg/s)**	**$\dot{m}_{source}$ (kg/s)**
1	41.00	101.33	41.00	101.33	3.00	3.00	0.45
2	-16.21	30.09	20.92	40.60	4.21	5.09	0.90
3	-8.96	37.60	10.06	41.69	3.86	4.67	1.13
4	40.30	100.13	75.56	124.08	11.19	13.53	1.36
5	-16.21	30.09	20.92	40.60	4.21	5.09	0.90
6	-3.45	43.31	15.97	48.01	4.40	5.33	0.68

4.2.2 Tactical Aircraft Cooling System Model Results

Cooling performance for both systems compared to the cooling goal is presented in Figure 4.5 for all segments of Mission 1 and in Figure 4.6 for all segments of Mission 2. As seen in Figure 4.5, the VCC tended to cool more than the goal for most segments of Mission 1, going as high as 21.5 kW above the goal during Segment 5. This trend was not seen during Segment 3, the high heat load, high ambient temperature combat section, which is the most demanding segment of the mission. This overcooling effect is because of the VCC system being sized for the 150kW max heat load condition and the requirement that the flow into the compressor have 8^{o}C of superheat, which was met for all segments of both missions. The RBC tended to cool the goal amount, but

fell 8.6kW short during Segment 5, the low speed, high altitude loiter section. This shortfall is a result of the low ram pressure and engine pressure ratio producing a correspondingly low bleed air pressure, which produces insufficient bleed air flow to power the RBC and cool the load.

Similar trends can be observed in Figure 4.6 for Mission 2, except the VCC fell 2.8kW short of the goal during Segment 4, low altitude dash, which is the most demanding case due to the high heat load and high sink temperature. Similar to Mission 1, the RBC fell 38.6kW short during the Segments 3 loiter and 9.3kW short during the Segment 6 loiter, again due to low bleed air pressure producing insufficient flow for the RBC cooling system. The RBC system also fell 1.8 kW short during Segment 4, low altitude dash.

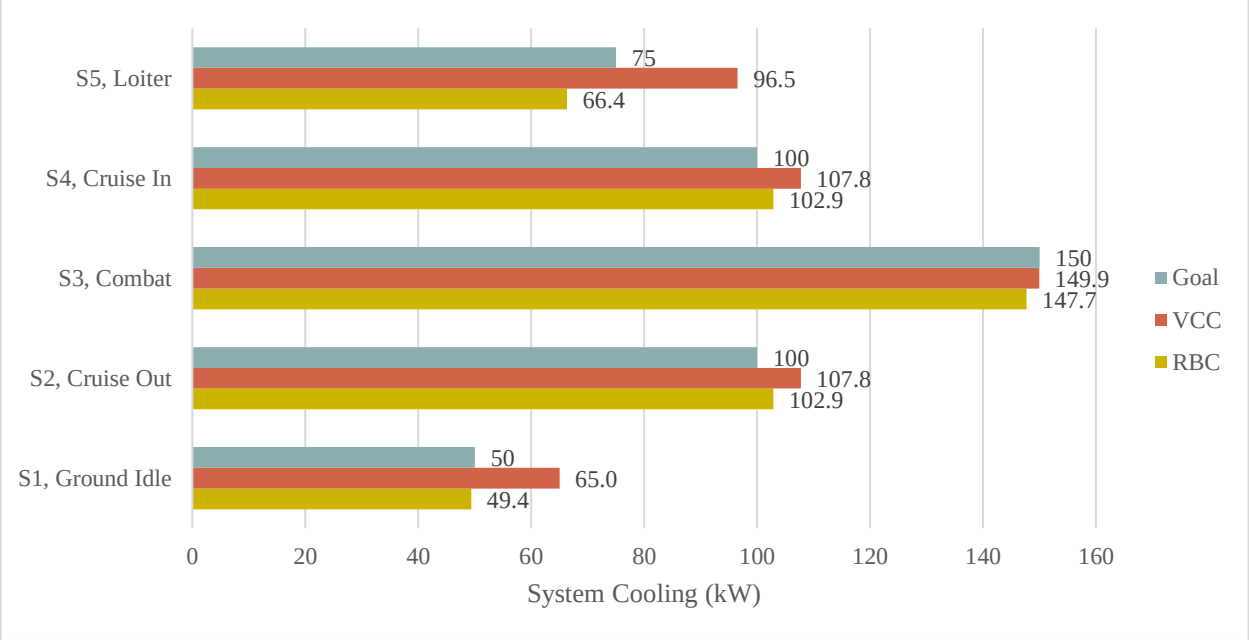

Figure 4.5. System Cooling Performance for Both Systems Compared to the Performance Goal, Mission 1

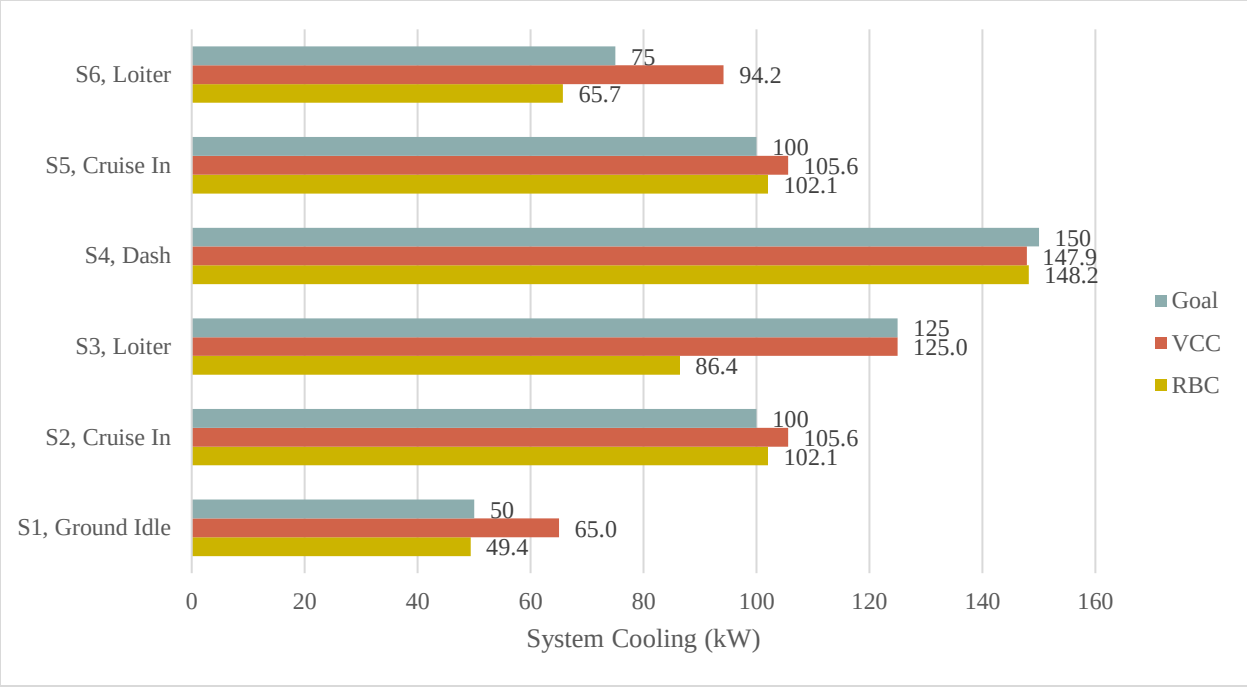

Figure 4.6. System Cooling Performance for Both Systems Compared to the Performance Goal, Mission 2

Source outlet temperature for both systems is presented in Figure 4.7 for all sections of Mission 1 and in Figure 4.8 for all sections of Mission 2. Note that the goal source outlet temperature was 20°C for all mission sections. Similar trends to what was observed in the system cooling performance can be seen in both figures, with the VCC cooling as much as 10.9°C below the 20°C goal to ensure the refrigerant entering the compressor has 8°C of superheating. The RBC shortfall during both loiter conditions, Segment 5 in Mission 1 and Segments 3 and 6 in Mission 2, is demonstrated more clearly in the source outlet temperature, with the temperature exceeding the goal by 3.5°C during Mission 1 Segment 5, and as much as 10.5°C during Mission 2 Segment 3.

In practice, the VCC's overcooling may not be realistic since the amount of achievable cooling can at most be the heat load introduced by the electronics. If the source boundary condition was changed to an electronics loop with a fixed heat load instead of a fixed source inlet temperature, the VCC would have likely not achieved the required 8°C of superheating, and another source of additional heat, such as a heater, may be needed.

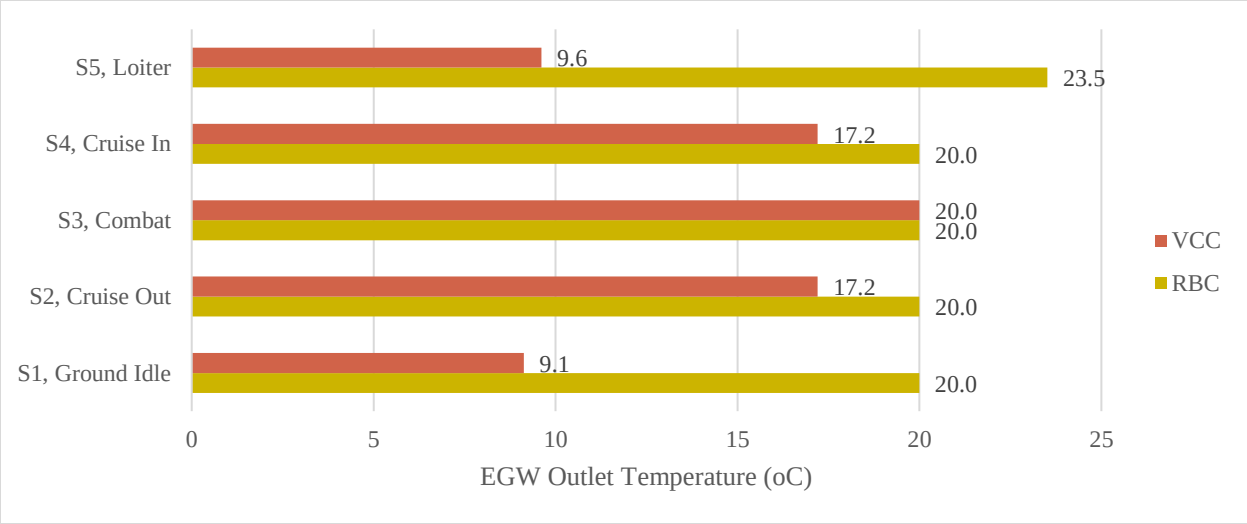

Figure 4.7. Source Outlet Temperature for Both Systems, Mission 1

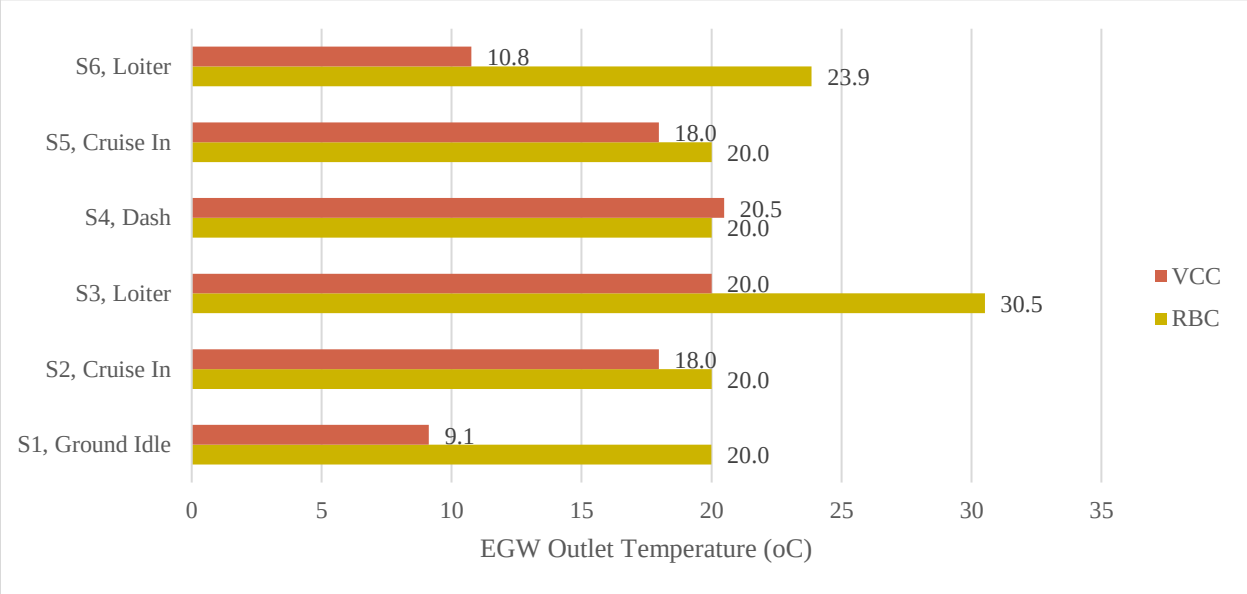

Figure 4.8. Source Outlet Temperature for Both Systems, Mission 2

The operational limitations of the HFC-134a refrigerant used in the VCC is demonstrated by reviewing the T-s diagram from Mission 2 Segment 4, which is presented in Figure 4.9. As seen in the figure, the refrigerant in the condenser is approaching the top of the vapor dome, indicating that the refrigerant is close to the critical point. At this condition, the condenser saturation temperature was 96.7ºC, which is 4.4ºC from the refrigerant's 101.1ºC critical

temperature. Conditions with higher sink temperatures, which would occur if the aircraft speed was increased beyond 0.75 Mach, would not be achievable with a traditional subcritical VCC using HFC-134a since the critical temperature would be exceeded. The RBC does not have a similar limitation since air is the working fluid, and is instead restricted by temperature and pressure limits of the system components.

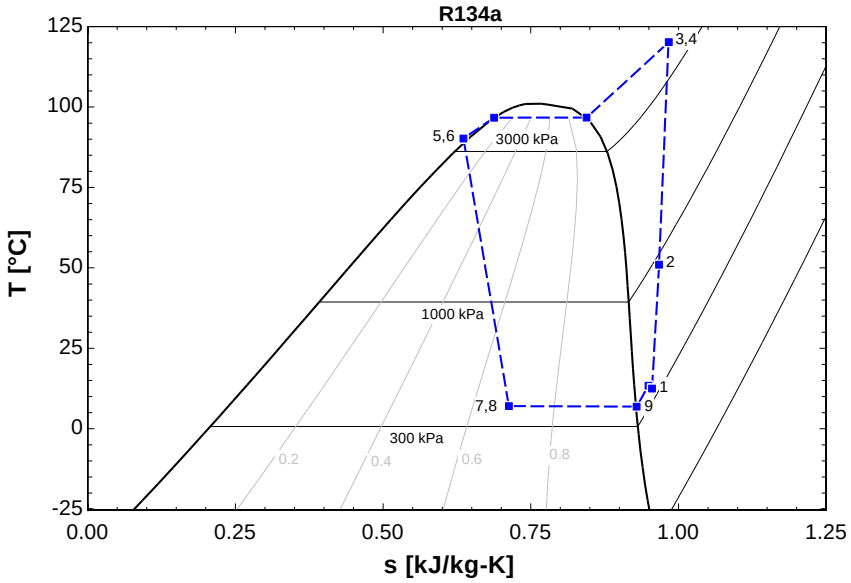

Figure 4.9. Mission Two, Segment Four, T-s Diagram

Full results at each system state point are presented in Table Error! **No text of specified style in document.**.8 for the VCC and for the RBC. T-s and P-h plots of the VCC for all Segments are presented in Figure Error! **No text of specified style in document.**.17 through Figure Error! **No text of specified style in document.**.32. System convergence was checked using mass and energy balances, which are presented in Table Error! **No text of specified style in document.**.7 for the VCC and Table Error! **No text of specified style in document.**.21 for the RBC.

4.2.3 Tactical Aircraft Cooling System Energy Based Analysis Results

The performance of both systems can be compared on a First Law energy basis. The coefficient of performance quantifies how effectively the TMS utilizes the supplied energy for cooling, and the values for both systems are presented in Figure 4.10 and Figure 4.11 for Missions 1 and 2 respectively. As seen in the figures, the RBC COP was overall much lower than the VCC

COP. The RBC ranged from 0.23 during Mission 2 Segment 4, low altitude dash, to at most 0.580 during Mission 2 Segment 3, high altitude loiter. The VCC COP remained above 1 for all segments, and ranged from 1.07 during Mission 2 Segment 4 to 6.28 during Mission 1 Segment 5. These results indicate the VCC produced at least as much cooling as the work inputted to the system, while the RBC produced less cooling than work inputted to the system.

Both system's COP was dependent on the ambient conditions and heat load, but the RBC had less variance than the VCC. Ambient condition dependence can be demonstrated by reviewing Mission 1 Segment 2 and Mission 2 Segment 2 results. Both segments had a 100kW heat load, but the Mission 1 Segment 2's ram air sink temperature was 8ºC higher and the ram air flow was higher, as seen in Table 4.5. The RBC's COP was 0.02 lower for the higher sink temperature segment, but the VCC's COP was 0.65 lower. This trend is because the RBC's energy input is in the form of engine compression work, which has much larger magnitude than the heat load, and results in less variance of the COP. Since the VCC work input is being used to directly cool the heat load, the source and sink conditions have a greater impact on system COP.

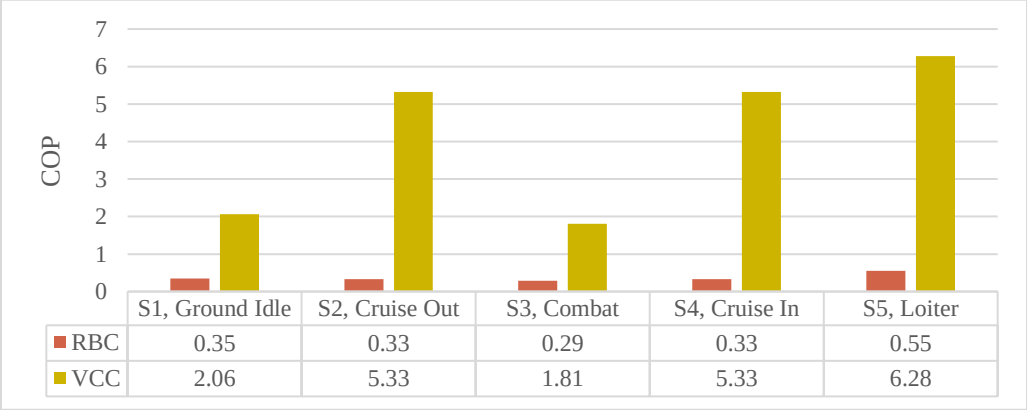

	S1, Ground Idle	S2, Cruise Out	S3, Combat	S4, Cruise In	S5, Loiter
RBC	0.35	0.33	0.29	0.33	0.55
VCC	2.06	5.33	1.81	5.33	6.28

Figure 4.10. Coefficient of Performance of Both Systems for Mission 1

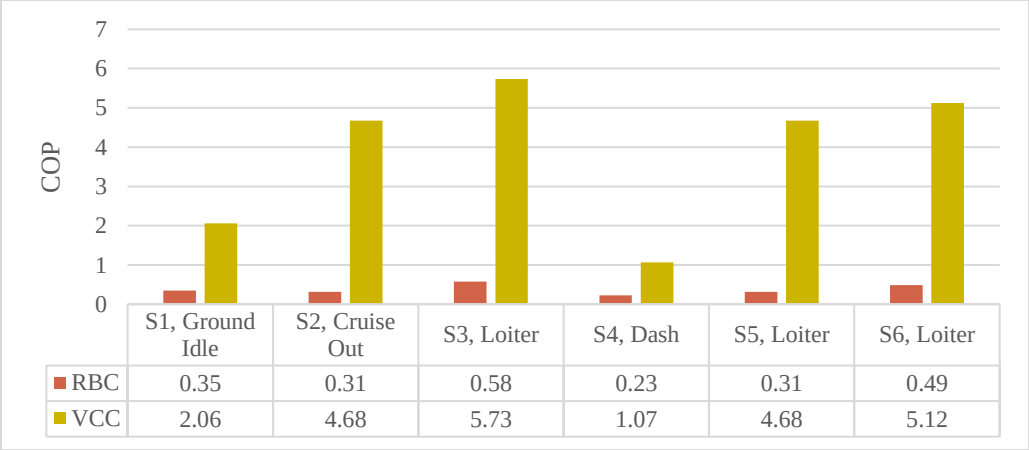

Figure 4.11. Coefficient of Performance of Both Systems for Mission 2

While the COP results of both systems show how effectively the systems use the supplied energy for cooling, they do not fully capture the energy-based impact of the cooling system on the aircraft. Each system has their own impact on the engine, since the work inputted to the RBC is a byproduct of the already available engine propulsion system compression work, while the VCC work input requires engine power take-off. Consequently, an energy-based aircraft cooling system impact analysis was applied to both systems to better capture the effects of both systems on the aircraft.

Inputs to the analysis were total system weight, ram air sink mass flow rates, bleed air mass flow rates for the RBC and compressor power for the VCC. Detailed breakdowns of all input parameters are presented in 0 for the VCC and 0 for the RBC. These parameters were inputted to the equations described in Section 3.5.2, using the F-15 specific fuel consumption values at the corresponding ambient conditions from Section 3.5.1.

The resultant total fuel penalties for both systems summed for each segment in Mission 1 and 2 are presented in Table 4.6 and Figure 4.12. As seen in the table, the RBC has a higher fuel impact to the aircraft than the VCC for both missions. Reviewing the breakdown, it can be seen that despite the VCC's higher system weight impact and ram air impact, the RBC's bleed air impact requires more fuel to address than the VCC's power take-off impact. For Mission 1, the bleed air fuel impact was over two times the power take-off impact. For Mission 2, the bleed air impact was over three times the power take-off impact. Note that the expendable material usage was zero for both systems. Detailed results for all segments are presented in Table Error! **No text**

of specified style in document..9 for the VCC and Table Error! **No text of specified style in document.**.23 for the RBC.

These trends are a result of the cost of each system's energy source on the engine. Since RBC bleed air directly pulls from the engine air flow, it has a greater SFC increase than the VCC, since power take-off comes from an engine driven gearbox. This is demonstrated in the shaft power factor equation in (3-21). Since k_{pwr} is always less than 1, $(SFC)_{TH}$ is always more than $(SFC)_{pwr}$, meaning every kg/s of bleed air flow taken from the engine increases fuel flow more than every Watt of power supplied by the engine. Due to the heat loads involved, as well as the SFC and k_{pwr}'s dependence on altitude and Mach number, the RBC's lower weight and ram air usage impacts are negated by the increased cost of bleed air compared to power take-off.

These dependencies are well demonstrated by comparing the low heat load ground idle condition, Mission 1 and Mission 2 Segment 1, to the high heat load combat and dash conditions, Mission 1 Segment 3 and Mission 2 Segment 4. During ground idle, the RBC's bleed air impact was 16kg of fuel versus the VCC's power impact of 21kg of fuel, showing that the VCC has a greater impact at this point due to the low altitude and low heat load conditions. However, during low altitude, high speed dash, the RBC's bleed air impact is 45 kg of fuel, while the VCC's power impact is 9 kg of fuel. Similarly, during high altitude, high speed combat, the bleed air impact is 14kg of fuel, while the VCC's power impact is 4kg of fuel.

The energy-based results must be caveated with the fact that the model used to determine $(SFC)_{pwr}$ was not F-15 specific, and was instead based on a study of multiple turbofan engines [23]. While the model used a turbofan power factor applied to F-15 specific $(SFC)_{Th}$ values, the correlation between $(SFC)_{Th}$ and $(SFC)_{pwr}$ may not be as simple as a generic multiplier that is only dependent on altitude and Mach number.

Table 4.6. Fuel Penalty Breakdown for Both Cooling Systems for All Mission Segments

Fuel Penalty	**RBC, Mission 1**	**VCC, Mission 1**	**RBC, Mission 1**	**VCC, Mission 2**
System Weight Total (kg Fuel)	6.77	10.97	14.31	23.19
Ram Air Total (kg Fuel)	28.75	34.78	70.80	85.65
Bleed Air Total (kg Fuel)	81.01	0	153.30	0

Power Take-Off Total (kg Fuel)	0	37.09	0	50.79
Total Fuel Penalty (kg Fuel)	116.54	82.84	238.41	159.63

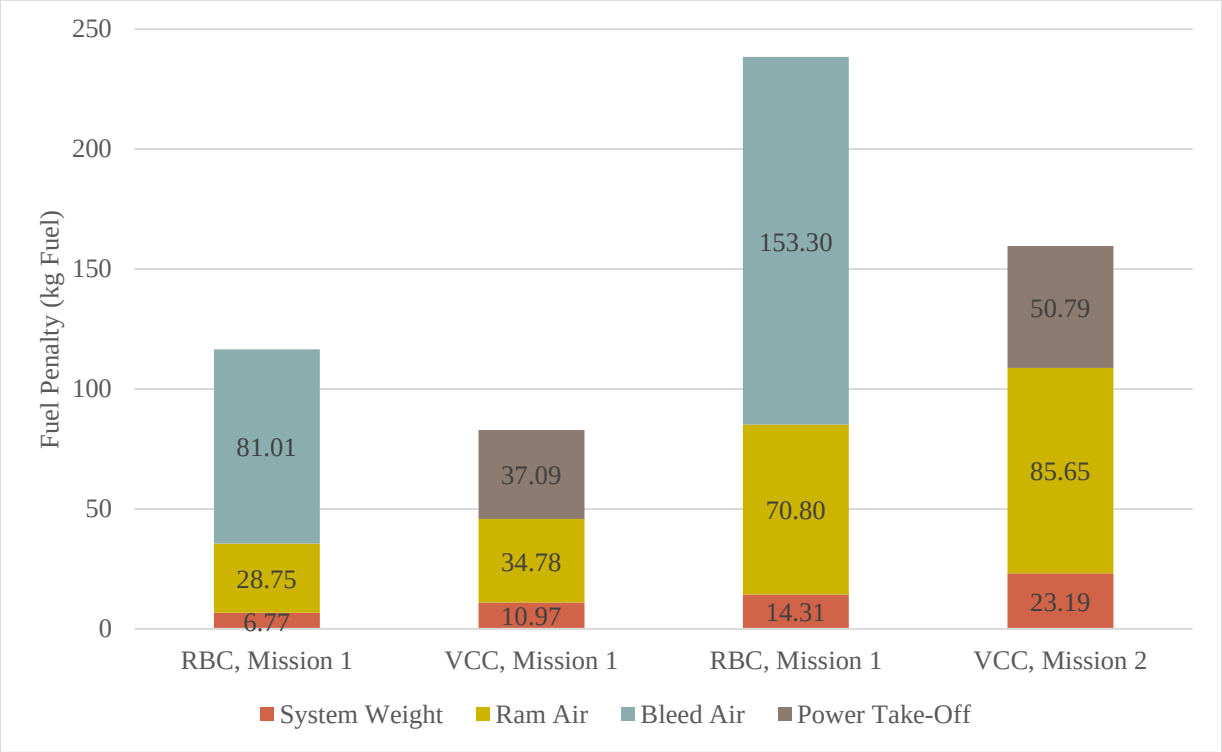

Figure 4.12. Total Fuel Penalty for Both Cooling Systems during both Missions

4.2.4 Tactical Aircraft Cooling System Exergy Based Analysis Results

The performance of both systems can also be compared on a Second Law exergy basis using a global exergy analysis. The total exergy destroyed by both systems can be computed by summing the exergy flows into and out of the systems. A detailed breakdown of the exergy flows is presented in 0 for the RBC and 0 for the VCC. The resulting total exergy destroyed by both systems during Mission 1 and Mission 2 is presented in Figure 4.13 and Figure 4.14 respectively. As seen in the figures, the largest amount of exergy was destroyed during the most demanding segments, Segment 3 for Mission 1 and Segment 4 for Mission 2. The RBC destroyed more exergy than the VCC during all segments in both missions, destroying 406kW of exergy more than the VCC during Mission 1 Segment 3, and 483.5kW more than the VCC during Mission 2 Segment 4.

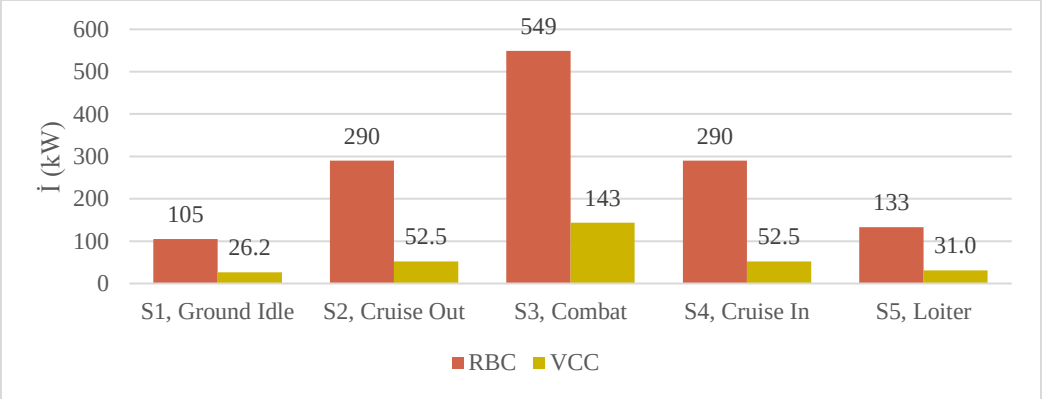

Figure 4.13. Total Exergy Destroyed by Both Systems during Mission 1

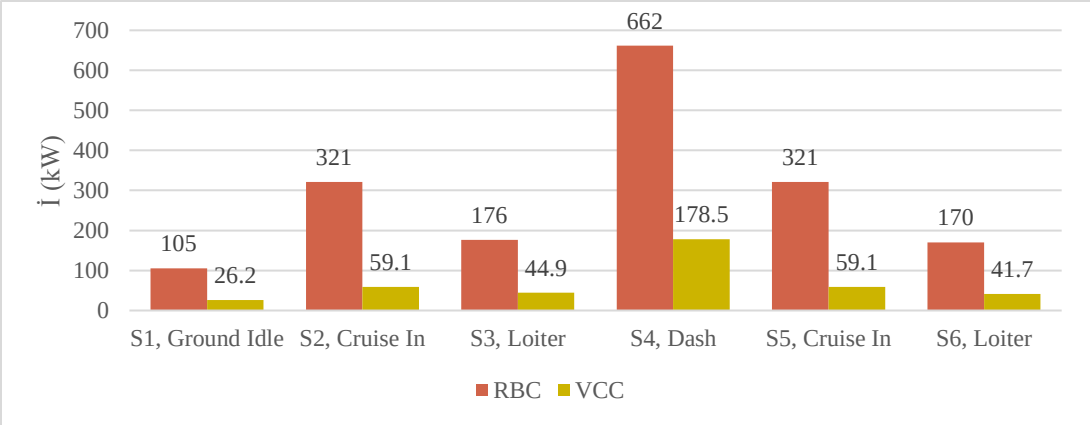

Figure 4.14. Total Exergy Destroyed by Both Systems during Mission 2

The exergy efficiency of the system can then be determined by dividing the exergy of the cooled EGW flow leaving the system by the exergy supplied to the thermal management system to cool this flow. The results for both systems are presented in Figure 4.15 and Figure 4.16 for Missions 1 and 2 respectively. As seen in the figures, the VCC exergy efficiency is higher than the RBC exergy efficiency for all segments of both missions. In Mission 1, the difference between the RBC and VCC exergy efficiency is largest during Segments 2 and 3, while the difference is smallest during Segments 3 and 4. In Mission 2, the difference between the RBC and VCC exergy efficiency is largest during Segment 1, while the difference is smallest during Segments 6.

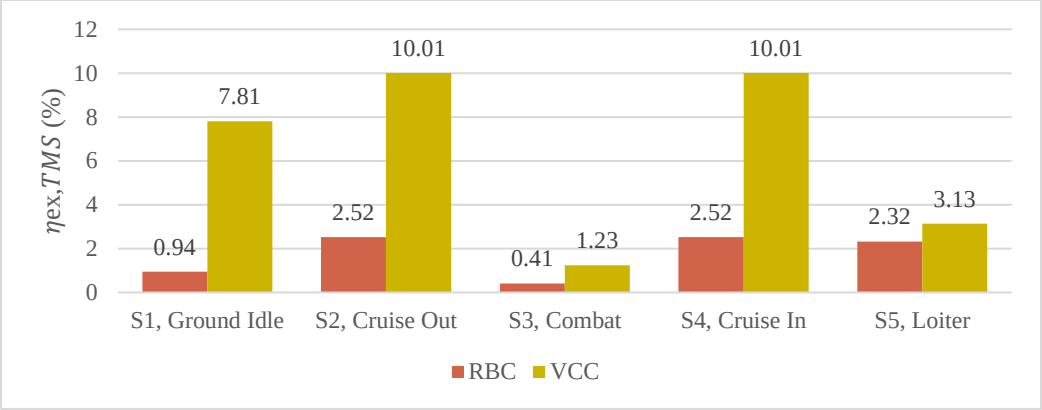

Figure 4.15. Exergy Efficiency of Both Systems during Mission 1

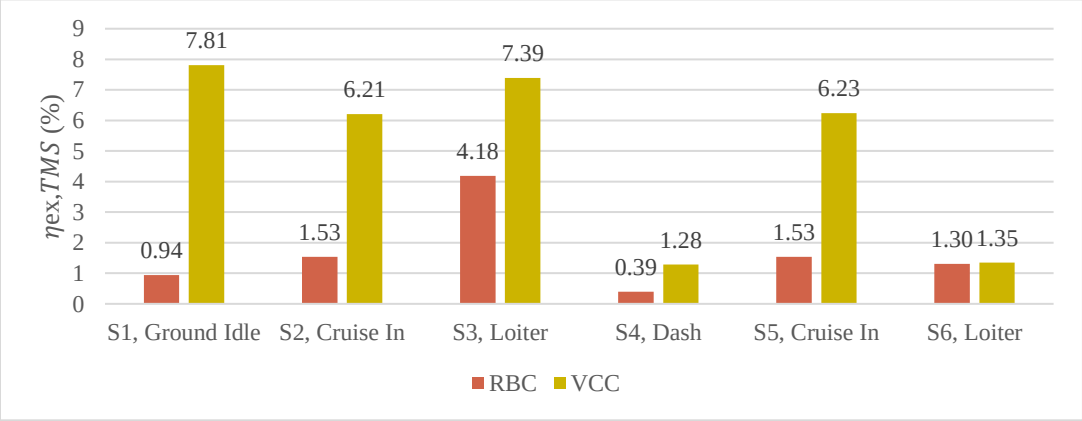

Figure 4.16. Exergy Efficiency of Both Systems during Mission 2

These exergy destruction and exergy efficiency trends are best explained by differences in the types of power used by the RBC and VCC to cool the load, how efficiently each system uses this power, and the thermodynamic phenomenon each system utilizes during operation. Reviewing the detailed flow breakdown in Table Error! **No text of specified style in document.**.10 and Table Error! **No text of specified style in document.**.11, the largest source of exergy for the VCC is the work entering the system to power the compressors, then the ram air flow into the system; for Mission 2 Segment 4, compressor work input was 138.4kW and ram air flow exergy was 103.4kW. Similarly for the RBC, Table Error! **No text of specified style in document.**.24 and Table Error! **No text of specified style in document.**.25 show that the largest source of exergy for the RBC is the bleed air flow into the system, then the ram air flow into the system; for Mission 2 Segment 4, the bleed air flow exergy was 622.4kW and the ram air flow exergy was 210kW. For all mission

segments, the bleed air exergy flow into the RBC was much larger than work supplied to power the VCC. This difference directly translates to the exergy efficiency discrepancy between both systems; during Mission 2 Segment 4, the VCC exergy efficiency of 1.28% was over 3 times larger than the RBC's 0.39%. This trend demonstrates that the VCC requires less exergy and therefore useful energy to cool the same load than the RBC, even at the highest demand point.

Similar to the energy-based results, the exergy-based results must be caveated with the fact that a detailed engine power take-off model was not used in the study. There are additional losses between the power produced by the engine and power supplied to the VCC, such as gearbox losses and power transmission losses, and which will increase the amount of exergy destroyed by the system.

A local exergy analysis was also performed on a component level basis to determine the component, or group of components that destroy the most system exergy, as well as to demonstrate why the RBC destroys a larger amount of exergy than the VCC. To choose segments for detailed component level analysis, the components of both systems were first grouped into four categories, heat exchangers, turbomachinery, valves and ducts/lines. The results show the percentage of the system exergy destroyed by each set of components. Data for the RBC is presented in Figure 4.17 and Figure 4.18 for Missions 1 and 2 respectively, and data for the VCC is presented in Figure 4.19 and Figure 4.20 for Missions 1 and 2 respectively. Complete results for the component level VCC exergy analysis can be found in Table Error! **No text of specified style in document.**.12 and Table Error! **No text of specified style in document.**.13 for missions 1 and 2 respectively. Complete results for the component level RBC exergy analysis can be found in Table Error! **No text of specified style in document.**.26 and Table Error! **No text of specified style in document.**.27 for missions 1 and 2 respectively.

For the RBC, the heat exchangers make up the largest portion of the destroyed exergy during all segments, but the second largest portion varies depending on the section. The turbomachinery destroys the second largest portion during Mission 1 Segments 1 and 5, as well as during Mission 2 Segments 1, 3, and 6. The valves destroy the second largest portion during Mission 1 Segments 2 and 3, as well as during Mission 2, Segments 2, 4 and 5. The ducts destroy the smallest portion during all segments, except during Mission 1 Segment 5 and Mission 2 Segment 6.

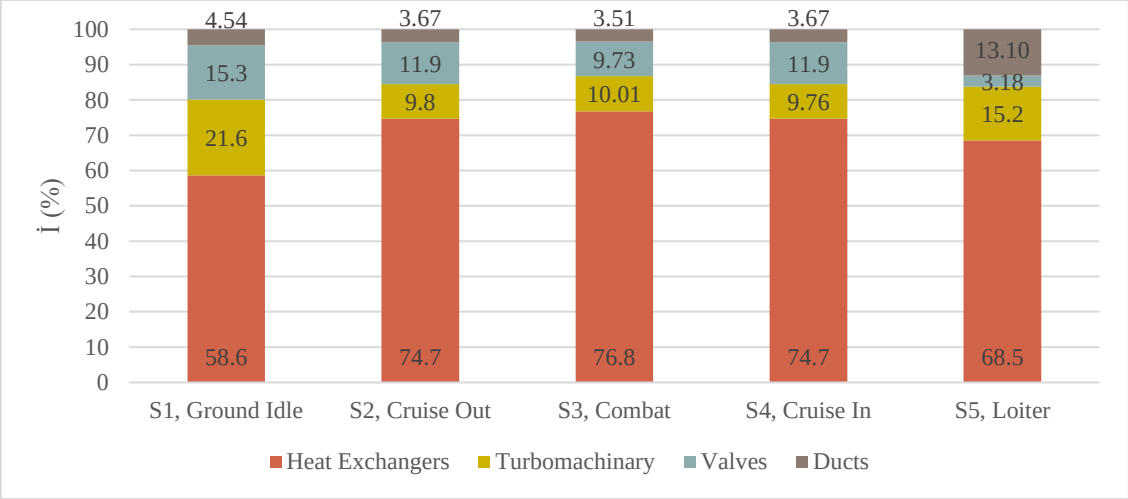

Figure 4.17. Exergy Destroyed as a Percentage of the Total by Each Component Category for the Reversed Brayton Cycle System, Mission 1

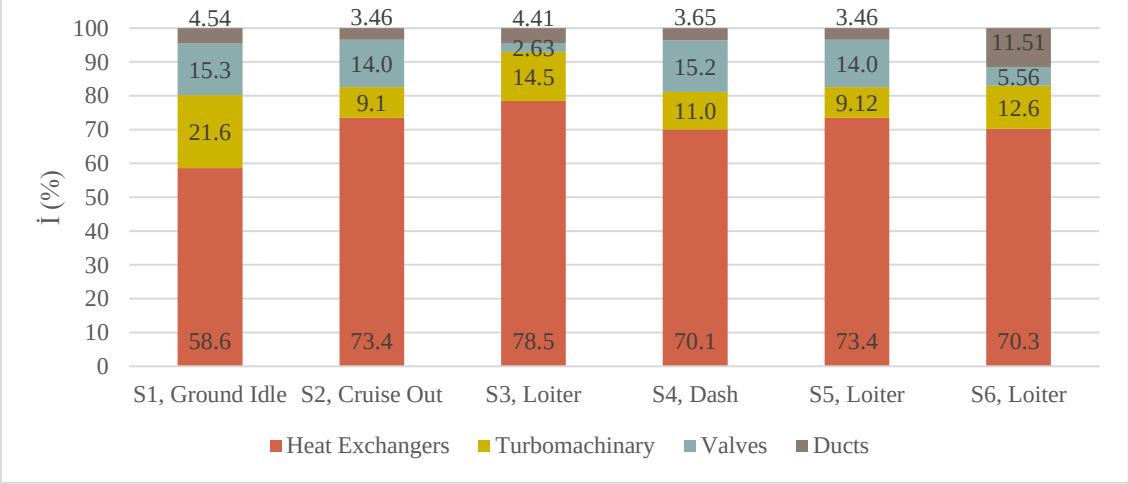

Figure 4.18. Exergy Destroyed as a Percentage of the Total by Each Component Category for the Reversed Brayton Cycle System, Mission 2

For the VCC, the heat exchangers also make up the largest portion of the destroyed exergy during all segments, and the second largest portion also varies depending on the section. The turbomachinery destroys the second largest portion for most Segments, except during Mission 1 Segments 1 and 3, as well as during Mission 2 Segments 1 and 4. The valves destroy the second largest portion during Mission 1 Segments 1 and 3, as well as during Mission 2, Segments 1 and 4. The lines destroy the smallest portion during all segments.

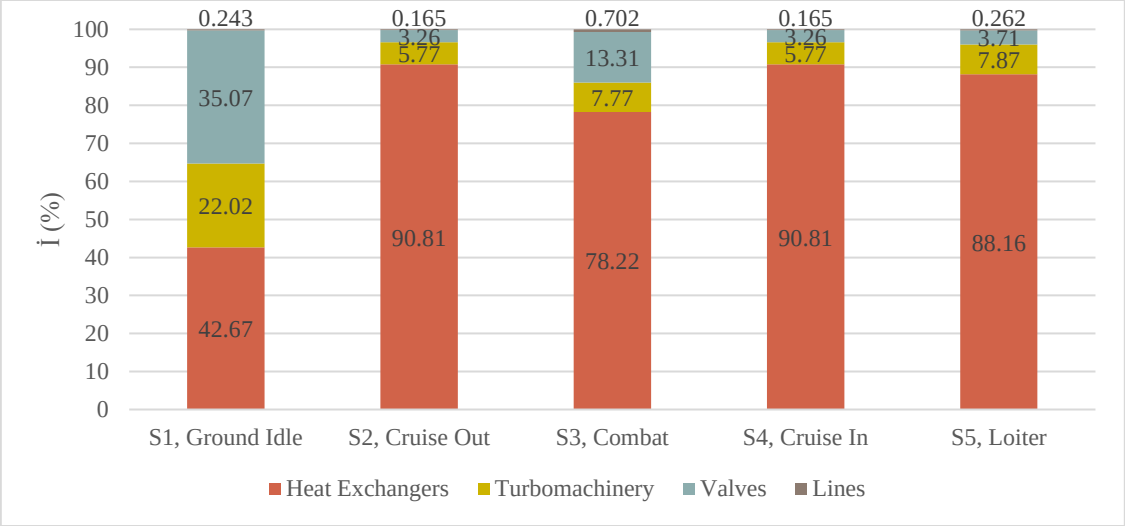

Figure 4.19. Exergy Destroyed as a Percentage of the Total by Each Component Category for the Vapor Compression Cycle System, Mission 1

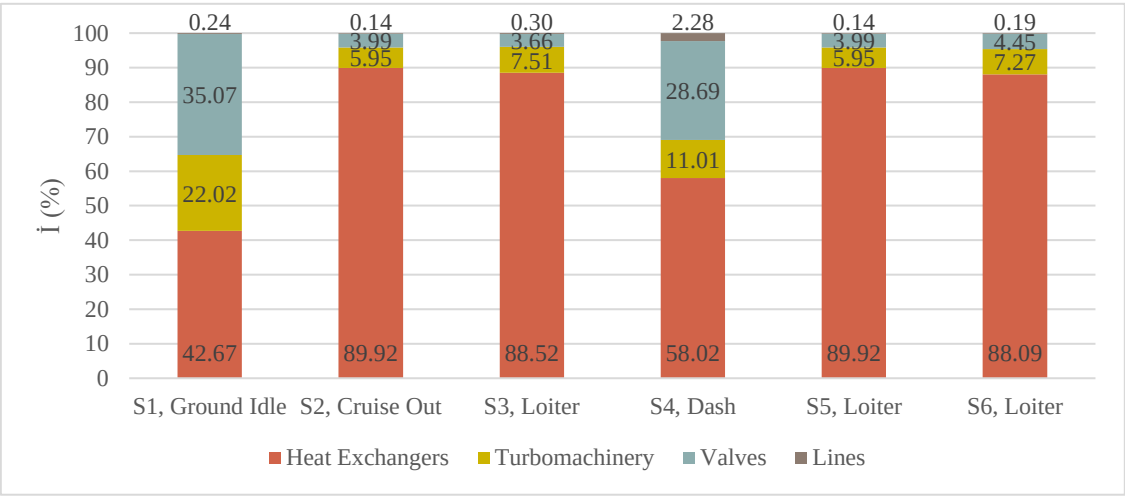

Figure 4.20. Exergy Destroyed as a Percentage of the Total by Each Component Category for the Vapor Compression Cycle System, Mission 2

Based on these results, Mission 1 Segment 1 and Mission 2 Segment 4 were chosen for further component level analysis. Both segments were chosen due to the variance of the valve losses in the VCC, as well as to capture the point of lowest exergy destruction (Mission 1 Segment 1) and highest exergy destruction (Mission 2 Segment 4).

For Mission 1 Segment 1, a breakdown of all components that destroyed 1% or more of the total exergy destroyed is presented in Figure 4.21 for the RBC and Figure 4.22 for the VCC. As

seen in Figure 4.21, the RBC primary heat exchanger destroys the most exergy, followed by the bleed air valve, the secondary heat exchanger, and the compressor. Because the flow entering the RBC is high temperature engine bleed air, large amounts of exergy are destroyed by the PHX and SHX to bring the air down to a usable temperature. Furthermore, the bleed air valve destroys a large amount of exergy in the form of pressure drop to drive the flow through the system. Also, of note is the 3% exergy destroyed by the duct between the bleed air valve and primary heat exchanger, which consists entirely of pressure losses, and is equal to the percentage destroyed by the reheater and condenser. As seen in Figure 4.22, the VCC condenser destroys the most exergy, followed by the hot gas bypass and mixing, then a three way tie between evaporator 1, evaporator 2, and the compressor stage 1. The condenser destroys the most exergy due the irreversibility inherent in heat transfer.

When comparing the amount of exergy destroyed by the RBC and VCC heat exchangers during Mission 1 Segment 1, the RBC PHX and SHX destroy 34.2kW and 12.3kW of exergy, while the condenser only destroys 4.8kW of exergy. While both systems utilize pressure drop to bring the working fluid below the source temperature and absorb heat, the RBC utilizes single phase air as the working fluid and the VCC utilizes multi-phase HFC-134a refrigerant. Bringing the air below the sink temperature requires a large pressure drop, which is achieved by driving the air pressure high. In order to reach this high pressure, there must be a correspondingly large increase in temperature since the air remains in the gas phase. The temperature must be dropped in order to bring the air to the required turbine outlet temperature, thus resulting in large losses due to irreversible heat transfer. The VCC requires a larger pressure drop to achieve this cooling, but the temperature range is not as large since the refrigerant changes phase. Additionally, the VCC requires less mass flow to achieve the same heat transfer as the RBC due to the much larger heat transfer coefficient during phase change, versus air's comparatively low heat transfer coefficient.

From a second law efficiency standpoint, the PHX and SHX efficiencies are 24% and 6% respectively, while the condenser's is 39%. Similar trends can be observed by comparing the RBC LHX's 8.6kW to the VCC Evaporator 1 and 2 combined irreversibility of 6.3kW, even though both heat exchangers are cooling a similar heat load. The LHX's second law efficiency is 13%, while the evaporators' are 77%.

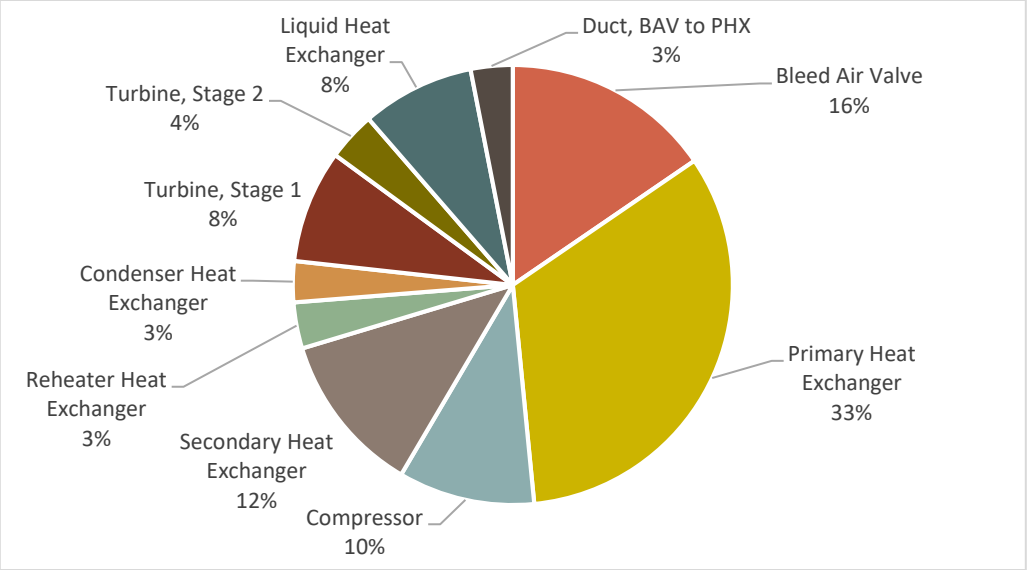

Figure 4.21. Percentage of Total Exergy Destroyed by Each Component in the Reversed-Brayton Cycle System during Mission 1 Segment 1

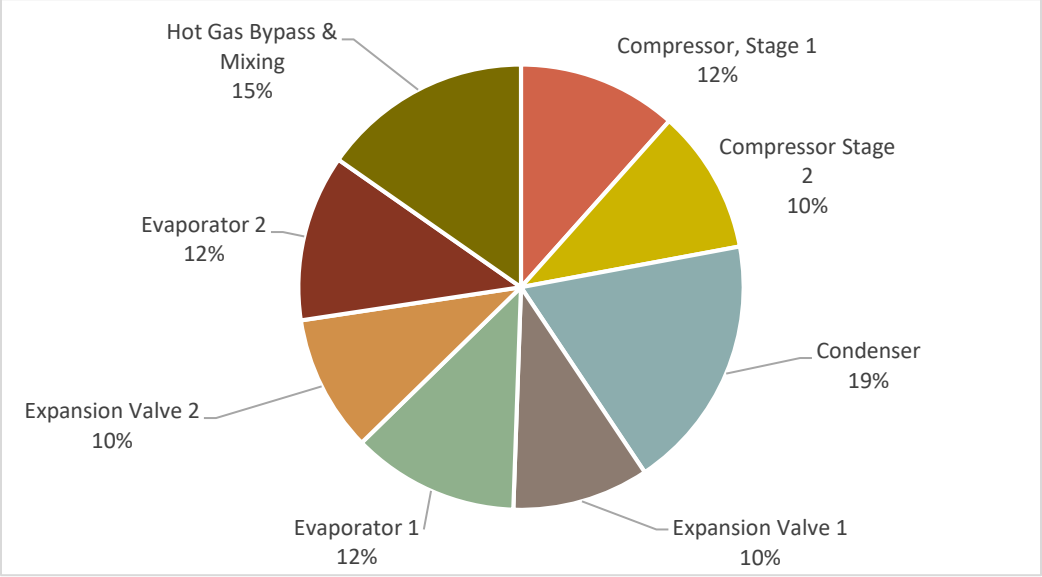

Figure 4.22. Percentage of Total Exergy Destroyed by Each Component in the Vapor Compression Cycle System during Mission 1 Segment 1

Similarly for Mission 2 Segment 4, a breakdown of all components that destroyed 1% or more of the total exergy destroyed is presented in Figure 4.23 for the RBC and Figure 4.24 for the VCC. As seen in Figure 4.23. The primary heat exchanger destroys the most exergy, followed by the secondary heat exchanger and the bleed air valve. Again, 3% of the exergy was destroyed by the

duct between the bleed air valve and primary heat exchanger, which is equal to the percentage destroyed by turbine stage 2 and greater than the percentage destroyed by the reheater.

As seen in Figure 4.24, the VCC condenser destroys the largest percentage of the exergy, followed by a two-way tie between evaporator 1 and evaporator 2, and compressor stage 1. These results contrast with the VCC results from Mission 1 Section 1 where the hot gas bypass and mixing was the second largest percentage of the total exergy destroyed. This is because the system is cooling 50kW instead of the 150kW design condition load. As a result, the system requires significant hot gas bypass flow to achieve 8^{o}C of superheating and protect the compressor from liquid ingestion.

Similar trends in destroyed exergy and 2nd law efficiency can be observed during this segment as from Mission 1 Segment 1. The RBC PHX, SHX and LHX destroy 257kW, 113kW, and 38kW of exergy respectively, while the VCC condenser and evaporator 1 and 2 destroy 88kW and 16kW combined of exergy respectively. The RBC PHX, SHX and LHX have a 2nd law efficiency of 2%, 52%, and 8% respectively, while the VCC condenser and evaporator 1 and 2's efficiencies are 91% and 83% respectively.

The results of the exergy-based local analysis can be used to identify specific cooling system components that may need optimization to reduce irreversibilities. For example, the heat exchangers make up the largest percentage of exergy destroyed during all mission segments for both systems. As a result, improvements should be explored for the heat exchangers to reduce losses, such as enhancing heat transfer effectiveness or reducing pressure drop.

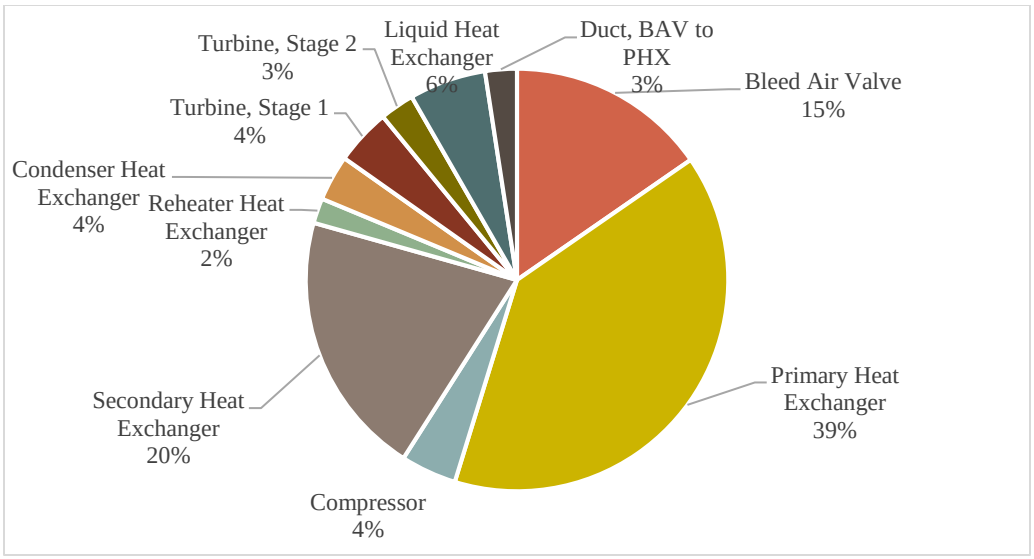

Figure 4.23. Percentage of Total Exergy Destroyed by Each Component in the Reversed-Brayton Cycle System during Mission 2 Segment 4

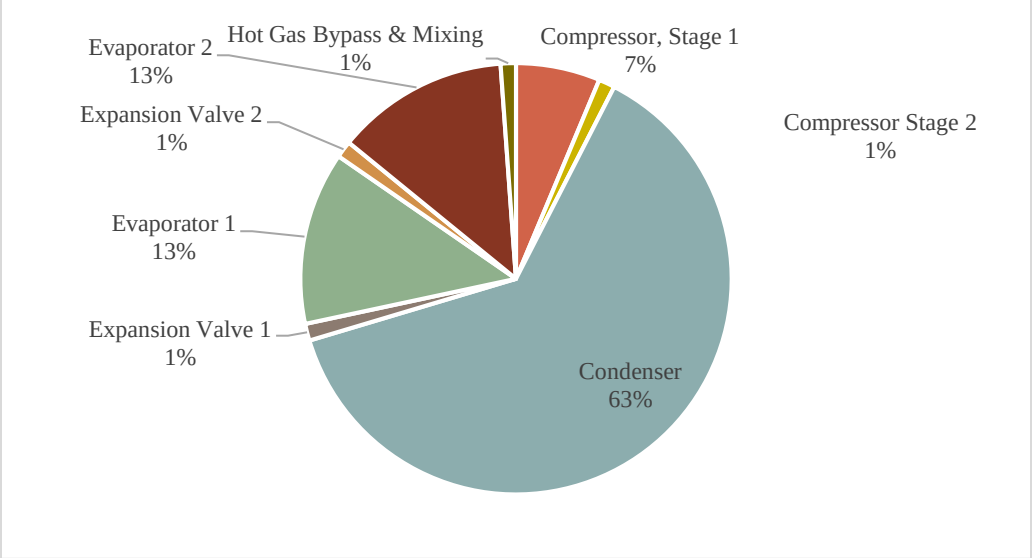

Figure 4.24. Percentage of Total Exergy Destroyed by Each Component in the Vapor Compression Cycle System during Mission 2 Segment 4

5. CONCLUSIONS AND FUTURE WORK

This thesis demonstrated the performance of VCC and RBC cooling systems for aircraft avionics thermal management using detailed component models during two tactical aircraft relevant missions, and compared the performance using an energy-based and exergy-based aircraft impact analysis. The VCC had better performance than the RBC, and met the thermal load goal at all points, but tended to cool the source EGW below the desired 20^{o}C outlet temperature due to compressor inlet flow protections. This overcooling may not be achievable in practice if more realistic heat load boundary conditions are introduced. The HFC-134a refrigerant prevented the aircraft from operating at ram air temperatures that would drive the condenser saturation temperature higher than the critical temperature, which can occur during high speed and/or low altitude conditions. The RBC met the thermal load during most mission segments, but failed to meet the thermal load goal at points of low ambient pressure, which can occur during low speed conditions.

On an energy basis, the VCC made better usage of the supplied energy than the RBC, having a higher COP during all mission segments. The VCC also had a lower fuel impact to the aircraft than the RBC for all flight segments, and only exceeded the RBC's fuel impact during the ground idle segment. Based on these results, it can be concluded that even though the VCC weights more than the RBC and requires more ram air, it has a lower impact during flight than the RBC. This is because of the lower impact of the energy it uses to cool the thermal load on engine fuel flow. During most flight conditions, bleed air requires more fuel flow than power take-off to compensate for the lost engine thrust, and the difference increases as the aircraft increases in airspeed and altitude.

On an exergy basis, the VCC also destroyed less exergy than the RBC during all mission segments. The VCC tended to use the exergy supplied to the system to cool the load more effectively than the RBC. The VCC components also tended to have lower irreversibilities and higher exergy efficiencies than the RBC components due to the system method of operation. The VCC makes use of the both sensible and latent heat transfer and the refrigerant's boiling heat transfer coefficient during phase change, while the RBC only utilizes latent heat transfer and air's low heat transfer coefficient. From these results, it can be concluded that the VCC has less irreversibility than the RBC, and as a result requires less exergy to cool the same load.

A limitation of the study was the RBC system's air humidity model. Due to inconsistent model results related to very low system temperature, which were lower than the validation system temperatures, the tactical aircraft model was analyzed on a dry air basis. Further studies should incorporate an improved humidity model without these limitations. The model should also incorporate entrained moisture evaporation, which may improve the RBC system's heat exchanger performance. System controls, such as compressor and turbine outlet temperature limits to prevent material damage or ice formation, should also be added to ensure the system performance is more realistic.

In order to ensure the aircraft is not operationally limited, alternative refrigerants and system architectures should also be explored. HFC-134a's low critical temperature limited the sink temperature, and therefore aircraft altitude and airspeed. Some refrigerants that may be better suited to the high sink temperatures encountered by a tactical aircraft VCC include HFC-245fa, which has a critical temperature of 154^{o}C, or low GWP alternatives such as HFO-1233zd(E) or HFO-1336mzz(Z), which have a critical temperature of 165.5^{o}C and 171.3^{o}C respectively. Alternatively, the system architecture could be modified to make use of fuel or phase change material as the sink, allowing the condenser temperature to remain low during points of high ram temperatures.

Finally, combined RBC and VCC architectures should be explored. A drawback of the fully VCC TMS presented in the thesis is it cannot supply fresh air to the cabin. A small RBC would need to be added to supply the necessary fresh air. A larger RBC could also be incorporated as the VCC's sink, which would then sink to the ram air. Since the RBC would not have the critical temperature limitation of the VCC, it would not operationally limit the aircraft. Additionally, because the RBC supplies air to the condenser at a lower temperature than the than ram air, it could increase the VCC COP and reduce system size and weight.

Overall, the VCC met the cooling performance goals better than the RBC, and both the energy and exergy-based methods demonstrated that the VCC had a lower fuel impact to the aircraft and destroyed less exergy than the RBC. Improved boundary conditions and additional losses should be included to make a more realistic comparison of both systems. The results presented in this thesis demonstrate some of the benefits of VCC thermal management systems over traditional RBC systems for tactical aircraft avionics cooling, and additional studies should be pursued to further explore these benefits.

APPENDIX A. VAPOR COMPRESSION CYCLE MODEL DETAILS

A.1 System Model Diagrams

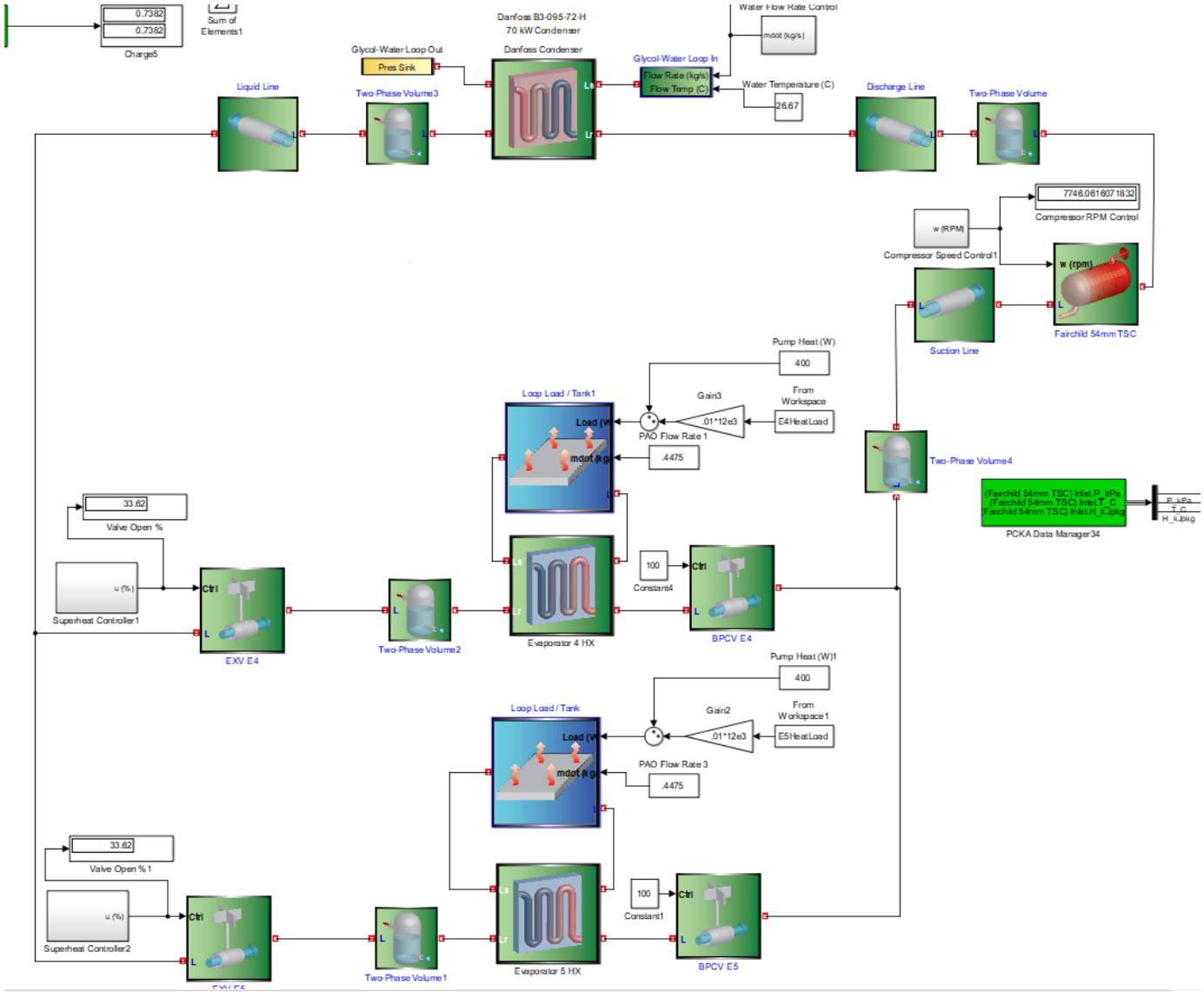

Figure **Error! No text of specified style in document.**.1. Verification and Validation System Model

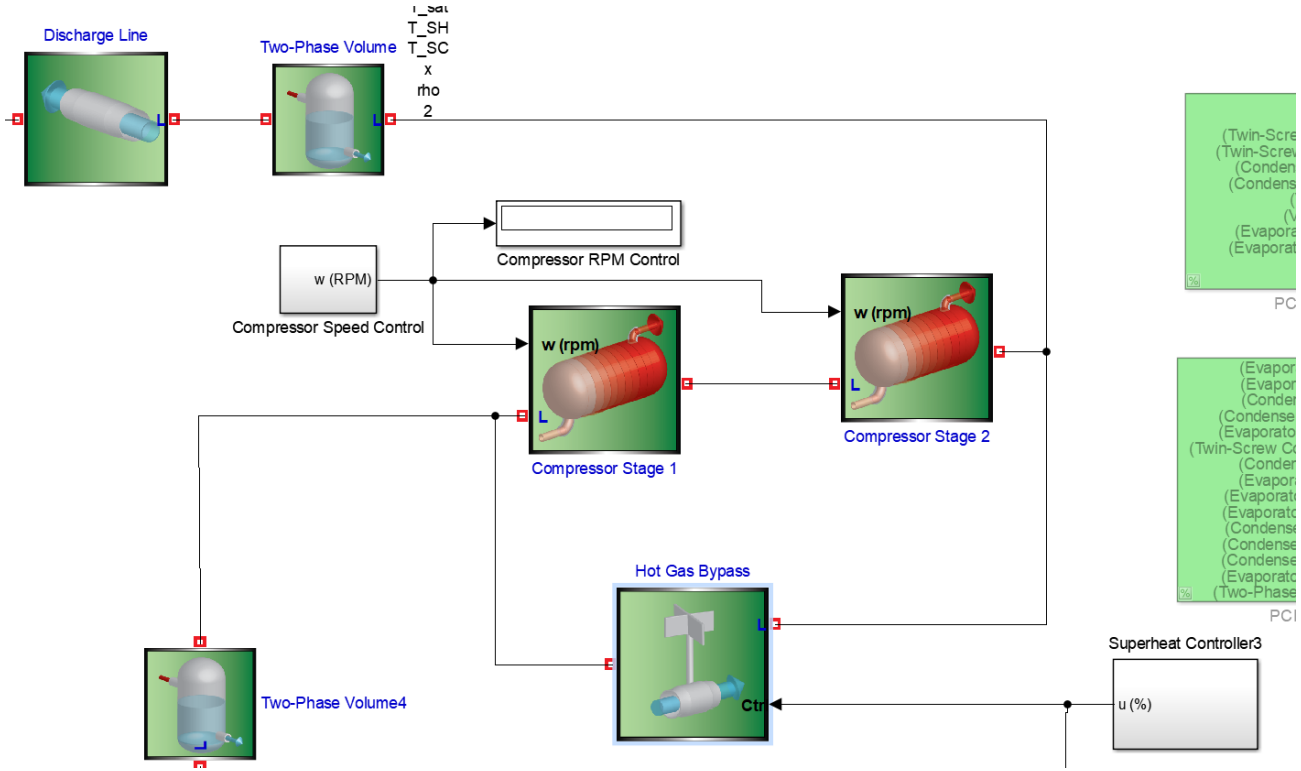

Figure **Error! No text of specified style in document.**.2. Tactical Aircraft Model System Model Diagram, Compressors

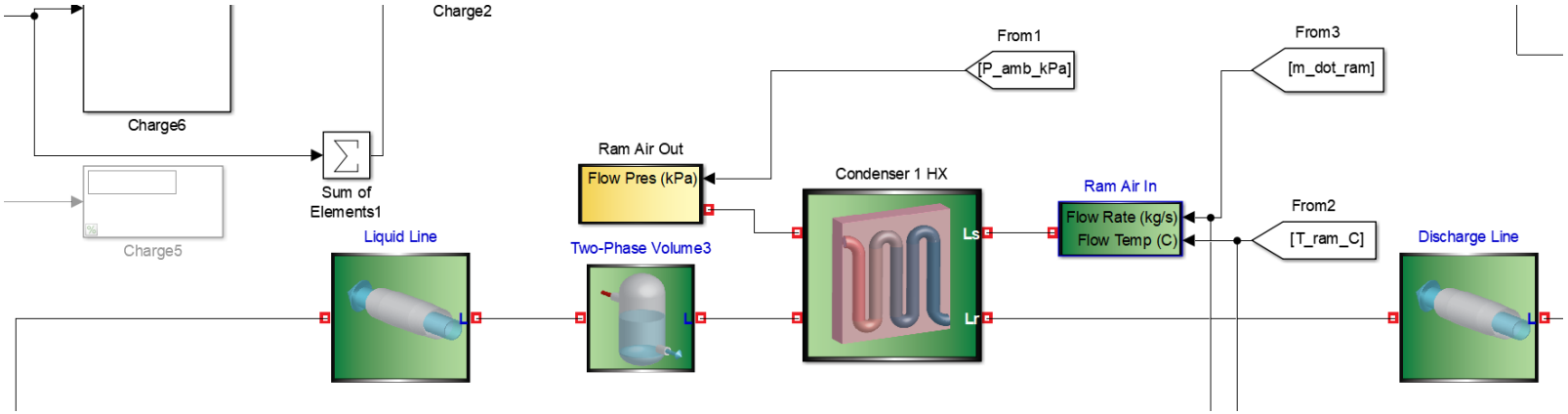

Figure **Error! No text of specified style in document.**.3. Tactical Aircraft Model System Model Diagram, Condenser

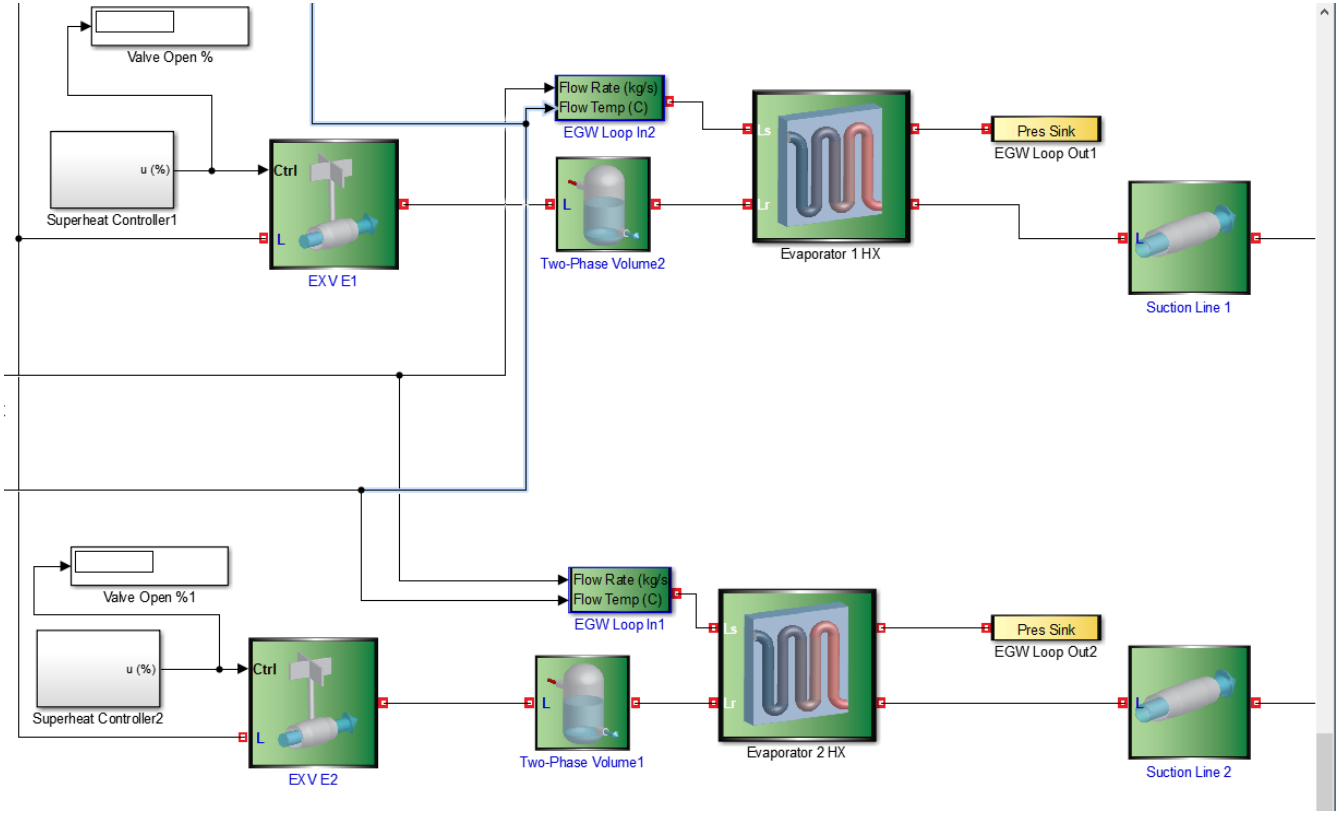

Figure **Error! No text of specified style in document.**.4. Tactical Aircraft Model System Model Diagram, Expansion Valves and Evaporators

A.2 Component Details

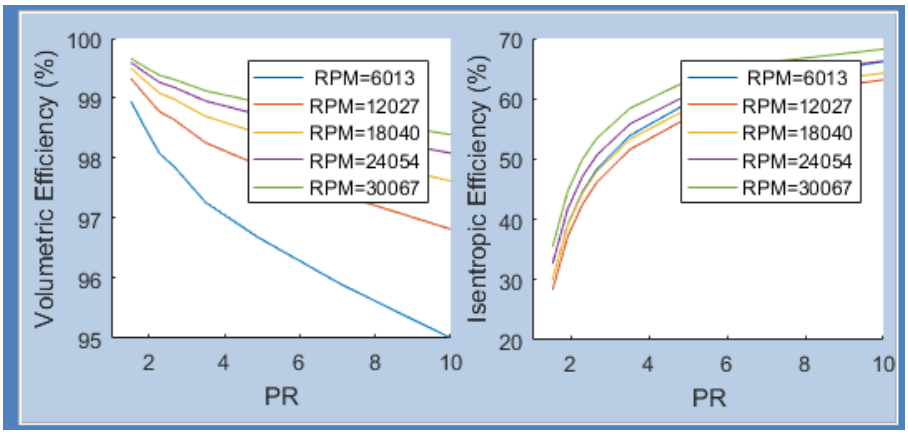

Figure **Error! No text of specified style in document.**.5. Verification and Validation Model Compressor Maps

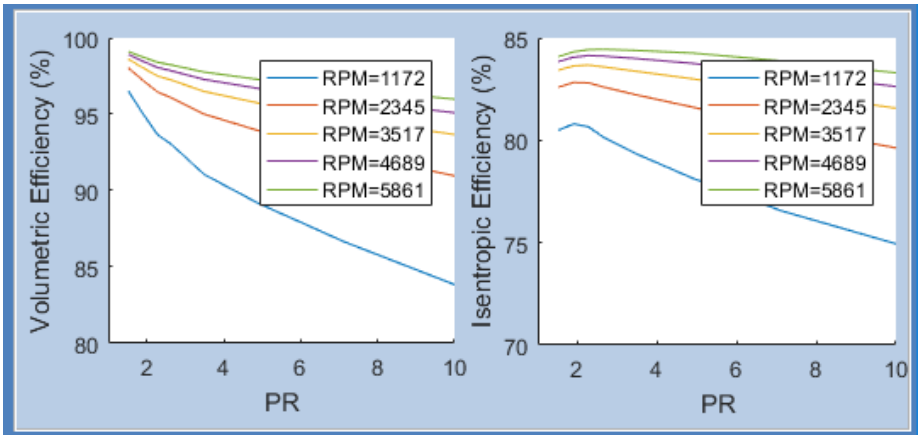

Figure **Error! No text of specified style in document.**.6. Tactical Aircraft Model Compressor, Stage 1 Maps

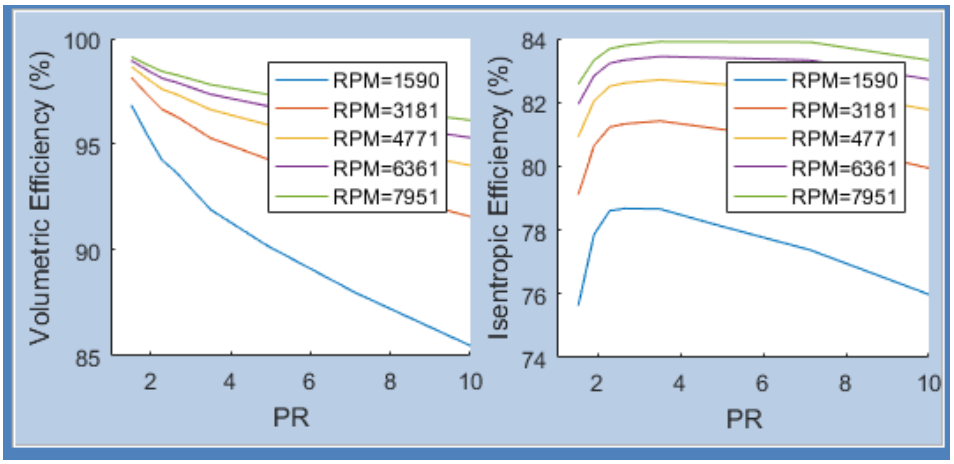

Figure **Error! No text of specified style in document.**.7. Tactical Aircraft Model Compressor, Stage 2 Maps

Table **Error! No text of specified style in document.**.1. Turbomachinery Details

Turbomachinery	**Volumetric Displacement (cm^3)**	**Number of Male Rotors (-)**	**Male Rotor Diameter (mm)**	**Dry Mass (kg)**
Verification Compressor	14.4	4	54.0	11.3
Tactical Aircraft Compressor, Stage 1	288.8	5	146.6	216.7
Tactical Aircraft Compressor, Stage 2	115.7	5	108.1	93.7

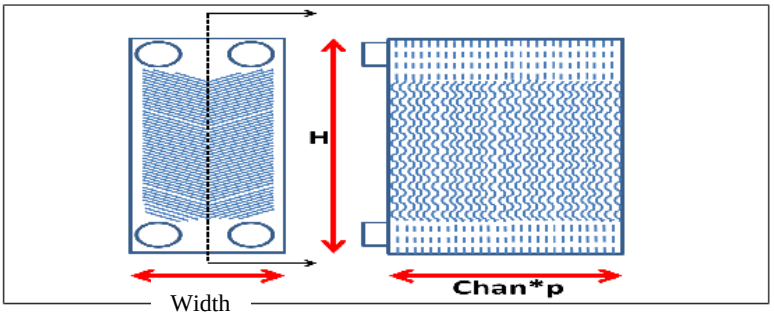

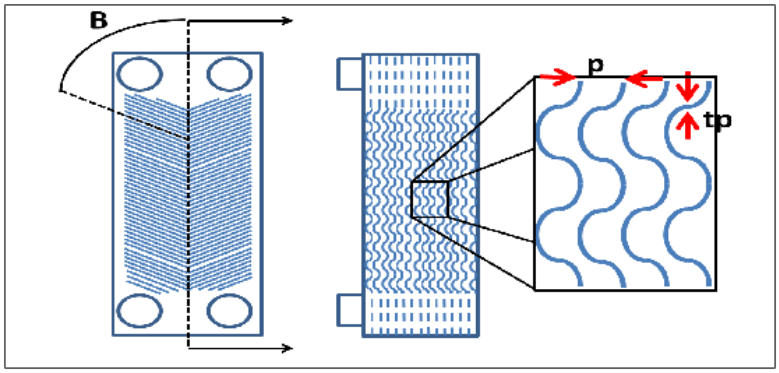

Figure **Error! No text of specified style in document.**.8. Verification and Validation Model Condenser Diagram

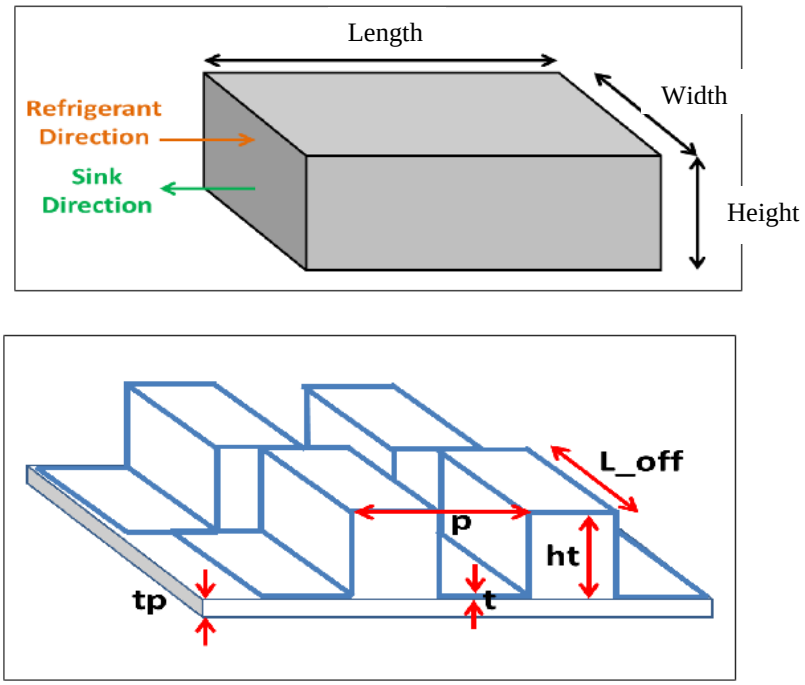

Figure **Error! No text of specified style in document.**.9. Verification and Validation Model Evaporator Diagram

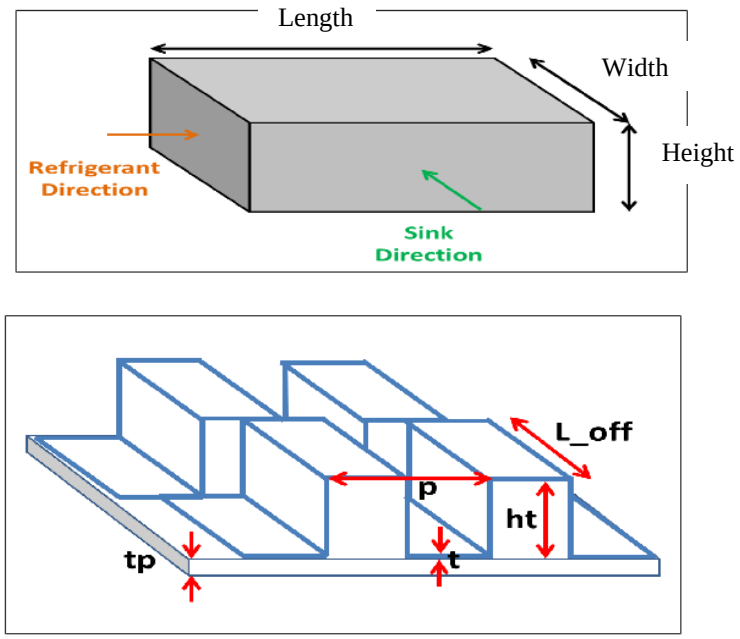

Figure **Error! No text of specified style in document.**.10. Tactical Aircraft Model Condenser Diagram

Tactical Aircraft Evaporators were identical to the Verification and Validation Model Evaporators

Table **Error! No text of specified style in document.**.2. Heat Exchanger Details

Verification Heat Exchangers	**Height (m)**	**Width (m)**	**Length (m)**	**Dry Mass (kg)**
Condenser	0.5150	0.0980	0.1728	2.9456
Evaporator 1	0.0508	0.1588	0.2032	1.5739
Evaporator 2	0.0508	0.1588	0.2032	1.5739
Tactical Aircraft Heat Exchangers	**Height (m)**	**Width (m)**	**Length (m)**	**Dry Mass (kg)**
Condenser	1.2000	0.0833	0.8340	44.2816
Evaporator 1	0.3270	0.2920	0.0523	5.7174
Evaporator 2	0.3270	0.2920	0.0523	5.7174

Table **Error! No text of specified style in document.**.3. Heat Exchanger Fin Details

Verification Condenser	**Liquid Side**	**Air Side**
Fin Structure	Corrugated Plate	Corrugated Plate
β (rad)	4*π/9	4*π/9
p (mm)	2.4	2.4
Chan (-)	36	36
tp (mm)	0.3	0.3
Tactical Aircraft Condenser	**Refrigerant Side**	**Air Side**
Fin Structure	Rectangular Offset	Rectangular Offset
p (mm)	2.54	2.622
ht (mm)	2.387	1.803
t (mm)	0.102	0.102
L_off (mm)	3.175	2.54
tp (mm)	0.204	0.204
Pass (-)	2	1
Verification Evaporator 1 & 2	**Liquid Side**	**Air Side**
Fin Structure	Rectangular Offset	Rectangular Offset
p (mm)	1.016	1.016
ht (mm)	2.032	2.032
t (mm)	0.1	0.1
L_off (mm)	3.81	3.81
tp (mm)	0.7	0.7
Pass (-)	1	1
Tactical Aircraft Evaporator 1 & 2	**Liquid Side**	**Air Side**
Fin Structure	Rectangular Offset	Rectangular Offset
p (mm)	1.016	1.016
ht (mm)	2.032	2.032
t (mm)	0.1	0.1
L_off (mm)	3.81	3.81
tp (mm)	0.7	0.7
Pass (-)	1	1

Table **Error! No text of specified style in document.**.4. Tactical Aircraft Line Details

Line Location	Inner Diameter (mm)	Outer Diameter (mm)	Length (m)	Volume (m)	Mass (kg)
Discharge Line	25.4	28.575	0.1	1.3459E-05	0.1084
Liquid Line	25.4	28.575	1.0	1.3459E-04	1.084
Suction Line	38.1	41.275	1.0	1.9793E-04	1.594

(Assume pipes are made of Stainless Steel AISI 302 with a density of 8055 kg/m^3

Table **Error! No text of specified style in document.**.5. Tactical Aircraft Vapor Compression Cycle Cooling System Mass Breakdown

Component	Mass (kg)
Compressor Stage 1	216.7
Compressor Stage 2	93.7
Condenser	44.3
Expansion Valve 1	5.0
Expansion Valve 2	5.0
Evaporator 1	5.7
Evaporator 2	5.7
Line Totals	2.8
Charge	20.0
System Total	399.0

A.3 Verification and Validation Model Detailed Results

Temperature entropy diagrams for runs one through three are presented in Figure Error! **No text of specified style in document.**.11 through Figure Error! **No text of specified style in document.**.13 and Pressure-enthalpy diagrams for runs one through three are presented in Figure Error! **No text of specified style in document.**.14 through Figure Error! **No text of specified style in document.**.16.

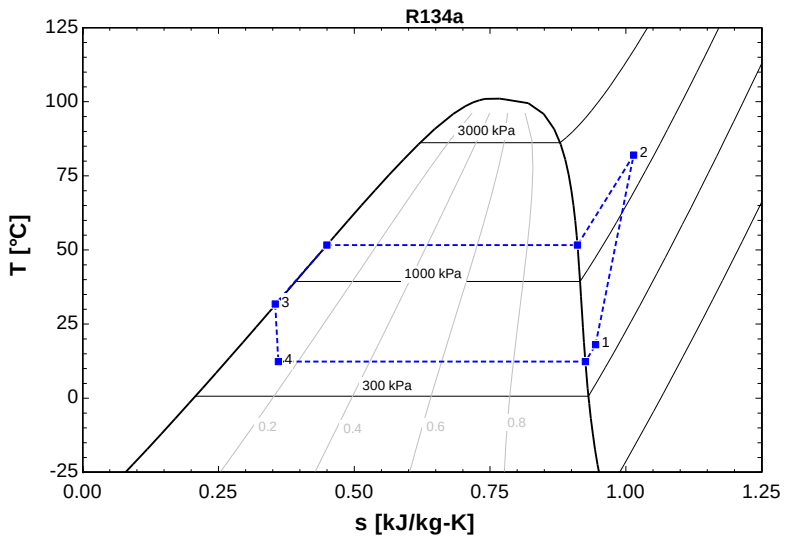

Figure **Error! No text of specified style in document.**.11. Temperature-Entropy Diagram for Model Verification Run 1

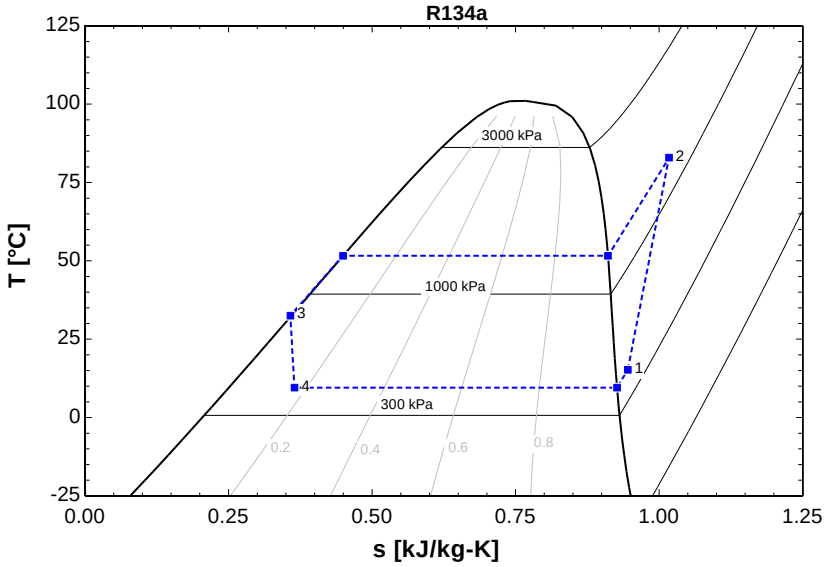

Figure **Error! No text of specified style in document.**.12. Temperature-Entropy Diagram for Model Verification Run 2

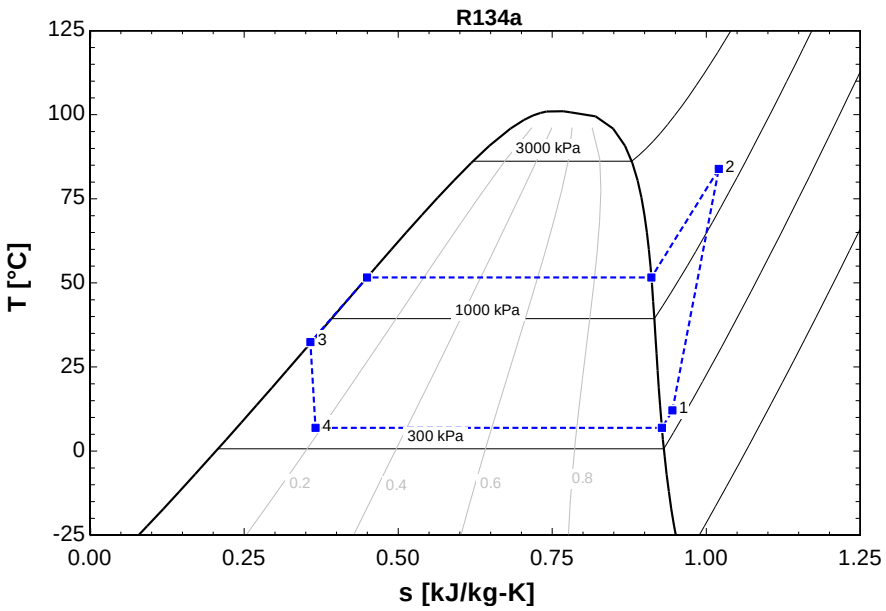

Figure **Error! No text of specified style in document.**.13. Temperature-Entropy Diagram for Model Verification Run 3

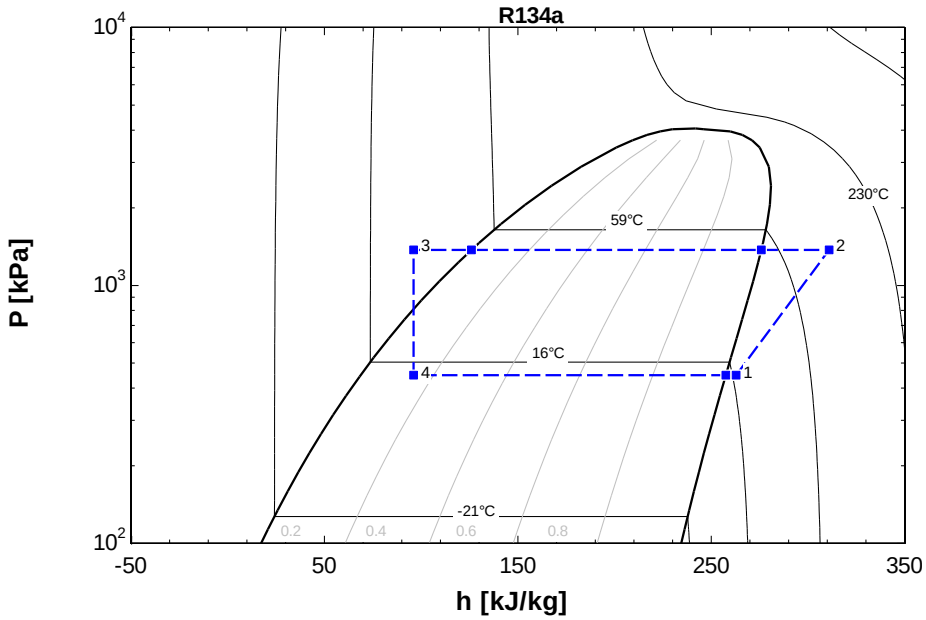

Figure **Error! No text of specified style in document.**.14. Pressure-Enthalpy Diagram for Model Verification Run 1

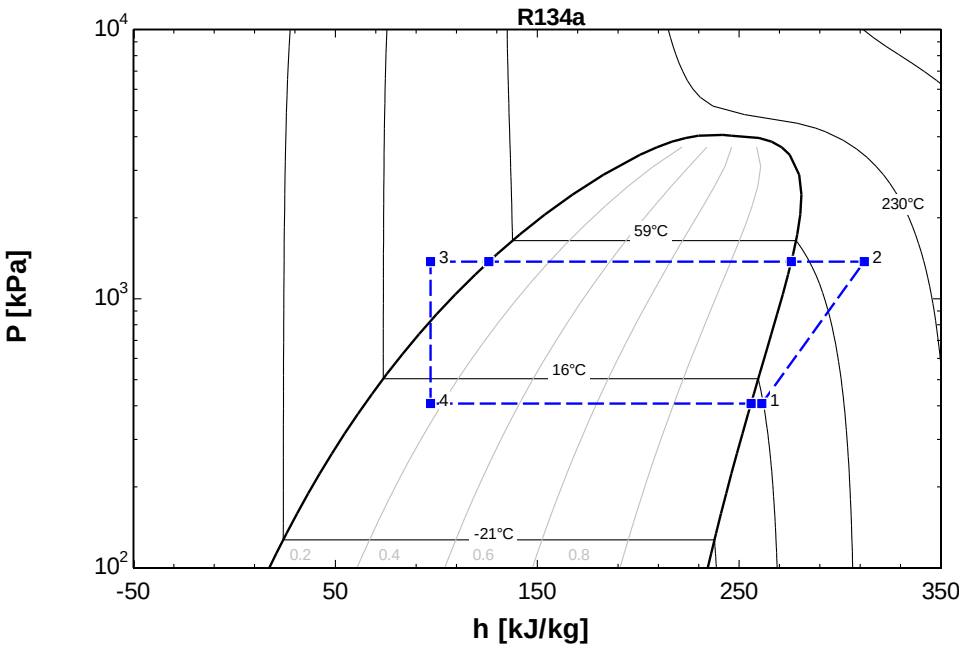

Figure **Error! No text of specified style in document.**.15. Pressure-Enthalpy Diagram for Model Verification Run 2

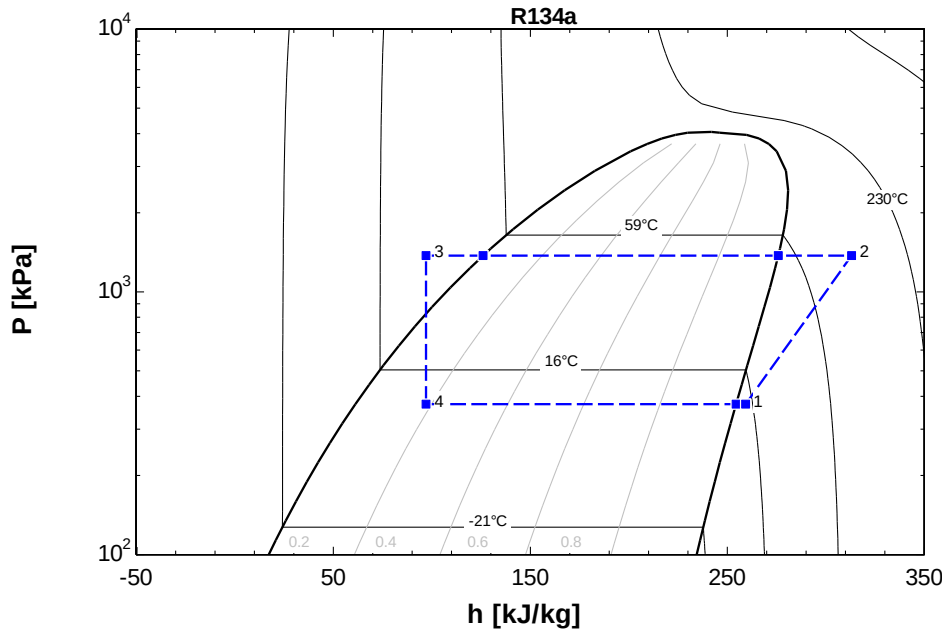

Figure **Error! No text of specified style in document.**.16. Pressure-Enthalpy Diagram for Model Verification Run 3

Table **Error! No text of specified style in document.**.6. Detailed Test Data and Model Results Comparison for All Model Runs

Parameter	Run 1 Relative Error (%)	Run 2 Relative Error (%)	Run 3 Relative Error (%)
$\dot{W}_{comp}$	-9.05	1.94	1.30
$T_{sat,cond}$	0.0305	0.0423	-0.000677
$T_{SC,cond}$	0.131	0.0510	-0.198
$\dot{Q}_{cond}$	-5.57	-3.26	-3.70
$\dot{Q}_{evap\ 4}$	-1.59	-1.59	-2.09
$T_{sat,evap\ 4}$	-0.00767	0.0677	0.133
$T_{SH,evap\ 4}$	0.180	-0.13	-0.459
$T_{sink,out,evap\ 4}$	-0.0228	0.0193	0.0577
$\dot{m}_{r,evap\ 4}$	-0.800	-0.526	-2.34
$\dot{Q}_{evap\ 5}$	-2.88	-2.36	-2.09
$T_{sat,evap\ 5}$	0.0414	0.0536	0.132
$T_{SH,evap\ 5}$	0.0521	-0.276	-0.494
$T_{sink,out,evap\ 5}$	0.252	0.0540	0.0927
$\dot{m}_{r,evap\ 5}$	-9.05	-3.08	-3.59
ΔP_{suc}	-17.4	n/a	n/a
ΔP_{ds}	-8.81	n/a	n/a
ΔP_{liq}	-7.30	n/a	n/a

A.4 Tactical Aircraft Model Detailed Results

Table **Error! No text of specified style in document.**.7. Vapor Compression Cycle System Model Convergence

Mission 1			Mission 2		
Segment	**Mass Balance (kg/s)**	**Energy Balance (W)**	**Segment**	**Mass Balance (kg/s)**	**Energy Balance (W)**
1	2.22E-16	-5.68E-10	1	2.22E-16	-5.68E-10
2	-3.68E-06	2.43E-02	2	7.43E-07	-2.86E-02
3	2.44E-15	2.20E-07	3	-5.55E-16	5.68E-11
4	-3.68E-06	2.43E-02	4	-6.31E-11	1.42E-04
5	-4.44E-16	5.68E-11	5	7.43E-07	-2.86E-02
			6	2.27E-07	-7.64E-02

Table **Error! No text of specified style in document.**.8. Vapor Compression Cycle Tactical Aircraft Mission Results

Mission One Segment One, Ground Idle						
State	**Description**	**P (kPa)**	**T (ºC)**	**h (kJ/kg)**	**s (kJ/kg-K)**	$\dot{m}$ **(kg/s)**
0	Ambient	101.3	41.00	438.3	1.946	0
1	Compressor Stage 1 Inlet	342.3	12.39	408.4	1.751	0.6468
2	Compressor Stage 2 Inlet	903.3	51.35	434.2	1.765	0.6468
3	Compressor Stage 2 Outlet	2032	89.49	457.2	1.779	0.6468
4	Condenser Inlet	2030	89.47	457.2	1.779	0.5596
5	Condenser Outlet	2030	58.30	284.6	1.275	0.5596
6a	Expansion Valve 1 Inlet	2028	58.30	284.6	1.275	0.2798
7a	Expansion Valve 1 Outlet	345.2	4.629	284.6	1.305	0.2798
8a	Evaporator 1 Inlet	344.9	4.606	284.6	1.305	0.2798
9a	Evaporator 1 Outlet	344.8	4.593	400.8	1.723	0.2798
6b	Expansion Valve 2 Inlet	2028	58.30	284.6	1.275	0.2798
7b	Expansion Valve 2 Outlet	345.5	4.653	284.6	1.305	0.2798
8b	Evaporator 2 Inlet	345.2	4.630	284.6	1.305	0.2798
9b	Evaporator 2 Outlet	345.1	4.617	400.8	1.723	0.2798
Mission One Segment Two, Cruise Out						
State	**Description**	**P (kPa)**	**T (ºC)**	**h (kJ/kg)**	**s (kJ/kg-K)**	$\dot{m}$ **(kg/s)**
0	Ambient	23.84	-23.77	387.1	1.880	0
1	Compressor Stage 1 Inlet	355.9	13.51	409.1	1.750	0.6722
2	Compressor Stage 2 Inlet	914.6	51.52	434.2	1.764	0.6722
3	Compressor Stage 2 Outlet	1083	59.26	439.2	1.768	0.6722
4	Condenser Inlet	1080	59.20	439.2	1.768	0.6441
5	Condenser Outlet	1079	29.10	240.5	1.138	0.6441
6a	Expansion Valve 1 Inlet	1077	29.10	240.5	1.138	0.3221
7a	Expansion Valve 1 Outlet	359.2	5.776	240.5	1.145	0.3221
8a	Evaporator 1 Inlet	358.9	5.750	240.5	1.145	0.3221
9a	Evaporator 1 Outlet	358.8	12.16	407.8	1.745	0.3221
6b	Expansion Valve 2 Inlet	1077	29.10	240.5	1.138	0.3220
7b	Expansion Valve 2 Outlet	359.6	5.802	240.5	1.145	0.3220
8b	Evaporator 2 Inlet	359.2	5.776	240.5	1.145	0.3220
9b	Evaporator 2 Outlet	359.1	12.14	407.8	1.745	0.3220

Table **Error! No text of specified style in document.**.8. Vapor Compression Cycle Tactical Aircraft Mission Results Continued

Mission One Segment Three, Combat						
State	**Description**	**P (kPa)**	**T (ºC)**	**h (kJ/kg)**	**s (kJ/kg-K)**	$\dot{m}$ **(kg/s)**
0	Ambient	46.56	-0.5601	404.6	1.893	0
1	Compressor Stage 1 Inlet	333.4	11.63	407.9	1.751	1.507
2	Compressor Stage 2 Inlet	887.4	50.10	433.2	1.764	1.507
3	Compressor Stage 2 Outlet	2674	102.5	462.9	1.778	1.507
4	Condenser Inlet	2667	102.4	462.9	1.778	1.467
5	Condenser Outlet	2667	70.29	304.3	1.332	1.467
6a	Expansion Valve 1 Inlet	2659	70.28	304.3	1.332	0.7336
7a	Expansion Valve 1 Outlet	347.8	4.847	304.3	1.375	0.7336
8a	Evaporator 1 Inlet	347.1	4.786	304.3	1.375	0.7336
9a	Evaporator 1 Outlet	346.6	10.41	406.5	1.743	0.7336
6b	Expansion Valve 2 Inlet	2659	70.28	304.3	1.332	0.7335
7b	Expansion Valve 2 Outlet	348.5	4.904	304.3	1.375	0.7335
8b	Evaporator 2 Inlet	347.8	4.843	304.3	1.375	0.7335
9b	Evaporator 2 Outlet	347.3	10.36	406.4	1.743	0.7335
Mission One Segment Four, Cruise In						
State	**Description**	**P (kPa)**	**T (ºC)**	**h (kJ/kg)**	**s (kJ/kg-K)**	$\dot{m}$ **(kg/s)**
0	Ambient	23.84	-23.77	387.1	1.880	0
1	Compressor Stage 1 Inlet	355.9	13.51	409.1	1.750	0.6722
2	Compressor Stage 2 Inlet	914.6	51.52	434.2	1.764	0.6722
3	Compressor Stage 2 Outlet	1083	59.26	439.2	1.768	0.6722
4	Condenser Inlet	1080	59.20	439.2	1.768	0.6441
5	Condenser Outlet	1079	29.10	240.5	1.138	0.6441
6a	Expansion Valve 1 Inlet	1077	29.10	240.5	1.138	0.3221
7a	Expansion Valve 1 Outlet	359.2	5.776	240.5	1.145	0.3221
8a	Evaporator 1 Inlet	358.9	5.750	240.5	1.145	0.3221
9a	Evaporator 1 Outlet	358.8	12.16	407.8	1.745	0.3221
6b	Expansion Valve 2 Inlet	1077	29.10	240.5	1.138	0.3220
7b	Expansion Valve 2 Outlet	359.6	5.802	240.5	1.145	0.3220
8b	Evaporator 2 Inlet	359.2	5.776	240.5	1.145	0.3220

Table Error! No text of specified style in document..8. Vapor Compression Cycle Tactical Aircraft Mission Results Continued

Mission One Segment Five, Loiter						
State	**Description**	**P (kPa)**	**T (°C)**	**h (kJ/kg)**	**s (kJ/kg-K)**	$\dot{m}$ **(kg/s)**
0	Ambient	37.60	-8.960	398.1	1.886	0
1	Compressor Stage 1 Inlet	296.5	8.341	405.9	1.753	0.5635
2	Compressor Stage 2 Inlet	769.0	45.89	431.2	1.767	0.5635
3	Compressor Stage 2 Outlet	821.8	48.84	433.2	1.769	0.5635
4	Condenser Inlet	818.8	48.78	433.2	1.769	0.5420
5	Condenser Outlet	818.3	19.43	226.7	1.093	0.5420
6a	Expansion Valve 1 Inlet	816.6	19.44	226.7	1.093	0.2711
7a	Expansion Valve 1 Outlet	299.3	0.6072	226.7	1.098	0.2711
8a	Evaporator 1 Inlet	299.1	0.5819	226.7	1.098	0.2711
9a	Evaporator 1 Outlet	298.9	7.215	404.9	1.748	0.2711
6b	Expansion Valve 2 Inlet	816.6	19.44	226.7	1.093	0.2710
7b	Expansion Valve 2 Outlet	299.6	0.6322	226.7	1.098	0.2710
8b	Evaporator 2 Inlet	299.3	0.6069	226.7	1.098	0.2710
9b	Evaporator 2 Outlet	299.2	7.196	404.8	1.748	0.2710

Table Error! No text of specified style in document..8. Vapor Compression Cycle Tactical Aircraft Mission Results Continued

Mission Two Segment One, Ground Idle						
State	**Description**	**P (kPa)**	**T (ºC)**	**h (kJ/kg)**	**s (kJ/kg-K)**	$\dot{m}$ **(kg/s)**
0	Ambient	101.3	41.00	438.3	1.946	0
1	Compressor Stage 1 Inlet	342.3	12.39	408.4	1.751	0.6468
2	Compressor Stage 2 Inlet	903.3	51.35	434.2	1.765	0.6468
3	Compressor Stage 2 Outlet	2032	89.49	457.2	1.779	0.6468
4	Condenser Inlet	2030	89.47	457.2	1.779	0.5596
5	Condenser Outlet	2030	58.30	284.6	1.275	0.5596
6a	Expansion Valve 1 Inlet	2028	58.30	284.6	1.275	0.2798
7a	Expansion Valve 1 Outlet	345.2	4.629	284.6	1.305	0.2798
8a	Evaporator 1 Inlet	344.9	4.606	284.6	1.305	0.2798
9a	Evaporator 1 Outlet	344.8	4.593	400.8	1.723	0.2798
6b	Expansion Valve 2 Inlet	2028	58.30	284.6	1.275	0.2798
7b	Expansion Valve 2 Outlet	345.5	4.653	284.6	1.305	0.2798
8b	Evaporator 2 Inlet	345.2	4.630	284.6	1.305	0.2798
9b	Evaporator 2 Outlet	345.1	4.617	400.8	1.723	0.2798
Mission Two Segment Two, Cruise Out						
State	**Description**	**P (kPa)**	**T (ºC)**	**h (kJ/kg)**	**s (kJ/kg-K)**	$\dot{m}$ **(kg/s)**
0	Ambient	30.09	-16.21	392.7	1.883	0
1	Compressor Stage 1 Inlet	368.4	14.51	409.7	1.750	0.6951
2	Compressor Stage 2 Inlet	944.9	52.61	434.7	1.764	0.6951
3	Compressor Stage 2 Outlet	1215	64.24	442.2	1.769	0.6951
4	Condenser Inlet	1212	64.18	442.2	1.769	0.6613
5	Condenser Outlet	1211	34.55	248.3	1.164	0.6613
6a	Expansion Valve 1 Inlet	1209	34.55	248.3	1.164	0.3307
7a	Expansion Valve 1 Outlet	371.9	6.780	248.3	1.173	0.3307
8a	Evaporator 1 Inlet	371.5	6.754	248.3	1.173	0.3307
9a	Evaporator 1 Outlet	371.4	12.81	408.1	1.743	0.3307
6b	Expansion Valve 2 Inlet	1209	34.55	248.3	1.164	0.3306
7b	Expansion Valve 2 Outlet	372.2	6.805	248.3	1.173	0.3306
8b	Evaporator 2 Inlet	371.9	6.779	248.3	1.173	0.3306
9b	Evaporator 2 Outlet	371.7	12.78	408.0	1.743	0.3306

Table Error! No text of specified style in document..8. Vapor Compression Cycle Tactical Aircraft Mission Results Continued

Mission Two Segment Three, Loiter						
State	**Description**	**P (kPa)**	**T (°C)**	**h (kJ/kg)**	**s (kJ/kg-K)**	$\dot{m}$ **(kg/s)**
0	Ambient	37.60	-8.960	398.1	1.886	0
1	Compressor Stage 1 Inlet	357.4	13.63	409.2	1.750	0.7539
2	Compressor Stage 2 Inlet	920.9	51.65	434.2	1.764	0.7539
3	Compressor Stage 2 Outlet	1050	57.66	438.1	1.767	0.7539
4	Condenser Inlet	1046	57.58	438.1	1.767	0.7325
5	Condenser Outlet	1046	27.17	237.7	1.129	0.7325
6a	Expansion Valve 1 Inlet	1043	27.17	237.7	1.129	0.3663
7a	Expansion Valve 1 Outlet	361.5	5.958	237.7	1.135	0.3663
8a	Evaporator 1 Inlet	361.1	5.929	237.7	1.135	0.3663
9a	Evaporator 1 Outlet	360.9	12.82	408.3	1.746	0.3663
6b	Expansion Valve 2 Inlet	1043	27.17	237.7	1.129	0.3662
7b	Expansion Valve 2 Outlet	361.9	5.987	237.7	1.135	0.3662
8b	Evaporator 2 Inlet	361.5	5.958	237.7	1.135	0.3662
9b	Evaporator 2 Outlet	361.3	12.79	408.3	1.746	0.3662
Mission Two Segment Four, Dash						
State	**Description**	**P (kPa)**	**T (°C)**	**h (kJ/kg)**	**s (kJ/kg-K)**	$\dot{m}$ **(kg/s)**
0	Ambient	100.1	40.30	437.7	1.945	0
1	Compressor Stage 1 Inlet	343.3	12.47	408.5	1.751	2.239
2	Compressor Stage 2 Inlet	914.6	50.96	433.6	1.763	2.239
3	Compressor Stage 2 Outlet	3730	120.2	470.3	1.778	2.239
4	Condenser Inlet	3719	120.1	470.3	1.779	2.239
5	Condenser Outlet	3718	90.25	342.4	1.436	2.239
6a	Expansion Valve 1 Inlet	3699	90.19	342.4	1.436	1.120
7a	Expansion Valve 1 Outlet	375.8	7.085	342.4	1.508	1.120
8a	Evaporator 1 Inlet	374.6	6.997	342.4	1.509	1.120
9a	Evaporator 1 Outlet	374.0	13.35	408.5	1.744	1.120
6b	Expansion Valve 2 Inlet	3699	90.19	342.4	1.436	1.119
7b	Expansion Valve 2 Outlet	376.7	7.161	342.4	1.508	1.119
8b	Evaporator 2 Inlet	375.6	7.073	342.4	1.508	1.119
9b	Evaporator 2 Outlet	375.0	13.31	408.4	1.744	1.119

Table Error! No text of specified style in document..8. Vapor Compression Cycle Tactical Aircraft Mission Results Continued

Mission Two Segment Five, Cruise In						
State	**Description**	**P (kPa)**	**T (°C)**	**h (kJ/kg)**	**s (kJ/kg-K)**	**$\dot{m}$ (kg/s)**
0	Ambient	30.09	-16.21	392.7	1.883	0
1	Compressor Stage 1 Inlet	368.4	14.51	409.7	1.750	0.6951
2	Compressor Stage 2 Inlet	944.9	52.61	434.7	1.764	0.6951
3	Compressor Stage 2 Outlet	1215	64.24	442.2	1.769	0.6951
4	Condenser Inlet	1212	64.18	442.2	1.769	0.6613
5	Condenser Outlet	1211	34.55	248.3	1.164	0.6613
6a	Expansion Valve 1 Inlet	1209	34.55	248.3	1.164	0.3307
7a	Expansion Valve 1 Outlet	371.9	6.780	248.3	1.173	0.3307
8a	Evaporator 1 Inlet	371.5	6.754	248.3	1.173	0.3307
9a	Evaporator 1 Outlet	371.4	12.81	408.1	1.743	0.3307
6b	Expansion Valve 2 Inlet	1209	34.55	248.3	1.164	0.3306
7b	Expansion Valve 2 Outlet	372.2	6.805	248.3	1.173	0.3306
8b	Evaporator 2 Inlet	371.9	6.779	248.3	1.173	0.3306
9b	Evaporator 2 Outlet	371.7	12.78	408.0	1.743	0.3306
Mission Two Segment Six Loiter						
State	**Description**	**P (kPa)**	**T (°C)**	**h (kJ/kg)**	**s (kJ/kg-K)**	**$\dot{m}$ (kg/s)**
0	Ambient	43.31	-3.448	402.3	1.891	0
1	Compressor Stage 1 Inlet	311.5	9.713	406.8	1.752	0.5909
2	Compressor Stage 2 Inlet	805.9	47.38	432.0	1.767	0.5909
3	Compressor Stage 2 Outlet	981.4	56.24	437.9	1.771	0.5909
4	Condenser Inlet	978.5	56.19	437.9	1.771	0.5622
5	Condenser Outlet	978.1	27.19	237.7	1.130	0.5622
6a	Expansion Valve 1 Inlet	976.3	27.19	237.7	1.130	0.2811
7a	Expansion Valve 1 Outlet	314.4	1.980	237.7	1.137	0.2811
8a	Evaporator 1 Inlet	314.1	1.955	237.7	1.137	0.2811
9a	Evaporator 1 Outlet	314.0	8.035	405.2	1.746	0.2811
6b	Expansion Valve 2 Inlet	976.3	27.19	237.7	1.130	0.2811
7b	Expansion Valve 2 Outlet	314.7	2.005	237.7	1.137	0.2811
8b	Evaporator 2 Inlet	314.4	1.980	237.7	1.137	0.2811
9b	Evaporator 2 Outlet	314.2	8.009	405.2	1.745	0.2811

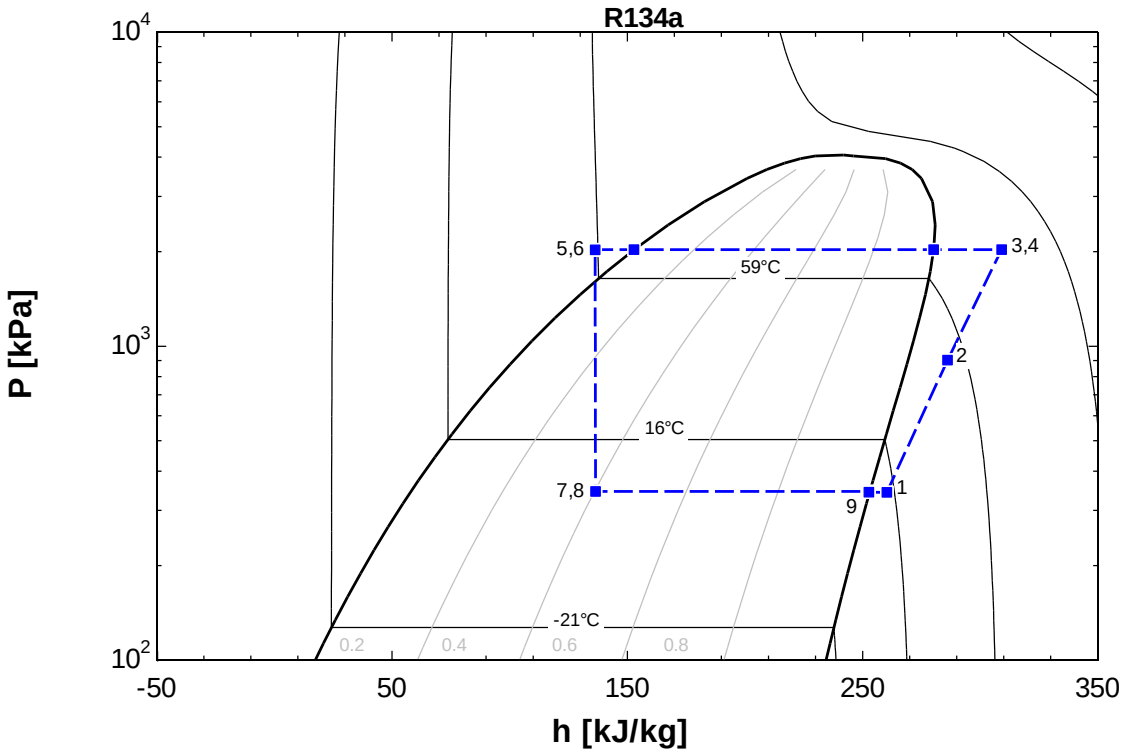

Figure **Error! No text of specified style in document.**.17. Mission One and Two, Segment One, P-h Diagram

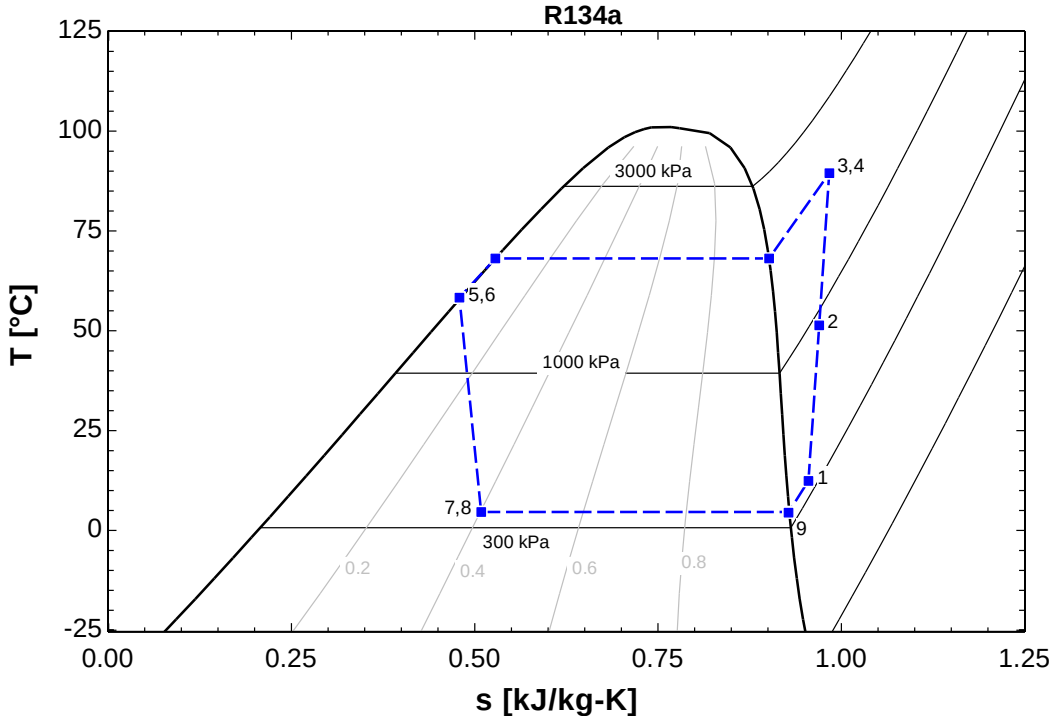

Figure **Error! No text of specified style in document.**.18. Mission One and Two, Segment One, T-s Diagram

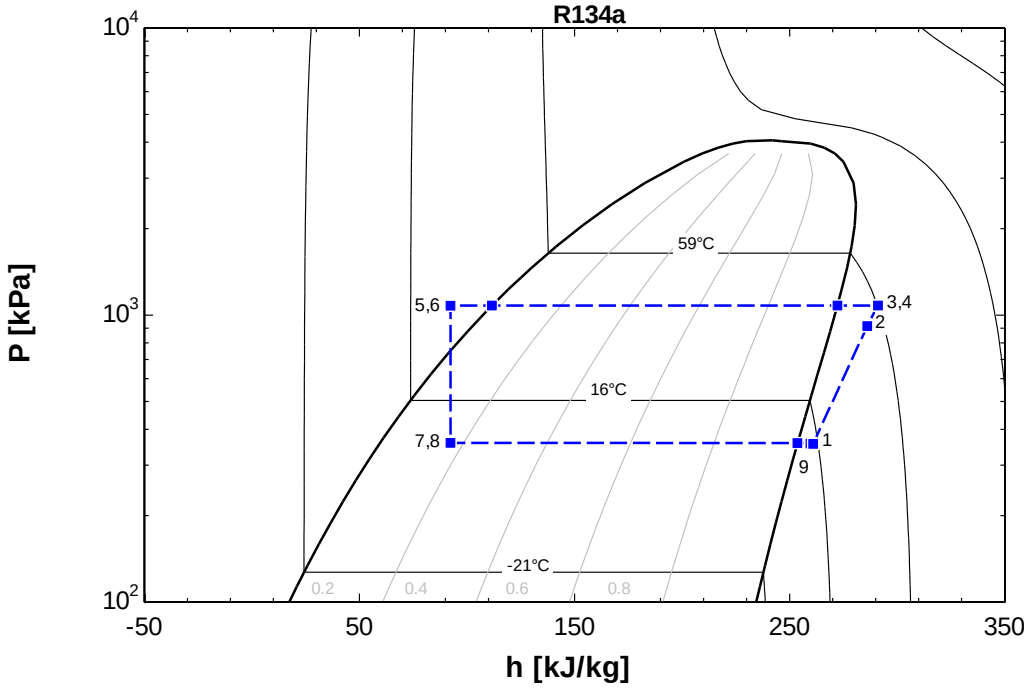

Figure **Error! No text of specified style in document.**.19. Mission One, Segment Two and Segment Four, P-h Diagram

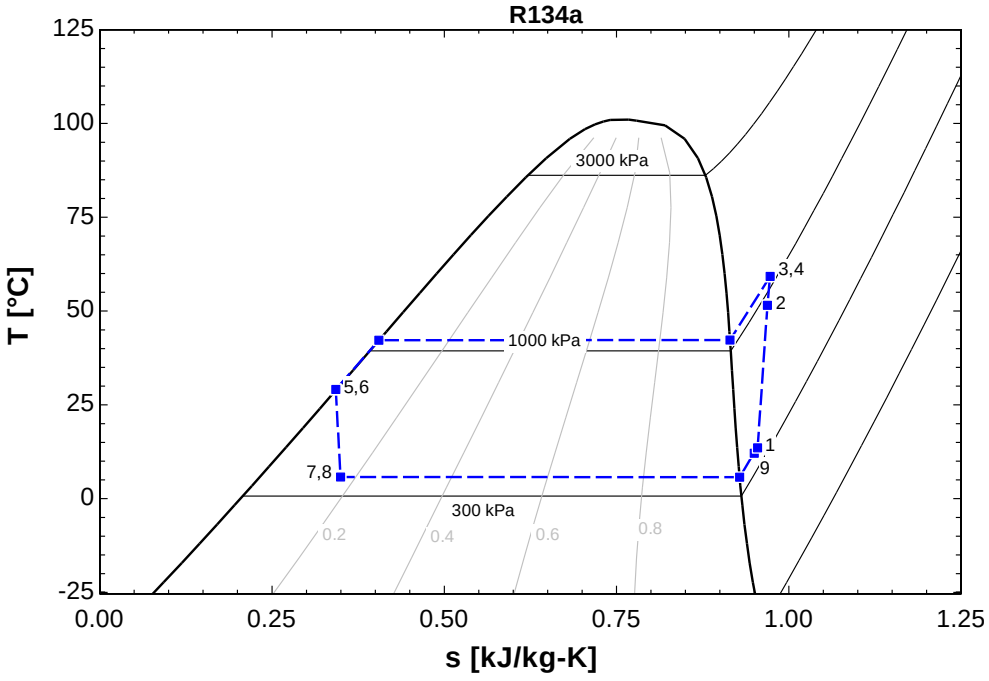

Figure **Error! No text of specified style in document.**.20. Mission One, Segment Two and Segment Four, T-s Diagram

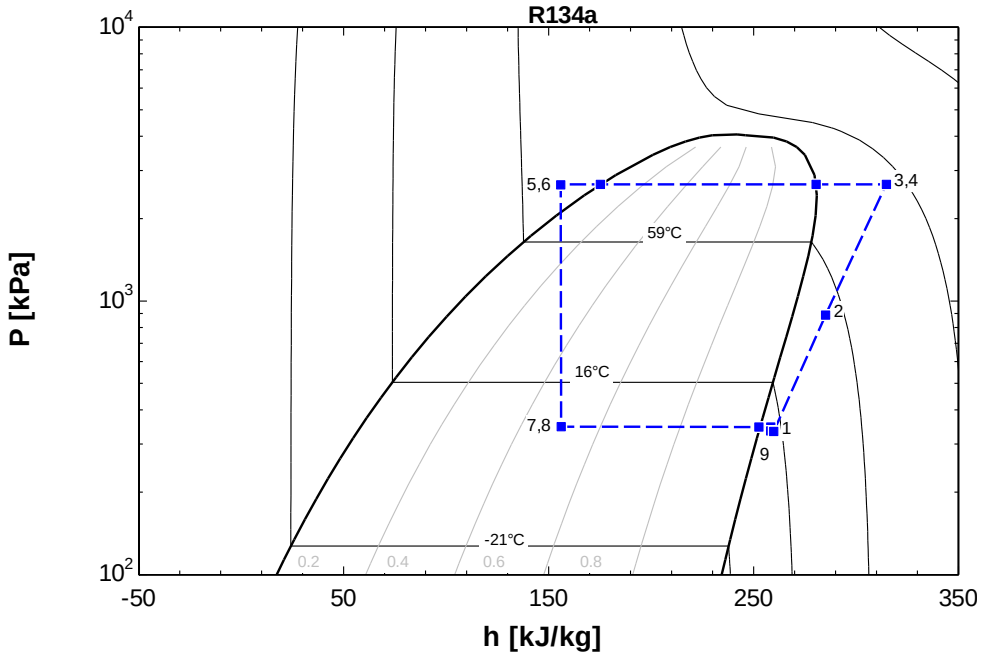

Figure **Error! No text of specified style in document.**.21. Mission One, Segment Three, P-h Diagram

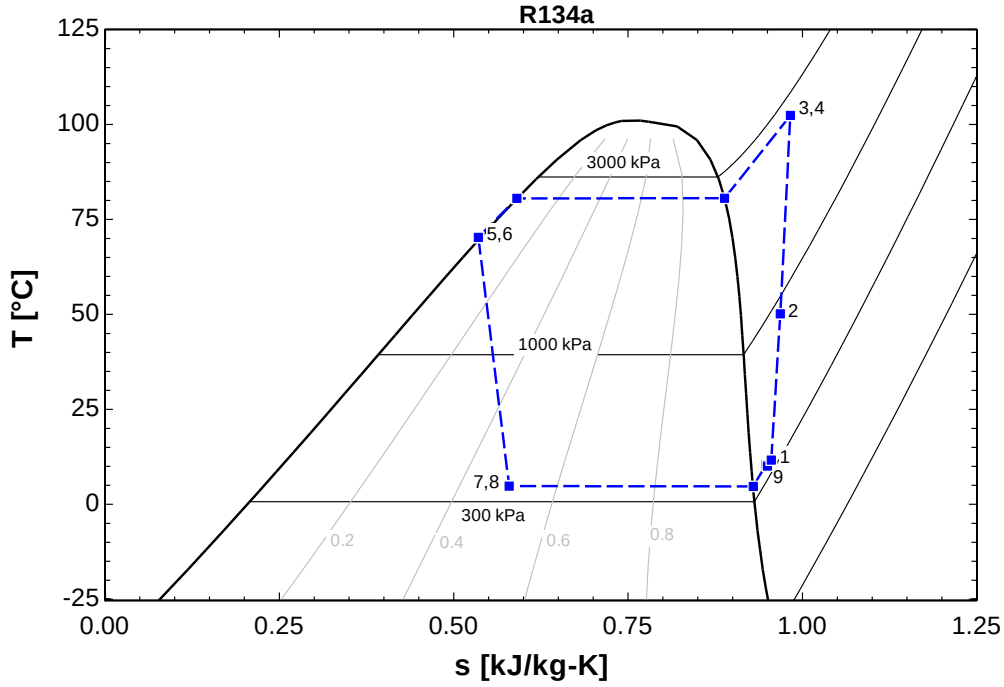

Figure **Error! No text of specified style in document.**.22. Mission One, Segment Three, T-s Diagram

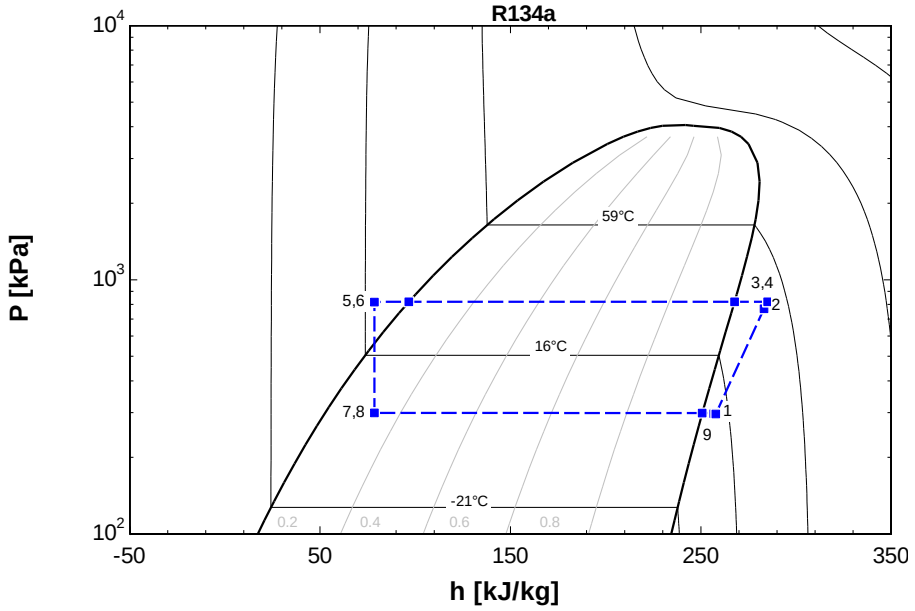

Figure **Error! No text of specified style in document.**.23. Mission One, Segment Five, P-h Diagram

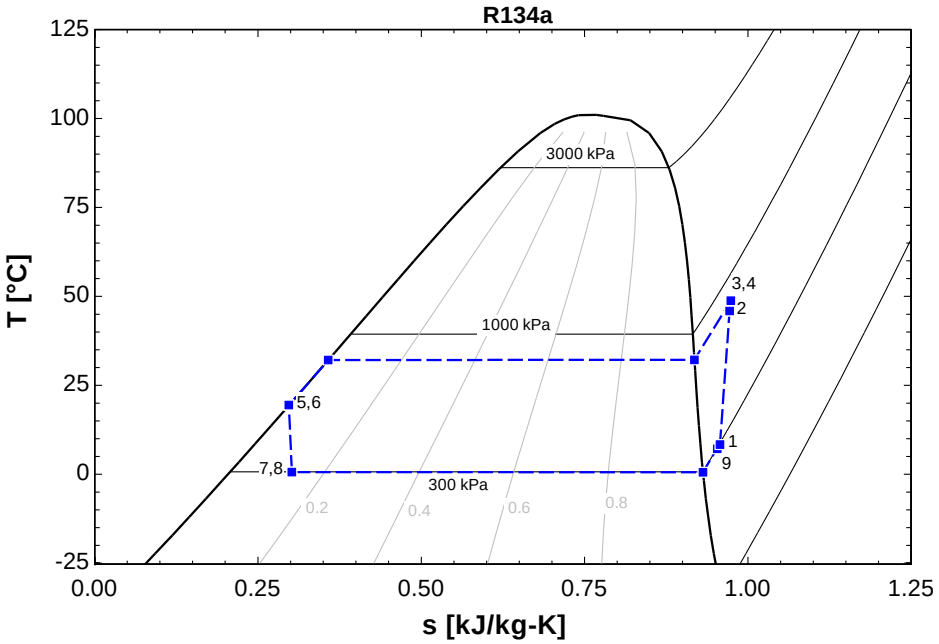

Figure **Error! No text of specified style in document.**.24. Mission One, Segment Five, T-s Diagram

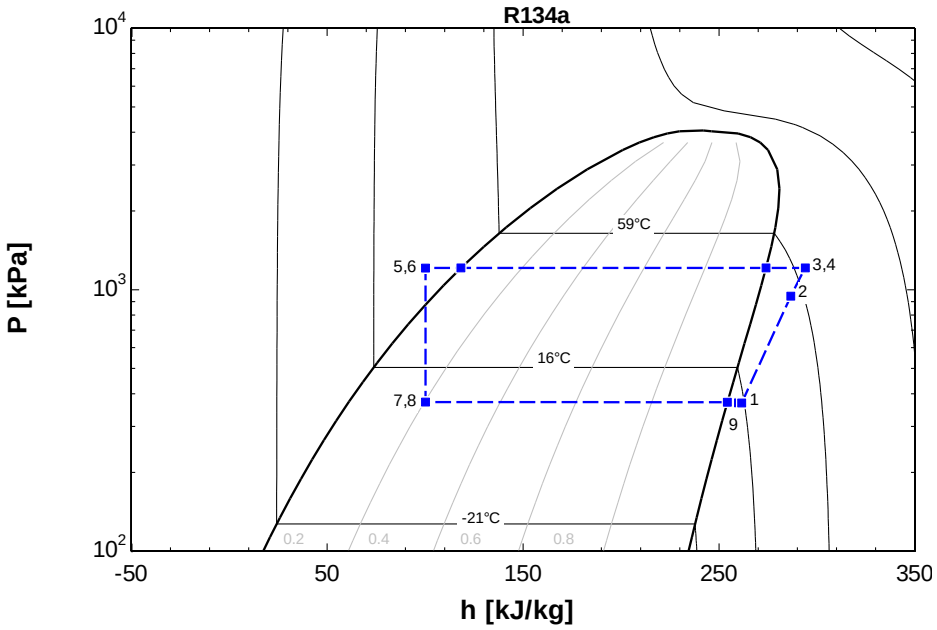

Figure **Error! No text of specified style in document.**.25. Mission Two, Segment Two and Five, P-h Diagram

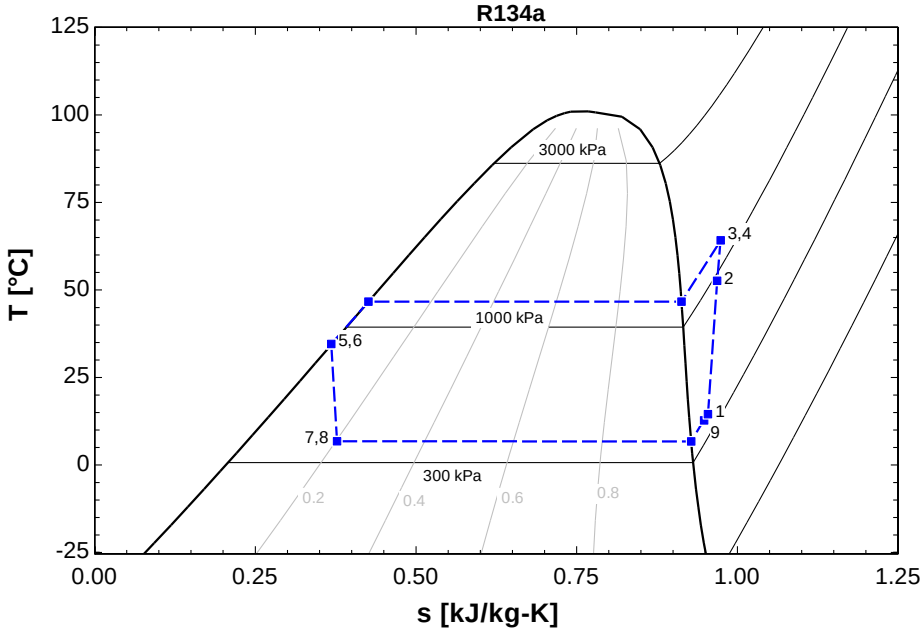

Figure **Error! No text of specified style in document.**.26. Mission Two, Segment Two and Five, T-s Diagram

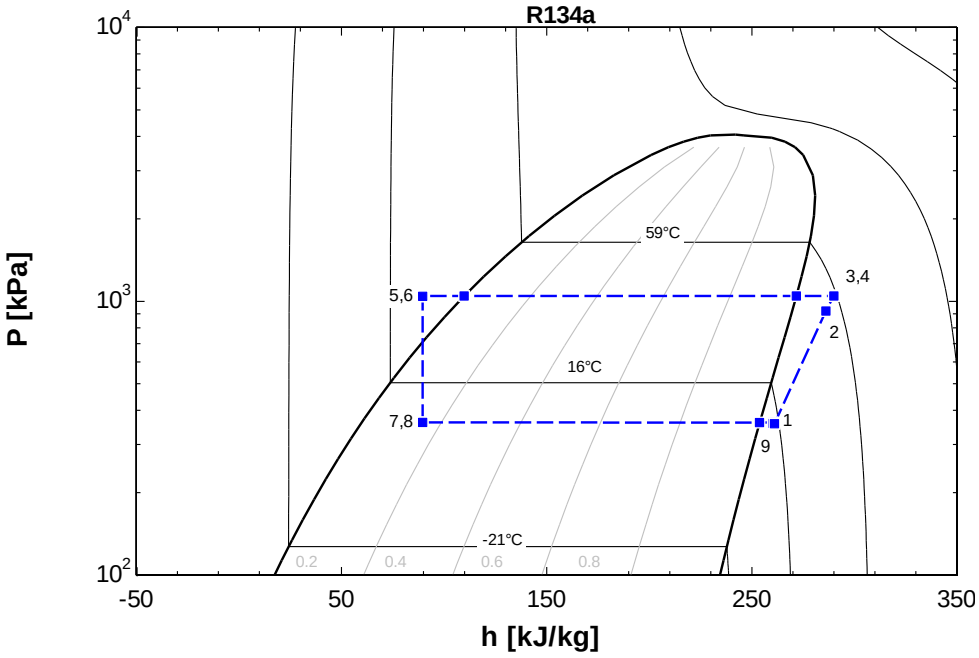

Figure **Error! No text of specified style in document.**.27. Mission Two, Segment Three, P-h Diagram

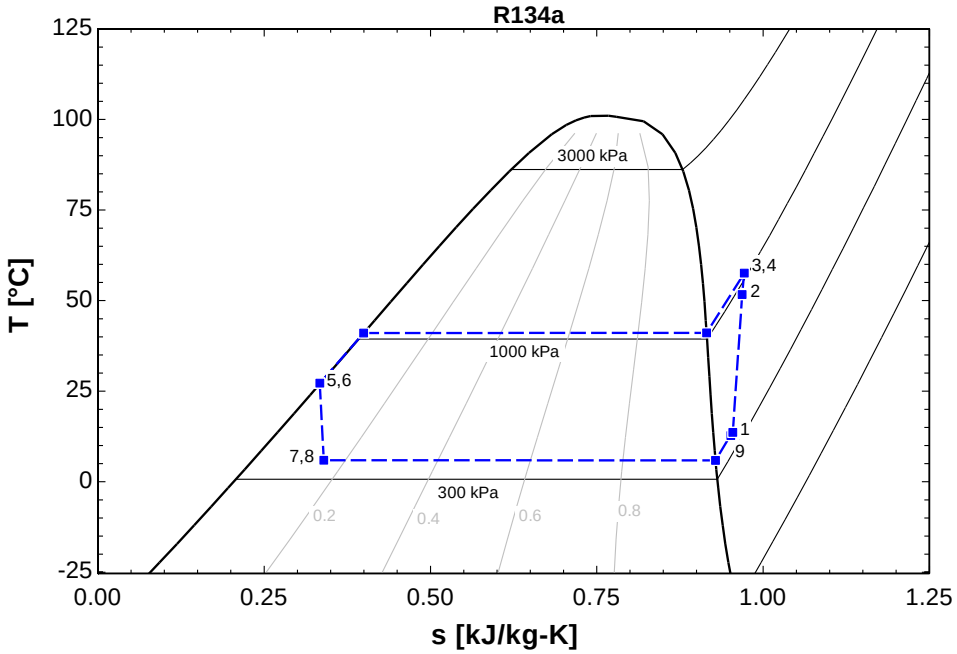

Figure **Error! No text of specified style in document.**.28. Mission Two, Segment Three, T-s Diagram

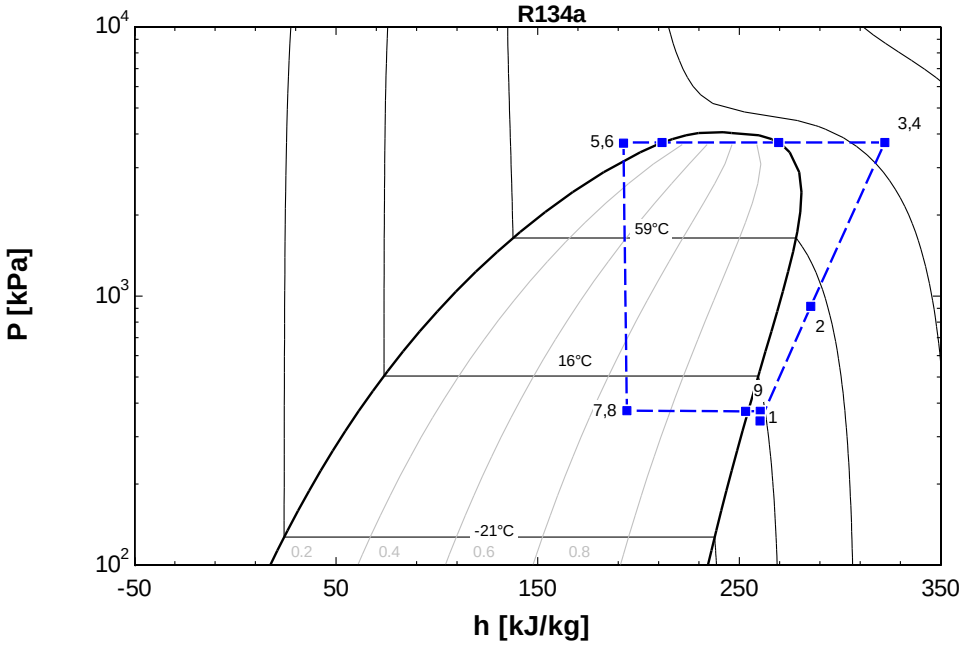

Figure **Error! No text of specified style in document.**.29. Mission Two, Segment Four, P-h Diagram

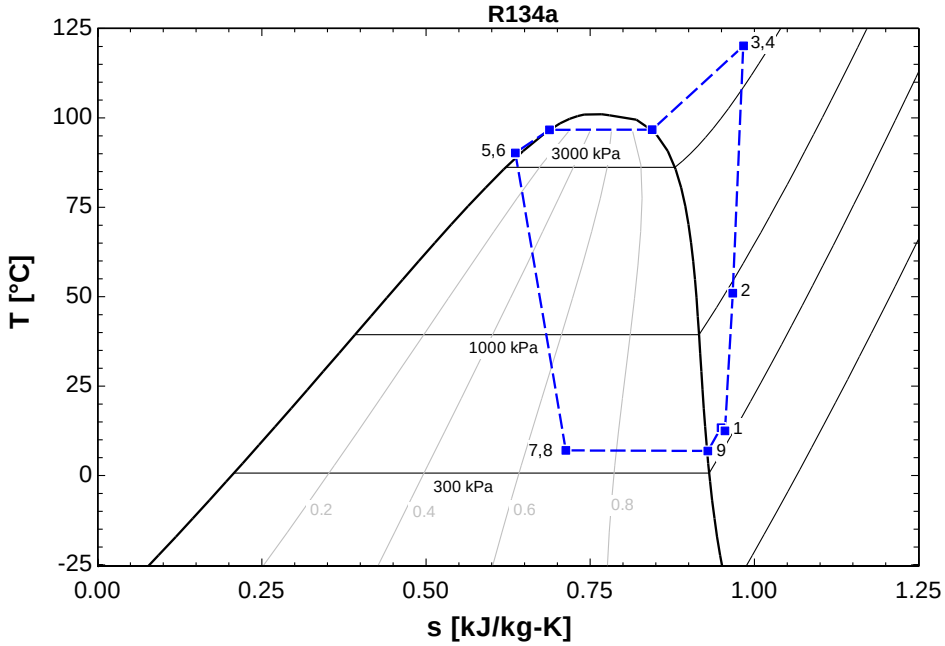

Figure **Error! No text of specified style in document.**.30. Mission Two, Segment Four, T-s Diagram

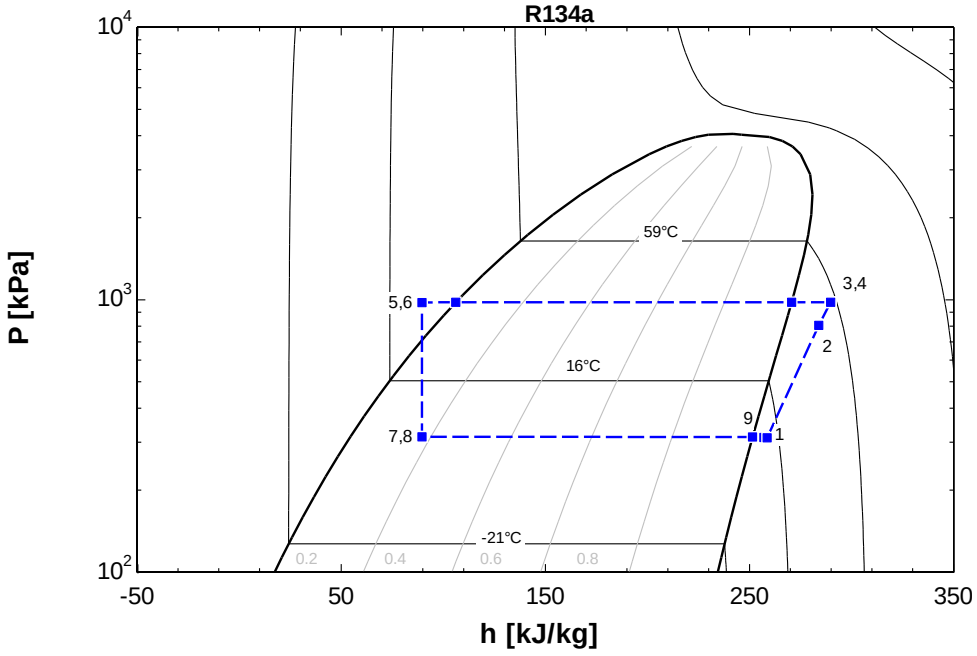

Figure **Error! No text of specified style in document.**.31. Mission 2, Segment Six, P-h Diagram

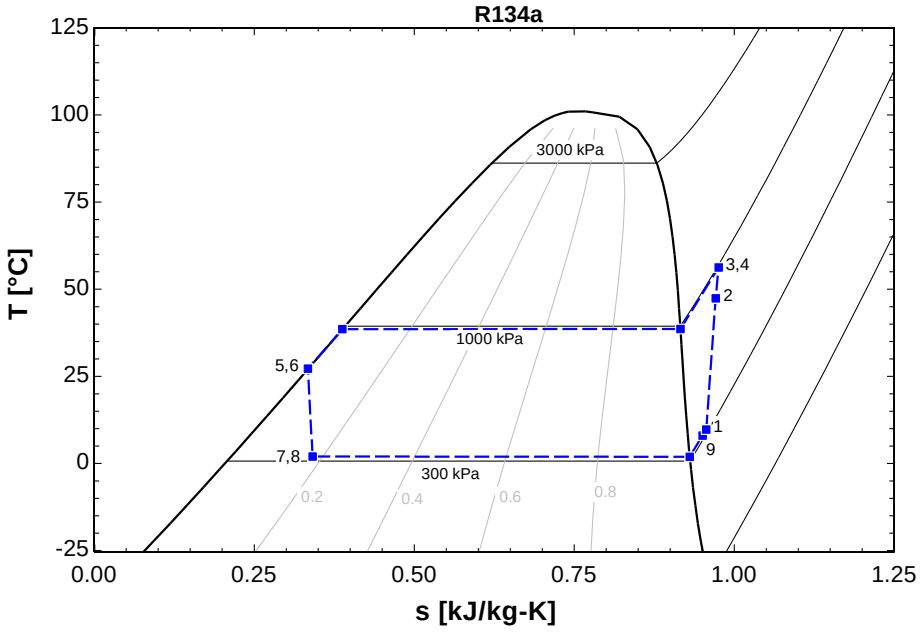

Figure **Error! No text of specified style in document.**.32. Mission 2, Segment Six, T-s Diagram

A.5 Energy Based Analysis Results

Table **Error! No text of specified style in document.**.9. Vapor Compression Cycle Cooling System Fuel Penalty Breakdown

VCC, Mission 1					
Segment	$\dot{m}_{fo,sys}$ **(kg Fuel)**	$\dot{m}_{fo,ram}$ **(kg Fuel)**	$\dot{m}_{fo,bleed}$ **(kg Fuel)**	$\dot{m}_{fo,pto}$ **(kg Fuel)**	$\dot{m}_{fo,tot}$ **(kg fuel)**
1	0	0	0	21.06	21.06
2	3.453	9.72	0	4.387	17.56
3	1.420	11.01	0	4.376	16.81
4	3.453	9.72	0	4.387	17.56
5	2.641	4.341	0	2.882	9.86
VCC, Mission 2					
Segment	$\dot{m}_{fo,sys}$ **(kg Fuel)**	$\dot{m}_{fo,ram}$ **(kg Fuel)**	$\dot{m}_{fo,bleed}$ **(kg Fuel)**	$\dot{m}_{fo,pto}$ **(kg Fuel)**	$\dot{m}_{fo,tot}$ **(kg fuel)**
1	0	0	0	21.06	21.06
2	7.308	26.13	0	9.050	42.49
3	4.062	9.62	0	5.387	19.06
4	1.713	16.11	0	3.327	21.15
5	7.308	26.13	0	9.050	42.49
6	2.800	7.660	0	2.923	13.38

A.6 Exergy Based Analysis Results

Table **Error! No text of specified style in document.**.10. Vapor Compression Cycle System Exergy Flow Breakdown for Mission 1

Segment	**1**	**2**	**3**	**4**	**5**
$\dot{\Psi}_{TMS,\,in}$ **(kW)**	0	0	0	0	0
$\dot{\Psi}_{TMS,\,Overboard}$ **(kW)**	0	0	0	0	0
$\dot{\Psi}_{Ram,\,In}$ **(kW)**	1.466	43.32	132.2	43.32	14.61
$\dot{\Psi}_{Ram,\,Out}$ **(kW)**	4.600	31.59	89.62	31.59	11.70
$\dot{\Psi}_{Avionics,\,Out}$ **(kW)**	0.4186	29.84	20.80	29.84	14.07
$\dot{W}_{TMS,\,in}$ **(kW)**	31.54	20.23	82.80	20.23	15.37
$\dot{\Psi}_{TMS,\,out}$ **(kW)**	2.609	9.350	2.909	9.350	1.380
$\dot{I}_{TMS}$ **(kW)**	26.2	52.5	143	52.5	31.0

$\eta_{ex,TMS}$ **(%)**	7.81	10.01	1.23	10.01	3.13

Table **Error! No text of specified style in document.**.11. Vapor Compression Cycle System Exergy Flow Breakdown for Mission 2

Segment	1	2	3	4	5	6
$\dot{\Psi}_{\text{TMS, in}}$ **(kW)**	0	0	0	0	0	0
$\dot{\Psi}_{\text{TMS, Overboard}}$ **(kW)**	0	0	0	0	0	0
$\dot{\Psi}_{\text{Ram, In}}$ **(kW)**	1.466	52.10	24.70	103.4	52.10	27.29
$\dot{\Psi}_{\text{Ram, Out}}$ **(kW)**	4.600	33.20	19.94	61.58	33.20	14.76
$\dot{\Psi}_{\text{Avionics, Out}}$ **(kW)**	0.4186	23.73	23.46	1.353	23.73	11.58
$\dot{W}_{\text{TMS, in}}$ **(kW)**	31.54	22.57	21.81	138.4	22.57	18.38
$\dot{\Psi}_{\text{TMS, out}}$ **(kW)**	2.609	6.110	5.172	3.123	6.134	0.7709
$\dot{I}_{\text{TMS}}$ **(kW)**	26.2	59.1	44.9	178	59.1	41.7
$\eta_{ex,TMS}$**(%)**	7.81	6.21	7.39	1.28	6.23	1.35

Table **Error! No text of specified style in document.**.12. Vapor Compression Cycle Component Performance Breakdown for Mission 1

Mission One Segment One, Ground Idle					
Component	$\dot{Q}$ **(kW)**	$\dot{W}$**(kW)**	$\dot{I}$ **(W)**	$\dot{I}$ **(%)**	η_{rev} **(%)**
Compressor, Stage 1		16.6981	3029	11.6	81.9
Compressor Stage 2		14.8425	2739	10.5	81.5
Discharge Line			4.280	0.0	99.99
Condenser	-96.5657		4847	18.5	39.3
Liquid Line			0.2627	0.0	99.999
Expansion Valve 1			2596	9.9	83.7
Evaporator 1	32.5193		3172	12.1	76.6
Suction Line 1			29.55	0.1	99.7
Expansion Valve 2			2593	9.9	83.7
Evaporator 2	32.5058		3159	12.1	76.7
Suction Line 2			29.66	0.1	99.7
Hot Gas Bypass & Mixing			3997	15.3	70.6
	-31.5406	31.5406	26195	1.0	

Table Error! No text of specified style in document..12. Vapor Compression Cycle Component Performance Breakdown for Mission 1 Continued

Mission One Segment Two, Cruise In					
Component	$\dot{Q}$ **(kW)**	$\dot{W}$**(kW)**	$\dot{I}$ **(W)**	$\dot{I}$ **(%)**	η_{rev} **(%)**
Compressor, Stage 1		16.876	2425	4.63	85.6
Compressor Stage 2		3.356	601.4	1.15	82.1
Discharge Line			20.78	0.0396	99.96
Condenser	-127.988		38564	73.56	43.7
Liquid Line			0.2449	0.000467	99.999
Expansion Valve 1			536.0	1.02	95.7
Evaporator 1	53.889		4534	8.65	83.0
Suction Line 1			32.70	0.0624	99.8
Expansion Valve 2			534.9	1.02	95.7
Evaporator 2	53.867		4510	8.60	83.1
Suction Line 2			32.64	0.0623	99.8
Hot Gas Bypass & Mixing			635.9	1.21	87.2
	-20.232	20.232	52428	1.0	
Mission One Segment Three, Combat					
Component	$\dot{Q}$ **(kW)**	$\dot{W}$**(kW)**	$\dot{I}$ **(W)**	$\dot{I}$ **(%)**	η_{rev} **(%)**
Compressor, Stage 1		38.11	5224	3.66	86.3
Compressor Stage 2		44.69	5862	4.11	86.9
Discharge Line			38.52	0.0270	99.97
Condenser	-232.74		96657	67.7	78.6
Liquid Line			4.930	0.0034556	99.99
Expansion Valve 1			8708	6.10	77.5
Evaporator 1	75.00		7479	5.24	81.4
Suction Line 1			480.6	0.337	98.5
Expansion Valve 2			8692	6.09	77.5
Evaporator 2	74.94		7462	5.23	81.5
Suction Line 2			478.0	0.335	98.5
Hot Gas Bypass & Mixing			1591	1.11	77.2
	-82.80	82.80	142676	1.0	

Table **Error! No text of specified style in document.**.12. Vapor Compression Cycle Component Performance Breakdown for Mission 1 Continued

Mission One Segment Four, Cruise In					
Component	$\dot{Q}$ **(kW)**	$\dot{W}$**(kW)**	$\dot{I}$ **(W)**	$\dot{I}$ **(%)**	η_{rev} **(%)**
Compressor, Stage 1		16.876	2425	4.63	85.6
Compressor Stage 2		3.36	601.4	1.15	82.1
Discharge Line			20.78	0.0396	99.96
Condenser	-127.988		38564	73.6	43.7
Liquid Line			0.2449	0.0004671	99.999
Expansion Valve 1			536	1.02	95.7
Evaporator 1	53.889		4534	8.65	83.0
Suction Line 1			32.70	0.0624	99.8
Expansion Valve 2	53.867		534.9	1.02	95.7
Evaporator 2			4510	8.60	83.1
Suction Line 2			32.64	0.0623	99.8
Hot Gas Bypass & Mixing			635.9	1.21	87.2
	-20.232	20.232	52428	1.0	
Mission One Segment Five, Loiter					
Component	$\dot{Q}$ **(kW)**	$\dot{W}$**(kW)**	$\dot{I}$ **(W)**	$\dot{I}$ **(%)**	η_{rev} **(%)**
Compressor, Stage 1		14.262	2219	7.17	84.4
Compressor Stage 2		1.111	215.7	0.697	80.6
Discharge Line			24.63	0.0796	99.9
Condenser	-111.919		18004	58.2	19.3
Liquid Line			0.2033	0.0006568	99.999
Expansion Valve 1			332.6	1.07	96.8
Evaporator 1	48.282		4655	15.0	72.7
Suction Line 1			28.14	0.0909	99.8
Expansion Valve 2			331.8	1.07	96.8
Evaporator 2	48.263		4626	14.9	72.8
Suction Line 2			28.08	0.0907	99.8
Hot Gas Bypass & Mixing			483.3	1.56	84.7
	-15.373	15.373	30948	1.0	

Table **Error! No text of specified style in document.**.13. Vapor Compression Cycle Component Performance Breakdown for Mission 2

Mission Two Segment One, Ground Idle					
Component	$\dot{Q}$ **(kW)**	$\dot{W}$**(kW)**	$\dot{I}$ **(W)**	$\dot{I}$ **(%)**	η_{rev} **(%)**
Compressor, Stage 1		16.6981	3029	11.6	81.9
Compressor Stage 2		14.8425	2739	10.5	81.5
Discharge Line			4.280	0.0163	99.99
Condenser	-96.5657		4847	18.5	39.3
Liquid Line			0.2627	0.0010027	99.999
Expansion Valve 1			2596	9.91	83.7
Evaporator 1	32.5193		3172	12.1	76.6
Suction Line 1			29.55	0.113	99.7
Expansion Valve 2			2593	9.90	83.7
Evaporator 2	32.5058		3159	12.1	76.7
Suction Line 2			29.66	0.113	99.7
Hot Gas Bypass & Mixing			3997	15.3	70.6
	-31.5406	31.5406	26195	1.0	
Mission Two Segment Two, Cruise In					
Component	$\dot{Q}$ **(kW)**	$\dot{W}$**(kW)**	$\dot{I}$ **(W)**	$\dot{I}$ **(%)**	η_{rev} **(%)**
Compressor, Stage 1		17.4130	2572	4.35	85.2
Compressor Stage 2		5.1597	940.7	1.59	81.8
Discharge Line			18.63	0.0315	99.96
Condenser	-128.1847		44197	74.8	74.7
Liquid Line			0.3677	0.0006224	99.999
Expansion Valve 1	52.8168		760.9	1.29	94.3
Evaporator 1	52.7952		4450	7.53	81.8
Suction Line 1			32.63	0.0552	99.8
Expansion Valve 2			759.6	1.29	94.3
Evaporator 2			4470	7.57	81.7
Suction Line 2			32.57	0.0551	99.8
Hot Gas Bypass & Mixing			836.4	1.42	85.7
	-22.5727	22.5727	59071	1.0	

Table **Error! No text of specified style in document.**.13. Vapor Compression Cycle Component Performance Breakdown for Mission 2 Continued

Mission Two Segment Three, Loiter					
Component	$\dot{Q}$ **(kW)**	$\dot{W}$**(kW)**	$\dot{I}$ **(W)**	$\dot{I}$ **(%)**	η_{rev} **(%)**
Compressor, Stage 1		18.885	2813	6.29	85.1
Compressor Stage 2		2.921	543.3	1.22	81.4
Discharge Line			36.17	0.0809	99.9
Condenser	-146.777		28009	62.7	20.4
Liquid Line			0.801	0.00179	99.997
Expansion Valve 1			564.3	1.26	96.1
Evaporator 1	62.500		5784	12.9	77.4
Suction Line 1			49.82	0.111	99.7
Expansion Valve 2			563.0	1.26	96.1
Evaporator 2	62.471		5781	12.9	77.5
Suction Line 2			49.20	0.110	99.7
Hot Gas Bypass & Mixing			510.9	1.14	85.3
	-21.806	21.806	44705	1.0	
Mission Two Segment Four, Dash					
Component	$\dot{Q}$ **(kW)**	$\dot{W}$**(kW)**	$\dot{I}$ **(W)**	$\dot{I}$ **(%)**	η_{rev} **(%)**
Compressor, Stage 1		56.3014	8509	4.78	84.9
Compressor Stage 2		82.1242	11101	6.23	86.5
Discharge Line			70.53	0.0396	99.96
Condenser	-286.3028		87663	49.2	91.1
Liquid Line			31.94	0.0179	99.98
Expansion Valve 1			25370	14.2	64.6
Evaporator 1	73.9813		7858	4.41	83.3
Suction Line 1			1989	1.12	94.7
Expansion Valve 2	73.8959		25319	14.2	64.7
Evaporator 2			7829	4.40	83.4
Suction Line 2			1973	1.11	94.8
Hot Gas Bypass & Mixing			420.4	0.236	68.9
	-138.4256	138.4256	178134	1.0	

Table **Error! No text of specified style in document.**.13. Vapor Compression Cycle Component Performance Breakdown for Mission 2 Continued

Mission Two Segment Five, Cruise In					
Component	$\dot{Q}$ **(kW)**	$\dot{W}$**(kW)**	$\dot{I}$ **(W)**	$\dot{I}$ **(%)**	η_{rev} **(%)**
Compressor, Stage 1		17.4130	2572	4.36	85.2
Compressor Stage 2		5.1597	940.7	1.593	81.8
Discharge Line			18.63	0.0316	99.96
Condenser	-128.1847		44197	74.8	74.7
Liquid Line			0.3677	0.0006227	99.999
Expansion Valve 1			760.93	1.29	94.3
Evaporator 1	52.8168		4450	7.5	81.8
Suction Line 1			32.63	0.0553	99.8
Expansion Valve 2			759.6	1.29	94.3
Evaporator 2	52.7952		4447	7.5	81.8
Suction Line 2			32.57	0.0552	99.8
Hot Gas Bypass & Mixing			836.4	1.42	85.7
	-22.5727	22.5727	59048	1.0	
Mission Two Segment Six, Loiter					
Component	$\dot{Q}$ **(kW)**	$\dot{W}$**(kW)**	$\dot{I}$ **(W)**	$\dot{I}$ **(%)**	η_{rev} **(%)**
Compressor, Stage 1		14.93	2351	5.64	84.2
Compressor Stage 2		3.45	681.5	1.634	80.3
Discharge Line			18.81	0.0451	99.95
Condenser	-112.55		27803	66.7	82.0
Liquid Line			0.2072	0.000497	99.999
Expansion Valve 1			562.6	1.35	95.1
Evaporator 1	47.09		4472	10.7	73.1
Suction Line 1			29.49	0.0707	99.7
Expansion Valve 2	47.08		561.6	1.35	95.1
Evaporator 2			4453	10.7	73.2
Suction Line 2			29.43	0.0706	99.8
Hot Gas Bypass & Mixing			732.6	1.76	83.0
	-18.38	18.38	41695	1.0	

APPENDIX B. REVERSED BRAYTON CYLE MODEL DETAILS

B.1 System Model Diagrams

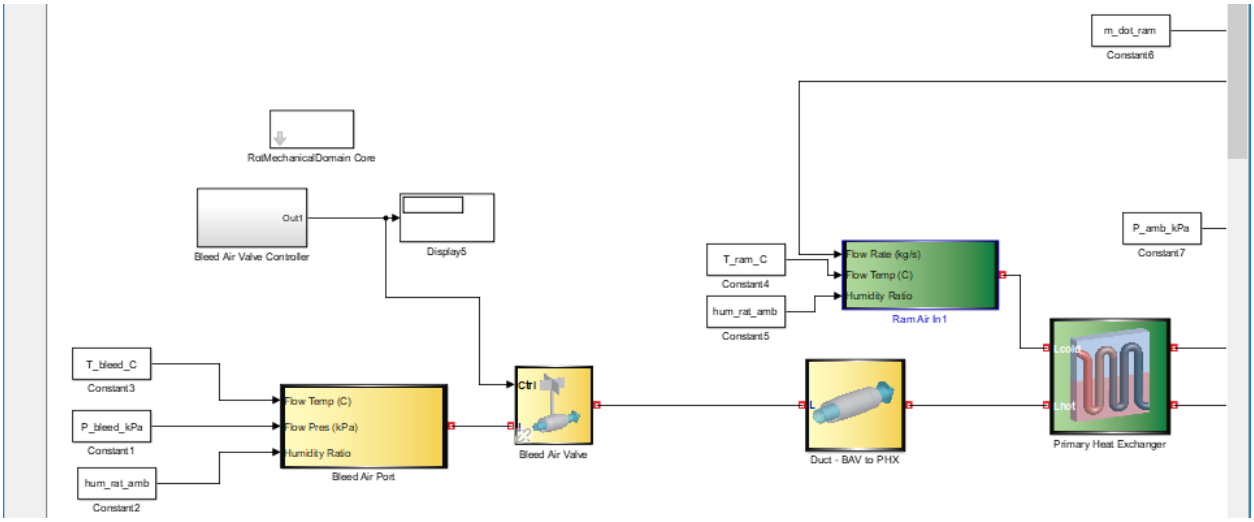

Figure **Error! No text of specified style in document.**.33. Bleed Air Valve and Primary Heat Exchanger

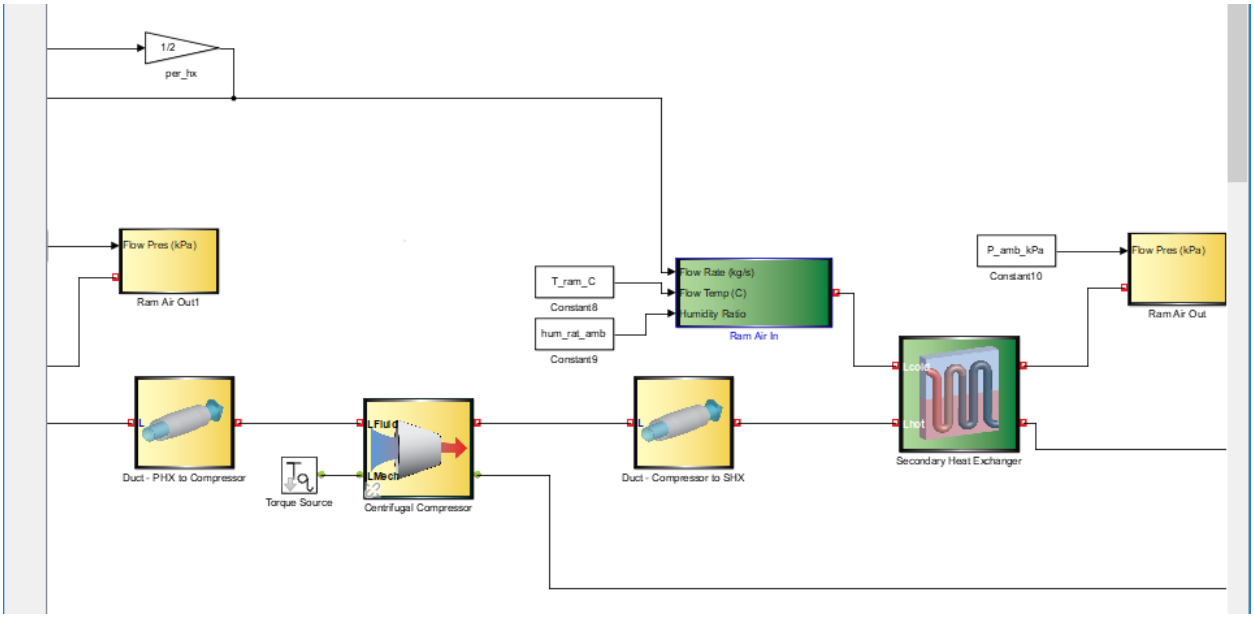

Figure **Error! No text of specified style in document.**.34. Compressor and Secondary Heat exchanger

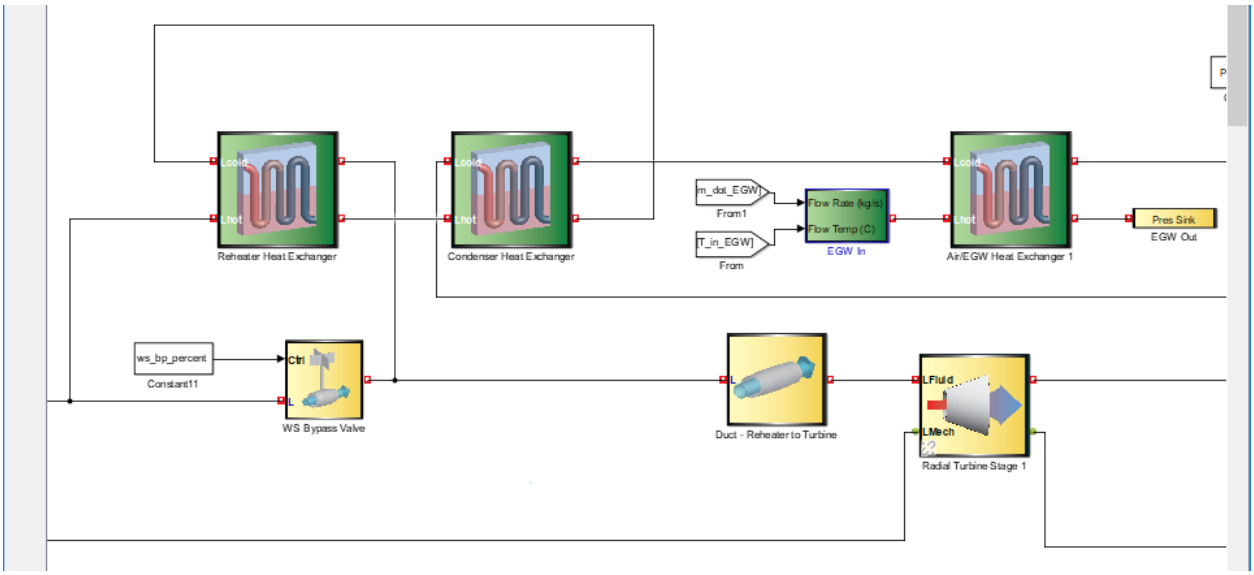

Figure **Error! No text of specified style in document.**.35. Reheater, Condenser, Water Separator Bypass Valve, Turbine Stage 1 and Liquid Heat Exchanger

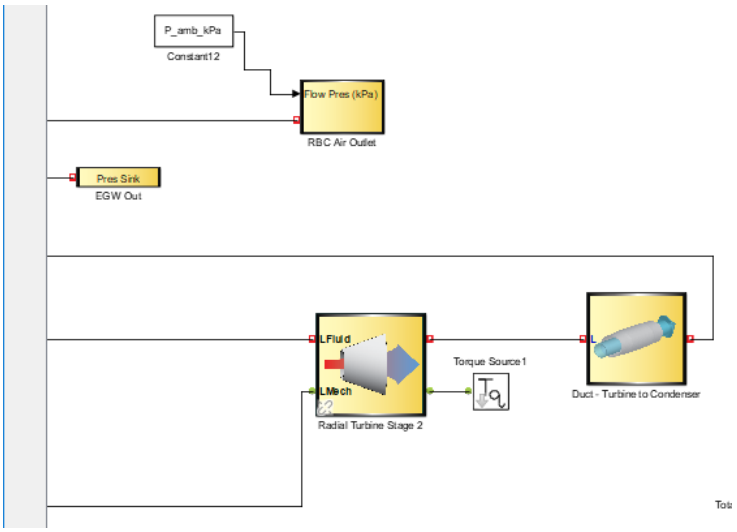

Figure **Error! No text of specified style in document.**.36. Turbine Stage 2 and Air Outlet

B.2 Component Details

Table **Error! No text of specified style in document.**.14. Turbomachinery Information

Component	Rotor Diameter (mm)	Mass (kg)	Material
Air Compressor	241	12.073	Stainless Steel
Expansion Turbine Stage 1	211	43.8614	Stainless Steel
Expansion Turbine Stage 2	208	48.0697	Stainless Steel

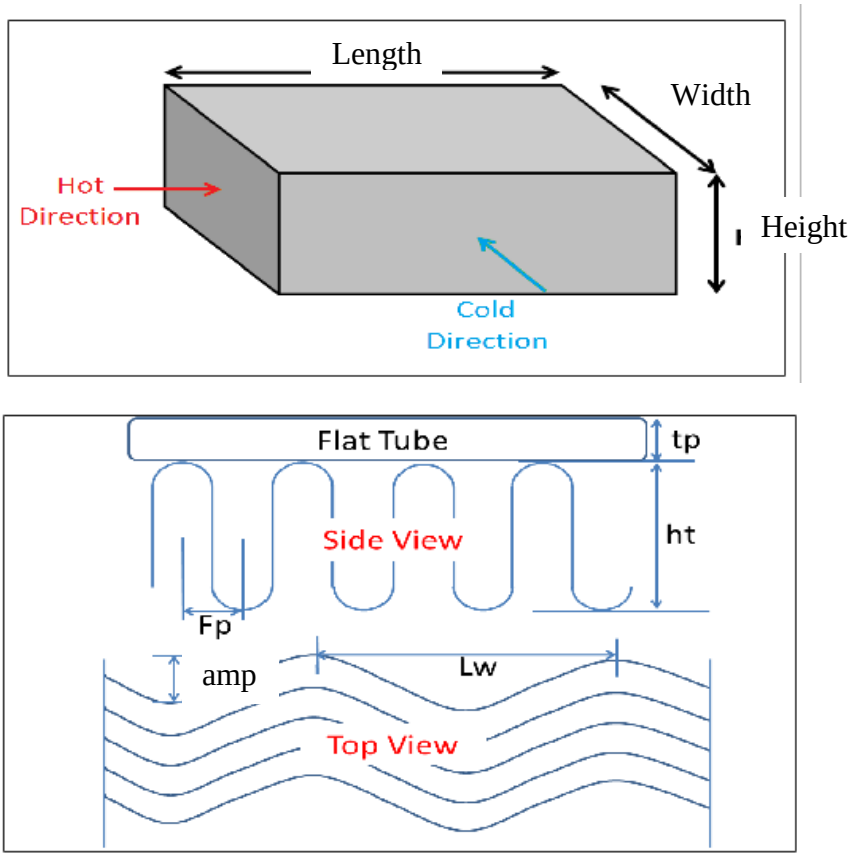

Figure **Error! No text of specified style in document.**.37. Tactical Aircraft Model Primary, Secondary, Reheater and Condenser Heat Exchanger Diagram

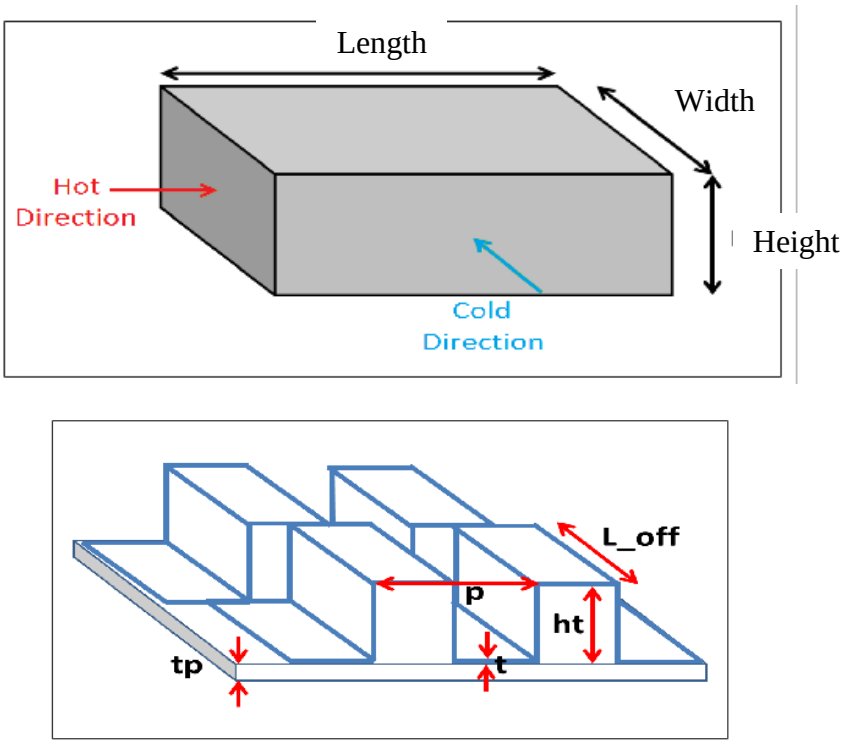

Figure **Error! No text of specified style in document.**.38. Tactical Aircraft Model Liquid Heat Exchanger Diagram

Table **Error! No text of specified style in document.**.15. Heat Exchanger Details

Tactical Aircraft Heat Exchangers	Heat Exchanger Type	Flow Configuration	Material
Primary Heat Exchanger	Plate-fin	Cross-flow	NI201
Secondary Heat Exchanger	Plate-fin	Cross-flow	NI201
Reheater Heat Exchanger	Plate-fin	Cross-flow	Al
Condenser Heat Exchanger	Plate-fin	Cross-flow	Al
Liquid Load Heat Exchanger	Plate-fin	Cross-Flow	Al

Table **Error! No text of specified style in document.**.16. Heat Exchanger Dimensions

Component	Height (m)	Width (m)	Length (m)	Dry Mass (kg)
Liquid Load Heat Exchanger	0.235	0.323	0.602	23.7227

Table **Error! No text of specified style in document.**.17. Heat Exchanger Fin Details

Component	**Side**	**Fin Structure**	**p (mm)**	**h_t (mm)**	**t (mm)**	**L_{off} (mm)**	**t_p (mm)**	**Pass**
Liquid Load Heat Exchanger	Hot	Offset Fin	6.3246	1.803	0.102	2.54	0.204	4
	Cold	Offset Fin	2.622	1.803	0.102	2.54	0.204	1

Table **Error! No text of specified style in document.**.18. Tactical Aircraft Reversed Brayton Cycle Cooling System Mass Breakdown

Component	**m (kg)**
Primary Heat Exchanger	21.2
Air Compressor	12.1
Secondary Heat Exchanger	22.3
Reheater	15.7
Condenser	3.5
Expansion Turbine Stage 1	43.9
Expansion Turbine Stage 2	48.1
Liquid Load Heat Exchanger	23.7
Valve Totals	10.0
Duct Totals	45.9
System Total	246.3

B.3 Verification and Validation Model Detailed Results

Table **Error! No text of specified style in document.**.19. Validation Data and Model Temperature Relative Comparison

Parameter	Run 1 Relative Error	Run 2 Relative Error	Run 3 Relative Error
$T_{out,\ PHX,\ hot}$	0.99%	-1.98%	1.24%
$T_{out,\ PHX,\ cold}$	0.71%	-2.81%	0.42%
$T_{out,\ comp}$	5.7%	3.33%	7.6%
$T_{out,\ SHX,\ hot}$	5.2%	7.2%	9.6%
$T_{out,\ SHX,\ cold}$	3.07%	3.24%	8.5%
$T_{out,\ LHX\ 1,\ hot}$	2.63%	5.8%	6.1%
$T_{out,\ rhtr\ hot}$	4.5%	0.8%	9.0%
$T_{out,\ cond,\ hot}$	10.8%	1.8%	18%
$T_{out,\ rhtr,\ cold}$	4.6%	2.1%	8.9%
$T_{out,\ turb}$	-7.4%	-4.1%	3.3%
$T_{out,\ cond,\ cold}$	-1.7%	-2.0%	2.7%
$T_{out,\ LHX\ 2,\ cold}$	0.65%	-1.6%	3.9%

Table **Error! No text of specified style in document.**.20. Validation Data and Model Pressure and Mass Flow Rate Relative Comparison

Parameter	Run 1 Relative Error	Run 2 Relative Error	Run 3 Relative Error
$\mathbf{P_{out,\ PHX,\ hot}}$	-1.87%	0.28%	-0.97%
$\mathbf{P_{out,\ comp}}$	7.62%	15.09%	13.21%
$\mathbf{P_{out,\ SHX,\ hot}}$	7.93%	15.85%	13.72%
$\mathbf{P_{out,\ LHX\ 1,\ hot}}$	7.95%	14.43%	12.67%
$\mathbf{P_{out,\ rhtr\ hot}}$	8.44%	14.63%	13.11%
$\mathbf{P_{out,\ cond,\ hot}}$	9.77%	14.70%	14.52%
$\mathbf{P_{out,\ rhtr,\ cold}}$	11.24%	14.71%	16.00%
$\mathbf{P_{out,\ turb}}$	-7.08%	-32.64%	-10.51%
$\mathbf{P_{out,\ cond,\ cold}}$	-11.00%	-30.82%	-12.25%
$\mathbf{P_{out,\ LHX\ 2,\ cold}}$	-7.82%	-29.63%	-9.83%
$\mathbf{P_{r,\ comp}}$	10.2%	12.7%	15.7%
$\mathbf{P_{r,\ turb}}$	19.6%	69.8%	29.4%
Parameter	**Run 1 Relative Error**	**Run 2 Relative Error**	**Run 3 Relative Error**
$\dot{m}_{BAV}$	5.52%	-3.66%	4.26%
$\dot{m}_{W/S\ bypass}$	-10.4%	-4.32%	-7.14%
Removed Water $\dot{m}$	-13.3%	-100%	-26.9%

B.4 Tactical Aircraft Model Detailed Results

Table **Error! No text of specified style in document.**.21. Reversed-Brayton Cycle System Model Convergence

Mission 1			Mission 2		
Segment	**Mass Balance (kg/s)**	**Energy Balance (W)**	**Segment**	**Mass Balance (kg/s)**	**Energy Balance (W)**
1	7.16E-12	-4.58E-02	1	7.16E-12	-4.58E-02
2	5.32E-12	-7.16E-02	2	2.88E-12	-3.25E-02
3	-1.94E-07	2.56E-01	3	5.90E-06	-4.80E-01
4	5.32E-12	-7.16E-02	4	2.22E-16	-7.36E-06
5	-3.45E-07	-1.65E-01	5	2.88E-12	-3.25E-02
			6	-1.18E-11	-8.15E-02

Table **Error! No text of specified style in document.**.22. Reversed Brayton Cycle Results

Mission One Segment One, Ground Idle						
State	**Description**	**P (kPa)**	**T (^{o}C)**	**h (kJ/kg)**	**s (kJ/kg-K)**	$\dot{m}$ **(kg/s)**
0	Ambient	101.3	41.00	36.63	6.913	0
1	Bleed Air Valve Inlet	608.0	341.0	344.3	7.084	0.4630
2	Bleed Air Valve Outlet	414.6	341.0	344.3	7.194	0.4630
3	PHX Inlet	384.1	341.0	344.3	7.216	0.4630
4	PHX Outlet	356.4	75.86	71.77	6.657	0.4630
5	Compressor Inlet	349.0	75.86	71.77	6.663	0.4630
6	Compressor Outlet	707.7	184.4	181.9	6.734	0.4630
7	SHX Inlet	702.4	184.4	181.9	6.736	0.4630
8	SHX Outlet	676.2	54.12	49.85	6.406	0.4630
9	RHX Hot Side Inlet	676.2	54.12	49.85	6.406	0.4267
10	RHX Hot Side Outlet	670.8	-7.400	-12.07	6.197	0.4267
11	CHX Hot Side Inlet	670.8	-7.398	-12.07	6.197	0.4267
12	CHX Hot Side Outlet	670.5	-34.03	-38.86	6.089	0.4267
13	RHX Cold Side Inlet	670.5	-34.03	-38.86	6.089	0.4267
14	RHX Cold Side Outlet	665.3	27.52	23.06	6.325	0.4267
15	Turbine Stage 1 Inlet	661.9	29.61	25.16	6.333	0.4630
16	Turbine Stage 1 Outlet	193.0	-47.82	-52.72	6.392	0.4630
17	Turbine Stage 2 Inlet	193.0	-47.82	-52.72	6.392	0.4630
18	Turbine Stage 2 Outlet	103.6	-79.85	-84.97	6.418	0.4630
19	CHX Cold Side Inlet	103.2	-79.85	-84.97	6.419	0.4630
20	CHX Cold Side Outlet	103.0	-55.33	-60.29	6.540	0.4630
21	LHX Cold Side Inlet	103.0	-55.33	-60.29	6.540	0.4630
22	LHX Cold Side Outlet	101.3	50.66	46.35	6.943	0.4630

Table **Error! No text of specified style in document.**.22. Reversed Brayton Cycle Results Continued

Mission One Segment Two, Cruise Out						
State	**Description**	**P (kPa)**	**T (oC)**	**h (kJ/kg)**	**s (kJ/kg-K)**	$\dot{m}$ **(kg/s)**
0	Ambient	23.84	-23.77	-28.54	7.097	0
1	Bleed Air Valve Inlet	963.6	490.3	504.2	7.185	0.5797
2	Bleed Air Valve Outlet	426.1	490.3	504.2	7.420	0.5797
3	PHX Inlet	359.3	490.3	504.2	7.469	0.5797
4	PHX Outlet	311.3	81.63	77.61	6.712	0.5797
5	Compressor Inlet	297.2	81.65	77.61	6.726	0.5797
6	Compressor Outlet	869.5	243.7	242.8	6.801	0.5797
7	SHX Inlet	861.9	243.7	242.8	6.803	0.5797
8	SHX Outlet	830.7	39.53	35.15	6.300	0.5797
9	RHX Hot Side Inlet	830.7	39.53	35.15	6.300	0.2379
10	RHX Hot Side Outlet	829.4	-62.99	-68.01	5.893	0.2379
11	CHX Hot Side Inlet	829.4	-63.00	-68.01	5.893	0.2379
12	CHX Hot Side Outlet	829.3	-105.4	-110.8	5.657	0.2379
13	RHX Cold Side Inlet	829.3	-105.4	-110.8	5.657	0.2379
14	RHX Cold Side Outlet	828.0	-2.956	-7.601	6.152	0.2379
15	Turbine Stage 1 Inlet	823.9	22.10	17.60	6.244	0.5797
16	Turbine Stage 1 Outlet	164.3	-74.13	-79.21	6.314	0.5797
17	Turbine Stage 2 Inlet	164.3	-74.13	-79.21	6.314	0.5797
18	Turbine Stage 2 Outlet	32.49	-141.7	-147.6	6.365	0.5797
19	CHX Cold Side Inlet	31.71	-141.7	-147.6	6.372	0.5797
20	CHX Cold Side Outlet	31.27	-124.5	-130.1	6.500	0.5797
21	LHX Cold Side Inlet	31.27	-124.5	-130.1	6.499	0.5797
22	LHX Cold Side Outlet	23.84	51.73	47.44	7.363	0.5797

Table **Error! No text of specified style in document.**.22. Reversed Brayton Cycle Results Continued

Mission One Segment Three, Combat						
State	**Description**	**P (kPa)**	**T (oC)**	**h (kJ/kg)**	**s (kJ/kg-K)**	$\dot{m}$ **(kg/s)**
0	Ambient	46.56	-0.5601	-0.5194	6.994	0
1	Bleed Air Valve Inlet	1491	496.5	511.0	7.068	1.010
2	Bleed Air Valve Outlet	762.2	496.5	511.0	7.261	1.010
3	PHX Inlet	649.7	496.5	511.0	7.307	1.010
4	PHX Outlet	577.6	119.0	115.4	6.635	1.010
5	Compressor Inlet	552.2	119.0	115.4	6.649	1.010
6	Compressor Outlet	1579	291.8	292.7	6.721	1.010
7	SHX Inlet	1565	291.8	292.7	6.723	1.010
8	SHX Outlet	1515	80.77	76.72	6.250	1.010
9	RHX Hot Side Inlet	1515	80.77	76.72	6.250	0.941
10	RHX Hot Side Outlet	1506	-0.4922	-5.123	5.984	0.941
11	CHX Hot Side Inlet	1506	-0.4895	-5.123	5.984	0.941
12	CHX Hot Side Outlet	1505	-38.86	-43.71	5.826	0.941
13	RHX Cold Side Inlet	1505	-38.86	-43.71	5.826	0.941
14	RHX Cold Side Outlet	1497	42.48	38.13	6.136	0.941
15	Turbine Stage 1 Inlet	1489	45.08	40.74	6.146	1.010
16	Turbine Stage 1 Outlet	297.0	-57.95	-62.92	6.221	1.010
17	Turbine Stage 2 Inlet	297.0	-57.95	-62.92	6.221	1.010
18	Turbine Stage 2 Outlet	58.65	-130.9	-136.6	6.273	1.010
19	CHX Cold Side Inlet	57.25	-130.9	-136.6	6.280	1.010
20	CHX Cold Side Outlet	56.58	-95.34	-100.6	6.508	1.010
21	LHX Cold Side Inlet	56.58	-95.34	-100.6	6.508	1.010
22	LHX Cold Side Outlet	46.56	50.01	45.70	7.165	1.010

Table **Error! No text of specified style in document.**.22. Reversed Brayton Cycle Results

Continued

Mission One Segment Four, Cruise In						
State	**Description**	**P (kPa)**	**T (oC)**	**h (kJ/kg)**	**s (kJ/kg-K)**	$\dot{m}$ **(kg/s)**
0	Ambient	23.84	-23.77	-28.54	7.097	0
1	Bleed Air Valve Inlet	963.6	490.3	504.2	7.185	0.5797
2	Bleed Air Valve Outlet	426.1	490.3	504.2	7.420	0.5797
3	PHX Inlet	359.3	490.3	504.2	7.469	0.5797
4	PHX Outlet	311.3	81.63	77.61	6.712	0.5797
5	Compressor Inlet	297.2	81.65	77.61	6.726	0.5797
6	Compressor Outlet	869.5	243.7	242.8	6.801	0.5797
7	SHX Inlet	861.9	243.7	242.8	6.803	0.5797
8	SHX Outlet	830.7	39.53	35.15	6.300	0.5797
9	RHX Hot Side Inlet	830.7	39.53	35.15	6.300	0.2379
10	RHX Hot Side Outlet	829.4	-62.99	-68.01	5.893	0.2379
11	CHX Hot Side Inlet	829.4	-63.00	-68.01	5.893	0.2379
12	CHX Hot Side Outlet	829.3	-105.4	-110.8	5.657	0.2379
13	RHX Cold Side Inlet	829.3	-105.4	-110.8	5.657	0.2379
14	RHX Cold Side Outlet	828.0	-2.956	-7.601	6.152	0.2379
15	Turbine Stage 1 Inlet	823.9	22.10	17.60	6.244	0.5797
16	Turbine Stage 1 Outlet	164.3	-74.13	-79.21	6.314	0.5797
17	Turbine Stage 2 Inlet	164.3	-74.13	-79.21	6.314	0.5797
18	Turbine Stage 2 Outlet	32.49	-141.7	-147.6	6.365	0.5797
19	CHX Cold Side Inlet	31.71	-141.7	-147.6	6.372	0.5797
20	CHX Cold Side Outlet	31.27	-124.5	-130.1	6.500	0.5797
21	LHX Cold Side Inlet	31.27	-124.5	-130.1	6.499	0.5797
22	LHX Cold Side Outlet	23.84	51.73	47.44	7.363	0.5797

Table **Error! No text of specified style in document.**.22. Reversed Brayton Cycle Results Continued

Mission One Segment Five, Loiter						
State	**Description**	**P (kPa)**	**T (oC)**	**h (kJ/kg)**	**s (kJ/kg-K)**	$\dot{m}$ **(kg/s)**
0	Ambient	37.60	-8.960	-13.64	7.024	0
1	Bleed Air Valve Inlet	381.4	259.3	258.9	7.069	0.4690
2	Bleed Air Valve Outlet	329.8	259.3	258.9	7.111	0.4690
3	PHX Inlet	293.5	259.3	258.9	7.144	0.4690
4	PHX Outlet	262.5	33.02	28.60	6.613	0.4690
5	Compressor Inlet	253.2	33.02	28.60	6.623	0.4690
6	Compressor Outlet	668.6	160.5	157.5	6.696	0.4690
7	SHX Inlet	663.2	160.5	157.5	6.698	0.4690
8	SHX Outlet	638.3	17.94	13.41	6.304	0.4690
9	RHX Hot Side Inlet	638.3	17.94	13.41	6.304	0.4339
10	RHX Hot Side Outlet	633.5	-50.84	-55.77	6.031	0.4339
11	CHX Hot Side Inlet	633.5	-50.84	-55.77	6.031	0.4339
12	CHX Hot Side Outlet	633.3	-80.97	-86.10	5.882	0.4339
13	RHX Cold Side Inlet	633.3	-80.97	-86.10	5.882	0.4339
14	RHX Cold Side Outlet	628.7	-12.22	-16.92	6.197	0.4339
15	Turbine Stage 1 Inlet	625.6	-9.96	-14.65	6.207	0.4690
16	Turbine Stage 1 Outlet	138.3	-91.23	-96.45	6.273	0.4690
17	Turbine Stage 2 Inlet	138.3	-91.23	-96.45	6.273	0.4690
18	Turbine Stage 2 Outlet	42.91	-137.7	-143.6	6.314	0.4690
19	CHX Cold Side Inlet	42.00	-137.7	-143.6	6.320	0.4690
20	CHX Cold Side Outlet	41.75	-110.1	-115.5	6.509	0.4690
21	LHX Cold Side Inlet	41.75	-110.1	-115.5	6.509	0.4690
22	LHX Cold Side Outlet	37.60	51.98	47.69	7.233	0.4690

Table **Error! No text of specified style in document.**.22. Reversed Brayton Cycle Results Continued

Mission Two Segment One, Ground Idle						
State	**Description**	**P (kPa)**	**T (oC)**	**h (kJ/kg)**	**s (kJ/kg-K)**	$\dot{m}$ **(kg/s)**
0	Ambient	101.3	41.00	36.63	6.913	0
1	Bleed Air Valve Inlet	608.0	341.0	344.3	7.084	0.4630
2	Bleed Air Valve Outlet	414.6	341.0	344.3	7.194	0.4630
3	PHX Inlet	384.1	341.0	344.3	7.216	0.4630
4	PHX Outlet	356.4	75.86	71.77	6.657	0.4630
5	Compressor Inlet	349.0	75.86	71.77	6.663	0.4630
6	Compressor Outlet	707.7	184.4	181.9	6.734	0.4630
7	SHX Inlet	702.4	184.4	181.9	6.736	0.4630
8	SHX Outlet	676.2	54.12	49.85	6.406	0.4630
9	RHX Hot Side Inlet	676.2	54.12	49.85	6.406	0.4267
10	RHX Hot Side Outlet	670.8	-7.40	-12.07	6.197	0.4267
11	CHX Hot Side Inlet	670.8	-7.40	-12.07	6.197	0.4267
12	CHX Hot Side Outlet	670.5	-34.03	-38.86	6.089	0.4267
13	RHX Cold Side Inlet	670.5	-34.03	-38.86	6.089	0.4267
14	RHX Cold Side Outlet	665.3	27.52	23.06	6.325	0.4267
15	Turbine Stage 1 Inlet	661.9	29.61	25.16	6.333	0.4630
16	Turbine Stage 1 Outlet	193.0	-47.82	-52.72	6.392	0.4630
17	Turbine Stage 2 Inlet	193.0	-47.82	-52.72	6.392	0.4630
18	Turbine Stage 2 Outlet	103.6	-79.85	-84.97	6.418	0.4630
19	CHX Cold Side Inlet	103.2	-79.85	-84.97	6.419	0.4630
20	CHX Cold Side Outlet	103.0	-55.33	-60.29	6.540	0.4630
21	LHX Cold Side Inlet	103.0	-55.33	-60.29	6.540	0.4630
22	LHX Cold Side Outlet	101.3	50.66	46.35	6.943	0.4630

Table **Error! No text of specified style in document.**.22. Reversed Brayton Cycle Results

Continued

Mission Two Segment Two, Cruise Out						
State	**Description**	**P (kPa)**	**T (oC)**	**h (kJ/kg)**	**s (kJ/kg-K)**	$\dot{m}$ **(kg/s)**
0	Ambient	30.09	-16.21	-20.93	7.060	0
1	Bleed Air Valve Inlet	1216	513.4	529.54	7.151	0.5923
2	Bleed Air Valve Outlet	441.0	513.4	529.54	7.442	0.5923
3	PHX Inlet	371.4	513.4	529.54	7.492	0.5923
4	PHX Outlet	323.6	79.27	75.22	6.694	0.5923
5	Compressor Inlet	309.6	79.28	75.22	6.707	0.5923
6	Compressor Outlet	888.5	237.8	236.7	6.782	0.5920
7	SHX Inlet	880.8	237.7	236.6	6.785	0.5923
8	SHX Outlet	849.6	40.83	36.45	6.297	0.5923
9	RHX Hot Side Inlet	849.6	40.83	36.45	6.297	0.2427
10	RHX Hot Side Outlet	848.2	-59.40	-64.40	5.904	0.2427
11	CHX Hot Side Inlet	848.2	-59.41	-64.40	5.904	0.2427
12	CHX Hot Side Outlet	848.1	-100.9	-106.2	5.678	0.2427
13	RHX Cold Side Inlet	848.1	-100.9	-106.2	5.678	0.2427
14	RHX Cold Side Outlet	846.8	-0.7413	-5.373	6.154	0.2427
15	Turbine Stage 1 Inlet	842.6	23.80	19.31	6.243	0.5923
16	Turbine Stage 1 Outlet	171.1	-72.09	-77.16	6.312	0.5923
17	Turbine Stage 2 Inlet	171.1	-72.09	-77.16	6.312	0.5923
18	Turbine Stage 2 Outlet	37.94	-136.3	-142.1	6.360	0.5923
19	CHX Cold Side Inlet	37.05	-136.3	-142.1	6.367	0.5923
20	CHX Cold Side Outlet	36.65	-119.4	-124.9	6.487	0.5923
21	LHX Cold Side Inlet	36.65	-119.4	-124.9	6.487	0.5923
22	LHX Cold Side Outlet	30.09	51.65	47.36	7.296	0.5923

Table **Error! No text of specified style in document.**.22. Reversed Brayton Cycle Results

Continued

Mission Two Segment Three, Loiter						
State	**Description**	**P (kPa)**	**T (oC)**	**h (kJ/kg)**	**s (kJ/kg-K)**	$\dot{m}$ **(kg/s)**
0	Ambient	37.60	-8.960	-13.64	7.024	0
1	Bleed Air Valve Inlet	410.1	270.5	270.5	7.070	0.5673
2	Bleed Air Valve Outlet	393.6	270.5	270.51	7.081	0.5673
3	PHX Inlet	347.7	270.5	270.5	7.117	0.5673
4	PHX Outlet	310.4	42.33	37.97	6.595	0.5673
5	Compressor Inlet	298.5	42.33	37.97	6.606	0.5673
6	Compressor Outlet	817.7	179.0	176.4	6.680	0.5673
7	SHX Inlet	810.9	179.0	176.4	6.683	0.5673
8	SHX Outlet	781.8	26.34	21.87	6.274	0.5673
9	RHX Hot Side Inlet	781.8	26.35	21.87	6.274	0.5263
10	RHX Hot Side Outlet	776.3	-44.69	-49.58	5.999	0.5263
11	CHX Hot Side Inlet	776.3	-44.69	-49.58	5.999	0.5263
12	CHX Hot Side Outlet	775.9	-76.38	-81.47	5.845	0.5263
13	RHX Cold Side Inlet	775.9	-76.38	-81.47	5.845	0.5263
14	RHX Cold Side Outlet	770.7	-5.36	-10.02	6.164	0.5263
15	Turbine Stage 1 Inlet	766.8	-3.06	-7.711	6.174	0.5673
16	Turbine Stage 1 Outlet	162.9	-88.18	-93.38	6.242	0.5673
17	Turbine Stage 2 Inlet	162.9	-88.18	-93.38	6.242	0.5673
18	Turbine Stage 2 Outlet	44.32	-140.2	-146.1	6.286	0.5673
19	CHX Cold Side Inlet	43.36	-140.2	-146.1	6.292	0.5673
20	CHX Cold Side Outlet	43.04	-111.1	-116.5	6.494	0.5673
21	LHX Cold Side Inlet	43.04	-111.1	-116.5	6.494	0.5673
22	LHX Cold Side Outlet	37.60	53.14	48.86	7.236	0.5673

Table **Error! No text of specified style in document.**.22. Reversed Brayton Cycle Results Continued

Mission Two Segment Four, Dash						
State	**Description**	**P (kPa)**	**T (oC)**	**h (kJ/kg)**	**s (kJ/kg-K)**	$\dot{m}$ **(kg/s)**
0	Ambient	100.1	40.30	35.92	6.914	0
1	Bleed Air Valve Inlet	2460	547.3	566.8	6.994	1.231
2	Bleed Air Valve Outlet	996.9	547.3	566.8	7.254	1.231
3	PHX Inlet	864.0	547.3	566.8	7.296	1.231
4	PHX Outlet	783.9	139.2	135.9	6.598	1.231
5	Compressor Inlet	755.2	139.3	135.9	6.609	1.231
6	Compressor Outlet	1964	304.8	306.3	6.682	1.231
7	SHX Inlet	1947	304.8	306.3	6.684	1.231
8	SHX Outlet	1889	98.16	94.29	6.235	1.231
9	RHX Hot Side Inlet	1889	98.16	94.29	6.235	1.148
10	RHX Hot Side Outlet	1878	22.25	17.76	6.000	1.148
11	CHX Hot Side Inlet	1878	22.26	17.76	6.001	1.148
12	CHX Hot Side Outlet	1877	-14.37	-19.08	5.863	1.148
13	RHX Cold Side Inlet	1877	-14.37	-19.08	5.863	1.148
14	RHX Cold Side Outlet	1866	61.65	57.44	6.132	1.148
15	Turbine Stage 1 Inlet	1857	64.10	59.91	6.141	1.231
16	Turbine Stage 1 Outlet	396.6	-41.01	-45.88	6.213	1.231
17	Turbine Stage 2 Inlet	396.6	-41.01	-45.88	6.213	1.231
18	Turbine Stage 2 Outlet	110.6	-105.1	-110.5	6.258	1.231
19	CHX Cold Side Inlet	108.1	-105.1	-110.5	6.264	1.231
20	CHX Cold Side Outlet	107.5	-71.02	-76.08	6.452	1.231
21	LHX Cold Side Inlet	107.5	-71.02	-76.08	6.452	1.231
22	LHX Cold Side Outlet	100.1	48.65	44.34	6.941	1.231

Table **Error! No text of specified style in document.**.22. Reversed Brayton Cycle Results

Continued

Mission Two Segment Five, Cruise In						
State	**Description**	**P (kPa)**	**T (oC)**	**h (kJ/kg)**	**s (kJ/kg-K)**	$\dot{m}$ **(kg/s)**
0	Ambient	30.09	-16.21	-20.93	7.060	0
1	Bleed Air Valve Inlet	1216	513.4	529.5	7.151	0.5923
2	Bleed Air Valve Outlet	441.0	513.4	529.5	7.442	0.5923
3	PHX Inlet	371.4	513.4	529.5	7.492	0.5923
4	PHX Outlet	323.6	79.27	75.22	6.694	0.5923
5	Compressor Inlet	309.6	79.28	75.22	6.707	0.5923
6	Compressor Outlet	888.5	237.8	236.7	6.782	0.5920
7	SHX Inlet	880.8	237.7	236.6	6.785	0.5923
8	SHX Outlet	849.6	40.83	36.45	6.297	0.5923
9	RHX Hot Side Inlet	849.6	40.83	36.45	6.297	0.2427
10	RHX Hot Side Outlet	848.2	-59.40	-64.40	5.904	0.2427
11	CHX Hot Side Inlet	848.2	-59.41	-64.40	5.904	0.2427
12	CHX Hot Side Outlet	848.1	-100.9	-106.2	5.678	0.2427
13	RHX Cold Side Inlet	848.1	-100.9	-106.2	5.678	0.2427
14	RHX Cold Side Outlet	846.8	-0.7413	-5.373	6.154	0.2427
15	Turbine Stage 1 Inlet	842.6	23.80	19.31	6.243	0.5923
16	Turbine Stage 1 Outlet	171.1	-72.09	-77.16	6.312	0.5923
17	Turbine Stage 2 Inlet	171.1	-72.09	-77.16	6.312	0.5923
18	Turbine Stage 2 Outlet	37.94	-136.3	-142.1	6.360	0.5923
19	CHX Cold Side Inlet	37.05	-136.3	-142.1	6.367	0.5923
20	CHX Cold Side Outlet	36.65	-119.4	-124.9	6.487	0.5923
21	LHX Cold Side Inlet	36.65	-119.4	-124.9	6.487	0.5923
22	LHX Cold Side Outlet	30.09	51.65	47.36	7.296	0.5923

Table **Error! No text of specified style in document.**.22. Reversed Brayton Cycle Results Continued

Mission Two Segment Six, Loiter						
State	**Description**	**P (kPa)**	**T (oC)**	**h (kJ/kg)**	**s (kJ/kg-K)**	$\dot{m}$ **(kg/s)**
0	Ambient	43.31	-3.448	-8.099	7.004	0
1	Bleed Air Valve Inlet	472.3	281.8	282.3	7.050	0.4831
2	Bleed Air Valve Outlet	348.1	281.8	282.3	7.138	0.4831
3	PHX Inlet	310.2	281.8	282.3	7.171	0.4831
4	PHX Outlet	278.8	37.81	33.42	6.611	0.4831
5	Compressor Inlet	269.5	37.81	33.42	6.621	0.4831
6	Compressor Outlet	695.7	165.5	162.6	6.696	0.4831
7	SHX Inlet	690.1	165.5	162.6	6.698	0.4831
8	SHX Outlet	664.7	24.79	20.31	6.316	0.4831
9	RHX Hot Side Inlet	664.7	24.79	20.31	6.316	0.4470
10	RHX Hot Side Outlet	659.7	-44.18	-49.07	6.050	0.4470
11	CHX Hot Side Inlet	659.7	-44.18	-49.07	6.050	0.4470
12	CHX Hot Side Outlet	659.4	-74.43	-79.52	5.904	0.4470
13	RHX Cold Side Inlet	659.4	-74.43	-79.52	5.904	0.4470
14	RHX Cold Side Outlet	654.7	-5.474	-10.14	6.211	0.4470
15	Turbine Stage 1 Inlet	651.4	-3.212	-7.862	6.221	0.4831
16	Turbine Stage 1 Outlet	146.6	-85.66	-90.83	6.287	0.4831
17	Turbine Stage 2 Inlet	146.6	-85.66	-90.83	6.287	0.4831
18	Turbine Stage 2 Outlet	48.42	-131.4	-137.1	6.325	0.4831
19	CHX Cold Side Inlet	47.39	-131.4	-137.1	6.332	0.4831
20	CHX Cold Side Outlet	47.15	-103.6	-108.9	6.513	0.4831
21	LHX Cold Side Inlet	47.15	-103.6	-108.9	6.513	0.4831
22	LHX Cold Side Outlet	43.31	51.87	47.58	7.192	0.4831

B.5 Energy Based Analysis Results

Table **Error! No text of specified style in document.**.23. Reversed-Brayton Cycle Cooling System Fuel Penalty Breakdown

RBC, Mission 1					
Segment	$\mathbf{m_{fo,sys}}$ **(kg Fuel)**	$\mathbf{m_{fo,ram}}$ **(kg Fuel)**	$\mathbf{m_{fo,bleed}}$ **(kg Fuel)**	$\mathbf{m_{fo,pto}}$ **(kg Fuel)**	$\mathbf{m_{fo,tot}}$ **(kg fuel)**
1	0	0	15.52	0	15.52
2	2.132	8.031	21.45	0	31.62
3	0.8767	9.100	14.08	0	24.06
4	2.132	8.031	21.45	0	31.62
5	1.630	3.589	8.506	0	13.72
RBC, Mission 2					
Segment	$\mathbf{m_{fo,sys}}$ **(kg Fuel)**	$\mathbf{m_{fo,ram}}$ **(kg Fuel)**	$\mathbf{m_{fo,bleed}}$ **(kg Fuel)**	$\mathbf{m_{fo,pto}}$ **(kg Fuel)**	$\mathbf{m_{fo,tot}}$ **(kg fuel)**
1	0	0	15.52	0	15.52
2	4.511	21.60	45.39	0	71.50
3	2.507	7.949	15.54	0	26.00
4	1.057	13.32	22.15	0	36.52
5	4.511	21.60	45.39	0	71.50
6	1.729	6.332	9.317	0	17.38

B.6 Exergy Based Analysis Results

Table **Error! No text of specified style in document.**.24. Reversed Brayton Cycle System Exergy Flow Breakdown for Mission 1

Segment	**1**	**2**	**3**	**4**	**5**
$\dot{\Psi}_{\mathbf{TMS,\ in}}$ **(kW)**	117.6	296.1	496.0	296.12	114.7
$\dot{\Psi}_{\mathbf{TMS,\ Overboard}}$ **(kW)**	0.06717	5.617	-0.4380	5.617	2.785
$\dot{\Psi}_{\mathbf{Ram,\ In}}$ **(kW)**	6.431	86.91	197.8	86.91	36.86
$\dot{\Psi}_{\mathbf{Ram,\ Out}}$ **(kW)**	17.81	107.1	163.3	107.1	26.39
$\dot{\Psi}_{\mathbf{Avionics,\ Out}}$ **(kW)**	0.4186	29.84	20.80	29.84	14.07
$\dot{W}_{\mathbf{TMS,\ in}}$ **(kW)**	0	0	0	0	0
$\dot{\Psi}_{\mathbf{TMS,\ out}}$ **(kW)**	1.171	10.41	2.913	10.41	3.849
$\dot{I}_{\mathbf{TMS}}$ **(kW)**	105.4	290	549	290	133
$\eta_{ex,TMS}$ **(%)**	0.94	2.52	0.41	2.52	2.32

Table **Error! No text of specified style in document.**.25. Reversed Brayton Cycle System Exergy Flow Breakdown for Mission 2

Segment	1	2	3	4	5	6
$\dot{\Psi}_{\text{TMS, in}}$ **(kW)**	117.6	312.2	142.6	622.4	312.2	128.5
$\dot{\Psi}_{\text{TMS, Overboard}}$ **(kW)**	0.06717	4.595	3.400	0.1	4.59	2.40
$\dot{\Psi}_{\text{Ram, In}}$ **(kW)**	6.431	104.1	55.10	210	104.14	60.7
$\dot{\Psi}_{\text{Ram, Out}}$ **(kW)**	17.81	107.7	32.41	169	107.72	25.8
$\dot{\Psi}_{\text{Avionics, Out}}$ **(kW)**	0.4186	23.73	23.46	1.353	23.73	11.58
$\dot{W}_{\text{TMS, in}}$ **(kW)**	0	0	0	0	0	0
$\dot{\Psi}_{\text{TMS, out}}$ **(kW)**	1.171	6.753	9.254	3.269	6.753	2.615
$\dot{I}_{\text{TMS}}$ **(kW)**	105.4	321	176	662	321	170
$\eta_{ex,TMS}$ **(%)**	0.94	1.53	4.18	0.39	1.53	1.30

Table **Error! No text of specified style in document.**.26. Reversed- Brayton Cycle Component Performance Breakdown for Mission 1

Mission One Segment One, Ground Idle					
Component	$\dot{Q}$ **(kW)**	$\dot{W}$**(kW)**	$\dot{I}$ **(W)**	$\dot{I}$ **(%)**	η_{rev} **(%)**
Bleed Air Valve			16022	15.2	86.4
Primary Heat Exchanger	-126.19		34206	32.5	23.7
Centrifugal Compressor		50.99	10397	9.87	79.6
Secondary Heat Exchanger	-61.14		12313	11.68	5.86
Reheater Heat Exchanger	-26.42		3516	3.34	97.7
Condenser Heat Exchanger	-11.43		3123	2.96	96.6
Radial Turbine, Stage 1		-36.06	8615	8.18	80.72
Radial Turbine, Stage 2		-14.93	3698	3.51	80.15
Liquid Heat Exchanger	49.37		8602	8.16	12.58
W/S Bypass Valve & Mixing			95.91	0.0910	49.6
Duct, BAV to PHX			3196	3.03	96.9
Duct, PHX to Compressor			888.6	0.843	98.3
Duct, Compressor to SHX			314.0	0.298	99.7
Duct, Reheater to Turbine			214.2	0.203	99.7
Duct, Turbine to Condenser			176.9	0.168	98.9

105377	1

Table Error! No text of specified style in document..26. Reversed- Brayton Cycle Component Performance Breakdown for Mission 1 Continued

Mission One Segment Two, Cruise Out					
Component	$\dot{Q}$ **(kW)**	$\dot{W}$**(kW)**	$\dot{I}$ **(W)**	$\dot{I}$ **(%)**	η_{rev} **(%)**
Bleed Air Valve			33924	11.7	88.5
Primary Heat Exchanger	-247.33		108841	37.6	21.1
Centrifugal Compressor		95.77	10798	3.73	88.7
Secondary Heat Exchanger	-120.39		56598	19.5	18.9
Reheater Heat Exchanger	-24.55		5245	1.81	95.9
Condenser Heat Exchanger	-10.17		4462	1.54	95.4
Radial Turbine, Stage 1		-56.13	10128	3.50	84.7
Radial Turbine, Stage 2		-39.65	7357	2.54	84.3
Liquid Heat Exchanger	102.90		41317	14.3	27.9
W/S Bypass Valve & Mixing			468.19	0.162	50.0
Duct, BAV to PHX			7091	2.45	97.3
Duct, PHX to Compressor			1941	0.670	98.3
Duct, Compressor to SHX			367.3	0.127	99.8
Duct, Reheater to Turbine			210.8	0.0727	99.9
Duct, Turbine to Condenser			1014	0.350	97.2
			289760	1	
Mission One Segment Three, Combat					
Component	$\dot{Q}$ **(kW)**	$\dot{W}$**(kW)**	$\dot{I}$ **(W)**	$\dot{I}$ **(%)**	η_{rev} **(%)**
Bleed Air Valve			53184	9.69	89.3
Primary Heat Exchanger	-399.44		209611	38.2	2.31
Centrifugal Compressor		179.01	19921	3.63	88.9
Secondary Heat Exchanger	-218.05		127213	23.2	44.9
Reheater Heat Exchanger	-77.04		11288	2.06	97.8
Condenser Heat Exchanger	-36.33		22280	4.06	92.9
Radial Turbine, Stage 1		-104.65	20492	3.73	83.6
Radial Turbine, Stage 2		-74.36	14517	2.65	83.7
Liquid Heat Exchanger	147.69		50860	9.27	4.6
W/S Bypass Valve & Mixing			201.02	0.0366	49.8
Duct, BAV to PHX			12638	2.30	97.1
Duct, PHX to Compressor			3584	0.653	98.3
Duct, Compressor to SHX			685	0.125	99.8
Duct, Reheater to Turbine			401	0.0731	99.9
Duct, Turbine to Condenser			1932	0.352	96.8
			548808	1	

Table Error! No text of specified style in document..26. Reversed- Brayton Cycle Component Performance Breakdown for Mission 1 Continued

Mission One Segment Four, Cruise In					
Component	$\dot{Q}$ **(kW)**	$\dot{W}$**(kW)**	$\dot{I}$ **(W)**	$\dot{I}$ **(%)**	η_{rev} **(%)**
Bleed Air Valve			33924	11.7	88.5
Primary Heat Exchanger	-247.33		108841	37.6	21.1
Centrifugal Compressor		95.77	10798	3.73	88.7
Secondary Heat Exchanger	-120.39		56598	19.5	18.9
Reheater Heat Exchanger	-24.55		5245	1.81	95.9
Condenser Heat Exchanger	-10.17		4462	1.54	95.4
Radial Turbine, Stage 1		-56.13	10128	3.50	84.7
Radial Turbine, Stage 2		-39.65	7357	2.54	84.3
Liquid Heat Exchanger	102.90		41317	14.3	27.9
W/S Bypass Valve & Mixing			468	0.162	50.0
Duct, BAV to PHX			7091	2.45	97.3
Duct, PHX to Compressor			1941	0.670	98.3
Duct, Compressor to SHX			367	0.127	99.8
Duct, Reheater to Turbine			211	0.0727	99.9
Duct, Turbine to Condenser			1014	0.350	97.2
			289760	1	
Mission One Segment Five, Loiter					
Component	$\dot{Q}$ **(kW)**	$\dot{W}$**(kW)**	$\dot{I}$ **(W)**	$\dot{I}$ **(%)**	η_{rev} **(%)**
Bleed Air Valve			4138	3.12	96.4
Primary Heat Exchanger	-102.62		38966	29.4	0.12
Centrifugal Compressor		49.64	9125	6.88	81.6
Secondary Heat Exchanger	-56.39		25100	18.9	72.1
Reheater Heat Exchanger	-25.18		3688	2.78	97.9
Condenser Heat Exchanger	-10.96		3974	3.00	96.2
Radial Turbine, Stage 1		-33.41	7411	5.59	81.8
Radial Turbine, Stage 2		-16.24	3669	2.77	81.6
Liquid Heat Exchanger	66.35		19104	14.4	25.8
W/S Bypass Valve & Mixing			83	0.0630	49.7
Duct, BAV to PHX			3135	2.36	97.2
Duct, PHX to Compressor			909	0.686	98.7
Duct, Compressor to SHX			264	0.199	99.8
Duct, Reheater to Turbine			174	0.131	99.8
Duct, Turbine to Condenser			12897	9.724	58.9
			132638	1	

Table **Error! No text of specified style in document.**.27. Reversed- Brayton Cycle Component Performance Breakdown for Mission 2

Mission Two Segment One, Ground Idle					
Component	$\dot{Q}$ **(kW)**	$\dot{W}$**(kW)**	$\dot{I}$ **(W)**	$\dot{I}$ **(%)**	η_{rev} **(%)**
Bleed Air Valve			16022	15.2	86.4
Primary Heat Exchanger	-126.19		34206	32.5	23.7
Centrifugal Compressor		50.99	10397	9.87	79.6
Secondary Heat Exchanger	-61.14		12313	11.68	5.86
Reheater Heat Exchanger	-26.42		3516	3.34	97.7
Condenser Heat Exchanger	-11.43		3123	2.96	96.6
Radial Turbine, Stage 1		-36.06	8615	8.18	80.72
Radial Turbine, Stage 2		-14.93	3698	3.51	80.15
Liquid Heat Exchanger	49.37		8602	8.16	12.58
W/S Bypass Valve & Mixing			95.91	0.0910	49.6
Duct, BAV to PHX			3196	3.03	96.9
Duct, PHX to Compressor			888.6	0.843	98.3
Duct, Compressor to SHX			314.0	0.298	99.7
Duct, Reheater to Turbine			214.2	0.203	99.7
Duct, Turbine to Condenser			176.9	0.168	98.9
			105377	1	
Mission Two Segment Two, Cruise Out					
Component	$\dot{Q}$ **(kW)**	$\dot{W}$**(kW)**	$\dot{I}$ **(W)**	$\dot{I}$ **(%)**	η_{rev} **(%)**
Bleed Air Valve			44397	13.8	85.8
Primary Heat Exchanger	-269.10		125780	39.2	14.9
Centrifugal Compressor		95.60	11399	3.55	88.1
Secondary Heat Exchanger	-118.56		62772	19.6	41.4
Reheater Heat Exchanger	-24.48		5123	1.60	96.0
Condenser Heat Exchanger	-10.15		4181	1.30	95.6
Radial Turbine, Stage 1		-57.14	10523	3.28	84.4
Radial Turbine, Stage 2		-38.45	7343	2.29	84.0
Liquid Heat Exchanger	102.05		37937	11.8	23.0
W/S Bypass Valve & Mixing			471.36	0.147	50.0
Duct, BAV to PHX			7517	2.34	97.2
Duct, PHX to Compressor			1949	0.607	98.3
Duct, Compressor to SHX			382.3	0.119	99.8
Duct, Reheater to Turbine			222.8	0.0694	99.8
Duct, Turbine to Condenser			1040	0.324	97.0
			321039	1	

Table **Error! No text of specified style in document.**.27. Reversed- Brayton Cycle Component Performance Breakdown for Mission 2 Continued

Mission Two Segment Three, Loiter					
Component	$\dot{Q}$ **(kW)**	$\dot{W}$**(kW)**	$\dot{I}_t$ **(W)**	$\dot{I}$ **(%)**	η_{rev} **(%)**
Bleed Air Valve			4528	2.57	96.8
Primary Heat Exchanger	-123.86		58530	33.2	17.46
Centrifugal Compressor		70.62	10265	5.83	85.5
Secondary Heat Exchanger	-78.54		36933	21.0	61.0
Reheater Heat Exchanger	-34.36		5625	3.19	97.5
Condenser Heat Exchanger	-15.22		7629	4.33	94.6
Radial Turbine, Stage 1		-44.17	9300	5.28	82.6
Radial Turbine, Stage 2		-26.45	5890	3.34	81.8
Liquid Heat Exchanger	86.43		29521	16.76	30.0
W/S Bypass Valve & Mixing			107.03	0.0608	49.8
Duct, BAV to PHX			4862	2.76	96.5
Duct, PHX to Compressor			1508	0.856	98.2
Duct, Compressor to SHX			323.8	0.184	99.8
Duct, Reheater to Turbine			204.6	0.1162	99.8
Duct, Turbine to Condenser			874.1	0.496	97.2
			176100	1	
Mission Two Segment Four, Dash					
Component	$\dot{Q}$ **(kW)**	$\dot{W}$**(kW)**	$\dot{I}$ **(W)**	$\dot{I}$ **(%)**	η_{rev} **(%)**
Bleed Air Valve			100386	15.2	83.9
Primary Heat Exchanger	-530.26		257277	38.9	1.5
Centrifugal Compressor		209.66	27907	4.22	86.7
Secondary Heat Exchanger	-260.90		132826	20.1	51.88
Reheater Heat Exchanger	-87.88		12535	1.89	98.0
Condenser Heat Exchanger	-42.31		22840	3.45	94.0
Radial Turbine, Stage 1		-130.19	27955	4.22	82.3
Radial Turbine, Stage 2		-79.48	17223	2.60	82.2
Liquid Heat Exchanger	148.19		38363	5.80	8.1
W/S Bypass Valve & Mixing			245.2	0.0371	49.8
Duct, BAV to PHX			15868	2.40	97.0
Duct, PHX to Compressor			4185	0.632	98.3
Duct, Compressor to SHX			975.7	0.147	99.8
Duct, Reheater to Turbine			569.0	0.0860	99.8
Duct, Turbine to Condenser			2548	0.385	96.5
			661704	1	

Table **Error! No text of specified style in document.**.27. Reversed- Brayton Cycle Component Performance Breakdown for Mission 2 Continued

Mission Two Segment Five, Cruise In					
Component	$\dot{Q}$ **(kW)**	$\dot{W}$**(kW)**	$\dot{I}$ **(W)**	$\dot{I}$ **(%)**	η_{rev} **(%)**
Bleed Air Valve			44397	13.83	85.8
Primary Heat Exchanger	-269.10		125780	39.2	14.86
Centrifugal Compressor		95.60	11399	3.55	88.1
Secondary Heat Exchanger	-118.6		62772	19.6	41.4
Reheater Heat Exchanger	-24.48		5123	1.60	96.0
Condenser Heat Exchanger	-10.15		4181	1.30	95.6
Radial Turbine, Stage 1		-57.14	10523	3.28	84.4
Radial Turbine, Stage 2		-38.45	7343	2.29	84.0
Liquid Heat Exchanger	102.05		37937	11.8	23.0
W/S Bypass Valve & Mixing			471	0.1468	50.0
Duct, BAV to PHX			7517	2.34	97.2
Duct, PHX to Compressor			1949	0.607	98.3
Duct, Compressor to SHX			382	0.119	99.8
Duct, Reheater to Turbine			223	0.069	99.8
Duct, Turbine to Condenser			1040	0.324	97.0
			321039	1	
Mission Two Segment Six, Loiter					
Component	$\dot{Q}$ **(kW)**	$\dot{W}$**(kW)**	$\dot{I}$ **(W)**	$\dot{I}$ **(%)**	η_{rev} **(%)**
Bleed Air Valve			9356	5.51	92.72
Primary Heat Exchanger	-115.83		59257	34.9	33.13
Centrifugal Compressor		52.04	9796	5.76	81.17
Secondary Heat Exchanger	-58.15		35160	20.7	74.93
Reheater Heat Exchanger	-26.34		3704	2.18	97.98
Condenser Heat Exchanger	-11.49		3897	2.29	96.39
Radial Turbine, Stage 1		-35.41	7920	4.66	81.72
Radial Turbine, Stage 2		-16.62	3752	2.21	81.58
Liquid Heat Exchanger	65.73		17454	10.3	22.31
W/S Bypass Valve & Mixing			87	0.0509	49.71
Duct, BAV to PHX			3313	1.95	97.22
Duct, PHX to Compressor			925	0.544	98.70
Duct, Compressor to SHX			279	0.164	99.75
Duct, Reheater to Turbine			186	0.109	99.81
Duct, Turbine to Condenser			14864	8.746	54.12
			169949	1	

APPENDIX C. SIMPLE SYSTEM MODEL CODE AND RESULTS

C.1 Simple Reversed Brayton Cycle

```
{Atmospheric properties are set with a parameter table
  properties to be set are:

T_amb = Ambient Air Temperature in C
P_amb = Ambient Air Pressure in Pa
M_num = Mach Number
h_alt = Altitude in m

Properties are set using MIL-HDBK-310 20% Hot Day values
}

"State 1: Ambient"

M_num = 0.8                                          [-]
T_amb = 48                                           [C]
T[1] = T_amb
P_amb = 101.325                                      [kPa]
P[1] = P_amb
s[1] = entropy(AirH2O,T=T[1],r=RH_air_in,P=P[1])
h[1] = enthalpy(AirH2O,T=T[1],w=omega[1],P=P[1])
h_alt = 0                                            [m]
rho_amb = .5167                                      [kg/m^3]

"Evaporator delta not need since pinch point can be directly calculated"
"Condenser delta to ensure pinch point is above zero"
"T_pinch_real_cond = 0"

RH_air_in = .1
RH[1] = RH_air_in
omega[1]=HumRat(AirH2O,T=T_amb,r=RH_air_in,P=P_amb)

"Inlet Area"
D_inlet = 0.15                                       [m]
A_inlet = pi*D_inlet^2/4

"Ideal Gas Specific Heat Ratio"
gam = 1.4                                            [-]
"Air Gas Constant"
R = 286                                              [J/kg-C]

"State 2: Ram air"
"Total Air Property Calculations for a calorically perfect gas"
P_tot = P_amb/(1+(gam-1)/2*M_num^2)^(-gam/(gam-1))
P[2] =P_tot
T_tot_k = ((converttemp('C','K',T_amb))/(1+(gam-1)/2*M_num^2)^(-1))
T_cold_in = converttemp('K','C',T_tot_k)
T[2] = T_cold_in
omega[2] = omega[1]
s[2] = entropy(AirH2O,T=T[2],w=omega[2],P=P[2])
h[2] = enthalpy(AirH2O,T=T[2],w=omega[2],P=P[2])
RH[2] = relhum(AirH2O,T=T[2],w=omega[2],P=P[2])

{rho_tot = rho_amb/(1+(gam-1)/2*M_num^2)^(-1/(gam-1))}
m_dot_air_calc = convert('kPa','Pa')*A_inlet*P_tot/sqrt(T_tot_k) * sqrt(gam/R)*M_num*(1+(gam-1)/2*M_num^2)^(-(gam+1)/(2*
(gam-1)))
"Assume ejector usage if airspeed is too low"
m_dot_air_in = IF(M_num, 0.3, 5 [kg/s], 5 [kg/s], m_dot_air_calc)
m_dot_ram_total = m_dot_air_in*2

"State 3: Bleed Air Valve Outlet"
"Pressure Ratio"
Pr = 20
"Bleed air conditions"
P_bleed = P_tot*Pr
```

```
T_bleed_k = T_tot_k*Pr^((gam-1)/gam)
T_bleed = converttemp('K','C',T_bleed_k)
T[3] = T_bleed
P_reg = 125                                          [Psi]
{P_reg = 150                                         [Psi]}
P[3] = P_reg*convert('Psi','kPa')
omega[3] = omega[2]
s[3] = entropy(AirH2O,T=T[3],w=omega[3],P=P[3])
h[3] = enthalpy(AirH2O,T=T[3],w=omega[3],P=P[3])
RH[3] = relhum(AirH2O,T=T[3],w=omega[3],P=P[3])
W_dot_eng = m_dot_bleed*(h[3] - h[2])


"State 4: Primary heat exchanger Outlet"
C_p_ram = cp('AirH2O',T = T[2], P = P[2], W = omega[1])
C_p_bleed = cp('AirH2O',T = T[3], P = P[3], W = omega[3])
C_min = min(m_dot_bleed*C_p_bleed,m_dot_air_in*C_p_ram)
epsilon_PHX = 0.8
Q_PHX = epsilon_PHX*C_min*(T[2] - T[3])
T[4] = T[3] +Q_PHX/(m_dot_bleed*C_p_bleed)
P[4] = P[3]
omega[4] = omega[3]
s[4] = entropy(AirH2O,T=T[4],w=omega[4],P=P[4])
h[4] = enthalpy(AirH2O,T=T[4],w=omega[4],P=P[4])
RH[4] = relhum(AirH2O,T=T[4],w=omega[4],P=P[4])

"State 5: Air Compressor Outlet"
eta_c = 0.8                                          [-]
"P_r_comp = 5"
P[5] = P[4]*P_r_comp
T_5_s_k = converttemp('C','K',T[4])*P_r_comp^((gam-1)/gam)
T_5_s = converttemp('K','C',T_5_s_k)
h_5_s = enthalpy(AirH2O,T=T_5_s,P = P[5], w=omega[5])
eta_c = (h_5_s - h[4])/(h[5] - h[4])
omega[5] = omega[4]
T[5] = Temperature(AirH2O,h=h[5],w=omega[5],P=P[5])
s[5] = entropy(AirH2O,h=h[5],w=omega[5],P=P[5])
RH[5] = relhum(AirH2O,T=T[5],w=omega[5],P=P[5])
W_dot_comp = m_dot_bleed*(h[5] - h[4])

"State 6: Secondary Heat Exchanger Outlet"
C_p_bleed_shx = cp('AirH2O',T = T[5], P = P[5], W = omega[5])
C_min_shx = min(m_dot_bleed*C_p_bleed_shx,m_dot_air_in*C_p_ram)
epsilon_SHX = 0.8
Q_SHX = epsilon_SHX*C_min*(T[2] - T[5])
T[6] = T[5] +Q_SHX/(m_dot_bleed*C_p_bleed_shx)
P[6] = P[5]
omega[6] = omega[5]
s[6] = entropy(AirH2O,T=T[6],w=omega[6],P=P[6])
h[6] = enthalpy(AirH2O,T=T[6],w=omega[6],P=P[6])
RH[6] = relhum(AirH2O,T=T[6],w=omega[6],P=P[6])
DP_pre = DewPoint(AirH2O,T=T[6],w=omega[6],P=P[6])

"Reheater"

"Condenser"

"Water separator"
eff_ws = 0.9
omega[7] = omega[6]*(1-eff_ws)
DP_post = DewPoint(AirH2O,T=T[6],w=omega[7],P=P[6])

"State 7: Turbine Outlet"
eta_t = 0.8                                          [-]
```

```
"P_r_turb = 10"
P[7] = P[6]/P_r_turb
T_7_s_k = converttemp('C','K',T[6])/P_r_turb^((gam-1)/gam)
T_7_s = converttemp('K','C',T_7_s_k)
h_7_s = enthalpy(AirH2O,T=T_7_s,P = P[7], w=omega[7])
eta_t = (h[7] - h[6])/(h_7_s - h[6])
T[7] = Temperature(AirH2O,h=h[7],w=omega[7],P=P[7])
s[7] = entropy(AirH2O,h=h[7],w=omega[7],P=P[7])
{DP_turb_out = DewPoint(AirH2O,T=T[7],w=omega[7],P=P[7])}
C_p_t = cp('AirH2O',T = T[7], P = P[7], W = omega[7])
W_dot_turb = m_dot_bleed*(h[7] - h[6])

P[7] = 100                                              [kPa]

W_dot_balance = -W_dot_turb/W_dot_comp
W_dot_balance = 1

T_elec_max = 55                                         [C]
Q_cooling = m_dot_bleed*C_p_t*(T_elec_max - T[7])
m_dot_bleed = 1.354                                     [kg/s]
COP = Q_cooling/W_dot_eng
```

SOLUTION

Unit Settings: SI C kPa kJ mass deg

A_{inlet} = 0.01767 [m^2]	COP = 0.2114
C_{min} = 1.524 [kW/C]	$C_{min,shx}$ = 1.462 [kW/C]
$C_{p,bleed}$ = 1.126 [kJ/kg-C]	$C_{p,bleed,shx}$ = 1.08 [kJ/kg-C]
$C_{p,ram}$ = 1.022 [kJ/kg-K]	$C_{p,t}$ = 1.004 [kJ/kg-K]
DP_{post} = 22.69 [C]	DP_{pre} = 66.96 [C]
D_{inlet} = 0.15 [m]	eff_{ws} = 0.9
ε_{PHX} = 0.8	ε_{SHX} = 0.8
η_c = 0.8 [-]	η_t = 0.8 [-]
gam = 1.4 [-]	$h_{s,s}$ = 379.4 [kJ/kg]
$h_{7,s}$ = -107.1 [kJ/kg]	h_{alt} = 0 [m]
$\dot{m}_{air,calc}$ = 5.593 [kg/s] {739.8 [lbm/min]}	$\dot{m}_{air,in}$ = 5.593 [kg/s]
$\dot{m}_{bleed}$ = 1.354 [kg/s] {179.1 [lbm/min]}	$\dot{m}_{ram,total}$ = 11.19 [kg/s] {1480 [lbm/min]}
M_{num} = 0.8 [-]	Pr = 20
P_{amb} = 101.3 [kPa]	P_{bleed} = 3089 [kPa] {448 [Psi]}
P_{reg} = 125 [psi] {861.8 [kPa]}	$P_{r,comp}$ = 2.873
$P_{r,turb}$ = 24.76	P_{tot} = 154.5 [kPa] {22.4 [Psi]}
$Q_{cooling}$ = 150 [kW]	Q_{PHX} = -597.8 [kW]
Q_{SHX} = -365.4 [kW]	R = 286 [J/kg-C]
ρ_{amb} = 0.5167 [kg/m^3]	$RH_{air,in}$ = 0.1
$T_{5,s}$ = 349.2 [C]	$T_{5,s,k}$ = 622.3 [K]
$T_{7,s}$ = -108.4 [C]	$T_{7,s,k}$ = 164.7 [K]
T_{amb} = 48 [C]	T_{bleed} = 579.4 [C] {1075 [F]}
$T_{bleed,k}$ = 852.6 [K]	$T_{cold,in}$ = 89.11 [C]
$T_{elec,max}$ = 55 [C]	$T_{tot,k}$ = 362.3 [K]
$\dot{W}_{balance}$ = 1	$\dot{W}_{comp}$ = 288.4 [kW]
$\dot{W}_{eng}$ = 709.6 [kW]	$\dot{W}_{turb}$ = -288.4 [kW]

No unit problems were detected.

EES suggested units (shown in purple) for A_inlet C_p_ram C_p_t DP_post DP_pre h[1] .

Arrays Table: Main

	P_i [kPa]	T_i [C]	h_i [kJ/kg]	s_i [kJ/kg-K]	RH_i	ω_i
1	101.3	48	66.19	5.837	0.1	0.006936
2	154.5	89.11	108.1	5.838	0.02511	0.006936
3	861.8	579.4	632.2	6.247	0.009515	0.006936
4	861.8	187.2	209	5.585	0.00806	0.006936
5	2476	388.8	422	5.662	0.02734	0.006936
6	2476	138.9	159.2	5.164	0.07798	0.006936
7	100	-55.38	-53.88	5.353		0.0006936

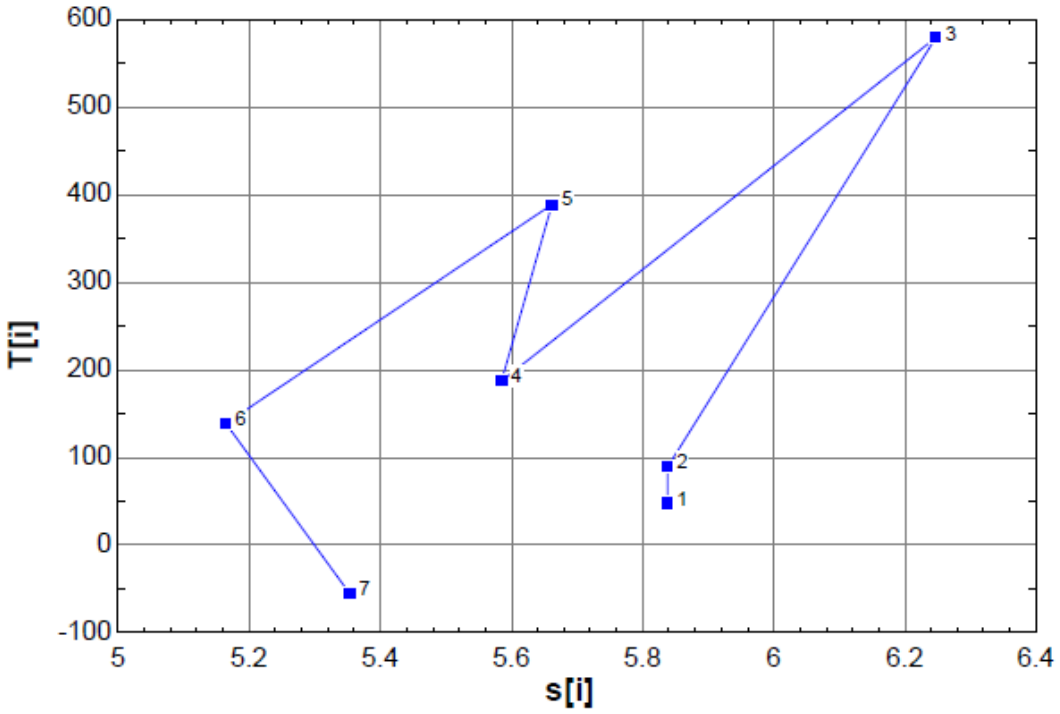

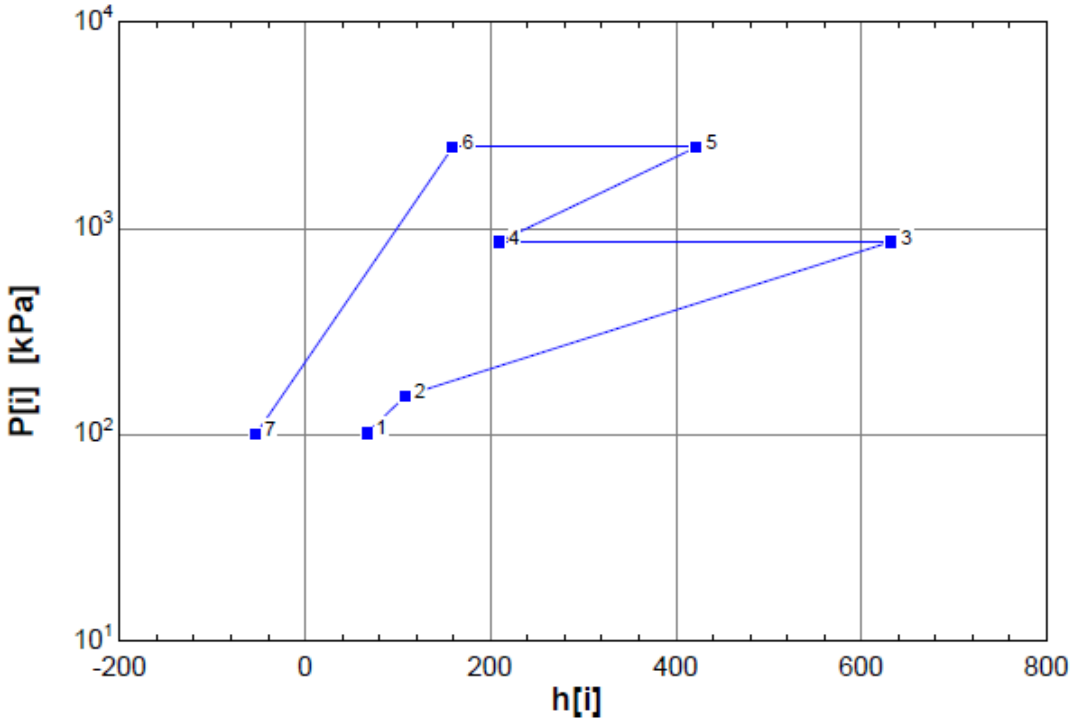
10^4
10^3
10^2
10^1
P[i] [kPa]
-200
0
200
400
600
800
h[i]
1
2
3
4
5
6
7

C.2 Simple Vapor Compressor Cycle

```
{R$ = 'R1233zd(E)'}
R$ = 'R134a'

{T_cond = 80}
T_cond = T_air_in + DELTAT_subcool + DELTAT_air
T_evap = T_cool_out - DELTAT_superheat - DELTAT_cool
{T_evap = 2.5}
T_crit =T_crit(R$)
P_crit = P_crit(R$)
T_margin = T_crit - T_cond
"Operational parameters of refrigeration system"
P_cond = P_sat(R$, T = T_cond)
P_r_1 = 4
P[3] = P_cond
P[2] = P_int
P[4] = P[3]
P_evap =  P_sat(R$, T = T_evap)
P[1] = P_evap
P[5] = P[1]
P_r_1 = P[2]/P[1]
P_r_2 = P[3]/P[2]
"State 1: Evaporator Outlet/Compressor Stage 1 Inlet"
DELTAT_superheat = 10
T[1] = T_evap + DELTAT_superheat
s[1] = entropy(R$, P = P[1], T = T[1])
h[1] = enthalpy(R$, P = P[1], T = T[1])
rho_suction = density(R$, P = P[1], T = T[1])
X[1] = 1
"State 2: Compressor Stage 1 Outlet/Compressor Stage 2 Inlet"
s_s[2] = s[1]
h_s[2] = enthalpy(R$, P = P[2], s = s_s[2])
eta_comp = 0.7
eta_comp = (h_s[2] - h[1])/(h[2] - h[1])
T[2] = Temperature(R$,P = P[2], h = h[2])
s[2] = entropy(R$,P = P[2], h = h[2])
DELTAh_comp_1 = h[2] - h[1]
X[2] = 1
"State 3: Compressor Stage 2 Outlet/Condenser Inlet"
s_s[3] = s[2]
h_s[3] = enthalpy(R$, P = P[3], s = s_s[3])
eta_comp = (h_s[3] - h[2])/(h[3] - h[2])
T[3] = Temperature(R$,P = P[3], h = h[3])
s[3] = entropy(R$,P = P[3], h = h[3])
X[3] = 1
DELTAh_comp_2 = h[3] - h[2]
T_air_in = 70
P_air_in = 101.325                                          [kPa]
DELTAT_air = 20
Cp_air = Cp(AirH2O,T=T_air_in,r=0.03,P=P_air_in)
epsilon_cond = 0.9
Q_dot_h = epsilon_cond*m_dot_air*Cp_air*(T_air_in - T_cond)
"State 4: Condenser Outlet/Expansion Valve Inlet"
DELTAT_subcool = 5
T[4] = T_cond - DELTAT_subcool
h[4] = enthalpy(R$, P = P[4], T = T[4])
s[4] = entropy(R$,P = P[4], h = h[4])
X[4] = 0
"State 5: Expansion Valve Outlet/Evaporator Inlet"
h[5] = h[4]
T[5] = Temperature(R$,P = P[5], h = h[5])
s[5] = entropy(R$,P = P[5], h = h[5])
X[5] = quality(R$, P=P[5], h = h[5])
Cp_ref_tp = Cp(R$,P = P[5],x = 0)*(1-x[5]) + Cp(R$,P = P[5],x = 1)*(x[5])
```

```
DELTAh_evap = h[1] - h[5]
{DELTAh_evapcomp = DELTAh_evap/DELTAh_comp}
Q_dot_L = 150                                                    [kW]
Q_dot_L = m_dot_r*DELTAh_evap
Q_dot_h = m_dot_r*(h[4] - h[3])
W_dot_1 = m_dot_r*DELTAh_comp_1
W_dot_2 = m_dot_r*DELTAh_comp_2
W_dot = W_dot_1 + W_dot_2
COP = Q_dot_L/W_dot
Balance = W_dot + Q_dot_L + Q_dot_h
" Coolant Side"
DELTAT_cool = 5                                                  [C]
C = 60                                                           [%]
C$ = 'EG'
T_cool_in = 55                                                   [C]
T_cool_out = 20 {T_evap + DELTAT_superheat + DELTAT_cool}
Cp_cool = Cp(C$,T = T_cool_out,C = C)
rho_cool = density(C$,T = T_cool_out,C = C)
Q_dot_L = m_dot_cool*Cp_cool*(T_cool_in - T_cool_out)
C_min_L = min(m_dot_cool*Cp_cool,m_dot_r*Cp_ref_tp)
Q_dot_L = epsilon_evap*(m_dot_cool*Cp_cool)*(T_cool_in - T_evap)
m_dot_cool = rho_cool*V_dot_cool

Duplicate j = 1,3
T_all[j] = T[j]
P_all[j] = P[j]
h_all[j] = h[j]
s_all[j] = s[j]
X_all[j] = X[j]
end

X_all[4] = 1
P_all[4] = P_all[3]
T_all[4] = T_sat(R$,P=P_all[4])
s_all[4] = entropy(R$,P=P_all[4],x=X_all[4])
h_all[4] = enthalpy(R$,P=P_all[4],x=X_all[4])

X_all[5] = 0
P_all[5] = P_all[3]
T_all[5] = T_sat(R$,P=P_all[5])
s_all[5] = entropy(R$,P=P_all[5],x=X_all[5])
h_all[5] = enthalpy(R$,P=P_all[5],x=X_all[5])

Duplicate j = 6,7
T_all[j] = T[j-2]
P_all[j] = P[j-2]
h_all[j] = h[j-2]
s_all[j] = s[j-2]
X_all[j] = X[j-2]
end

X_all[8] = 1
P_all[8] = P_all[7]
T_all[8] = T_sat(R$,P=P_all[8])
s_all[8] = entropy(R$,P=P_all[8],x=X_all[8])
h_all[8] = enthalpy(R$,P=P_all[8],x=X_all[8])

T_all[9] = T_all[1]
P_all[9] = P_all[1]
h_all[9] = h_all[1]
s_all[9] = s_all[1]
X_all[9] = X_all[1]
```

SOLUTION

Unit Settings: SI C kPa kJ mass deg

Balance = 0 [kW]
C$ = 'EG'
$C_{p,air}$ = 1.018 [kJ/kg-K]
$C_{p,ref,tp}$ = 1.056 [kJ/kg-K]
$\Delta h_{comp,1}$ = 43.48 [kJ/kg]
Δh_{evap} = 69.8 [kJ/kg]
ΔT_{cool} = 5 [C]
$\Delta T_{superheat}$ = 10 [C]
ε_{evap} = 0.7
$\dot{m}_{air}$ = 13.53 [kg/s] {1790 [lbm/min]}
$\dot{m}_{r}$ = 2.149 [kg/s]
P_{cond} = 3594 [kPa] {35.94 [Bar]}
P_{evap} = 349.9 [kPa] {3.499 [Bar]}
$P_{r,1}$ = 4
$\dot{Q}_{h}$ = -310 [kW]
R$ = 'R134a'
$\rho_{suction}$ = 16.3 [kg/m^3]
T_{cond} = 95 [C]
$T_{cool,out}$ = 20 [C]
T_{evap} = 5 [C]
$\dot{V}_{cool}$ = 0.001284 [m^3/s] {20.36 [Gal/min]}
$\dot{W}_{1}$ = 93.44 [kJ/s]

C = 60 [%]
COP = 0.9376
$C_{p,cool}$ = 3.098 [kJ/kg-K]
$C_{min,L}$ = 2.27 [kJ/s-K]
$\Delta h_{comp,2}$ = 30.97 [kJ/kg]
ΔT_{air} = 20 [C]
$\Delta T_{subcool}$ = 5 [C]
ε_{cond} = 0.9
η_{comp} = 0.7
$\dot{m}_{cool}$ = 1.383 [kg/s]
$P_{air,in}$ = 101.3 [kPa]
P_{crit} = 4059 [kPa] {40.59 [Bar]}
P_{int} = 1400 [kPa]
$P_{r,2}$ = 2.568
$\dot{Q}_{L}$ = 150 [kW]
ρ_{cool} = 1077 [kg/m^3]
$T_{air,in}$ = 70 [C]
$T_{cool,in}$ = 55 [C]
T_{crit} = 101 [C]
T_{margin} = 6.03 [C]
$\dot{W}$ = 160 [kW]
$\dot{W}_{2}$ = 66.55 [kJ/s]

No unit problems were detected.
EES suggested units (shown in purple) for Balance Cp_air Cp_ref_tp C_min_L DELTAh_comp_1 DELTAh_comp_2 .

Arrays Table: Main

	h_{l} [kJ/kg]	$h_{s,l}$ [kJ/kg]	P_{l} [kPa]	s_{l} [kJ/kg-K]	$s_{s,l}$ [kJ/kg-K]	T_{l} [C]	X_{l}	$P_{all,l}$ [kPa]	$T_{all,l}$ [C]	$X_{all,l}$	$h_{all,l}$ [kJ/kg]
1	262.5		349.9	0.961		15	1	349.9	15	1	262.5
2	305.9	292.9	1400	0.9988	0.961	77.84	1	1400	77.84	1	305.9
3	336.9	327.6	3594	1.022	0.9988	128.8	1	3594	128.8	1	336.9
4	192.7		3594	0.6365		90	0	3594	95	1	272.3
5	192.7		349.9	0.7106		5	0.6884	3594	95	0	207.1
6								3594	90	0	192.7
7								349.9	5	0.6884	192.7
8								349.9	5	1	253.3
9								349.9	15	1	262.5

Arrays Table: Main

	$s_{all,l}$ [kJ/kg-K]
1	0.961
2	0.9988
3	1.022
4	0.8529
5	0.6758
6	0.6365
7	0.7106
8	0.9288

Arrays Table: Main

	$s_{all,i}$ [kJ/kg-K]
9	0.961

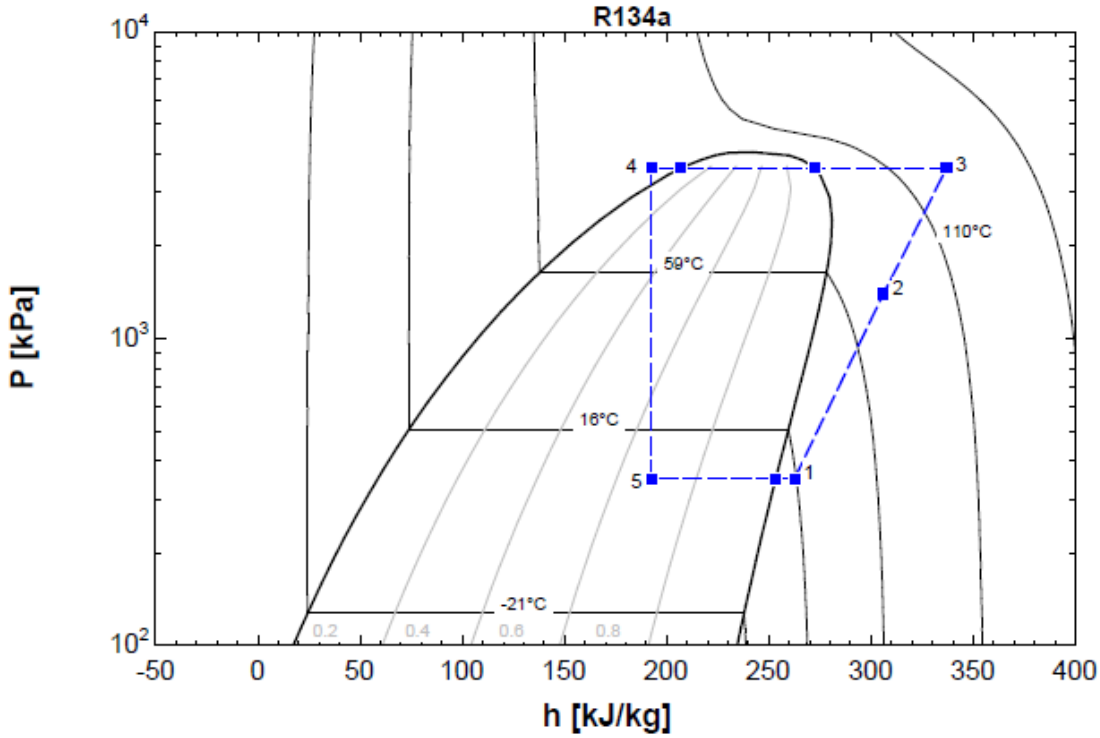

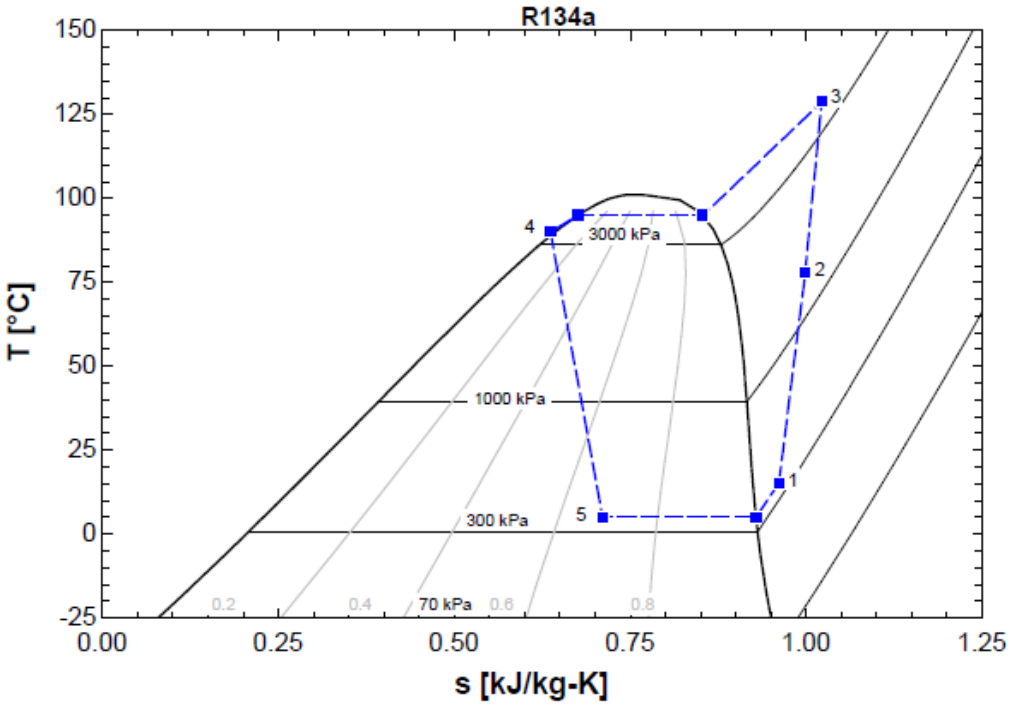
R134a
T [°C]
s [kJ/kg-K]
150
125
100
75
50
25
0
-25
0.00
0.25
0.50
0.75
1.00
1.25
3000 kPa
1000 kPa
300 kPa
70 kPa
0.2
0.4
0.6
0.8
1
2
3
4
5

REFERENCES

[1] T. Mahefkey, K. Yerkes, B. Donovan and M. L. Ramalingam, "Thermal Management Challenges For Future Military Aircraft Power Systems," in *Power Systems Conference*, Reno, 2004.

[2] J. Homitz, R. Scaringe and G. Cole, "SAE 2010-01-1733: Evaluation of a Vapor-Compression Thermal Management System for Reliability While Operating Under Thermal Transients," in *Aircraft Thermal Management - Systems Architectures*, SAE International, 2010, p. Chapter 10.

[3] R. B. Barta, J. J. Hugenroth and E. A. Groll, "Modeling of S-RAM Energy Recover Compressor Integration in a Transcritical Carbon Dioxide Cycle for Application in Electronics Cooling in Varying Gravity," in *17th International Refrigeration and Air Conditioning Conference at Purdue*, West Lafayette, 2018.

[4] J. Homitz, R. P. Scaringe, G. S. Cole, A. Fleming and T. Michalak, "SAE 2008-01-2905: Comparative Analysis of Thermal Management Architectures to Address Evolving Thermal Requirements of Aircraft Systems," in *Aircraft Thermal Management - Systems Architectures*, SAE International, 2008.

[5] Kollmorgen, "The Trend Towards Increasing Use of Electrical Actuators in the Aerospace and Defense Industry," Kollmorgen Corporation, Radford, 2015.

[6] T. W. Lovell, D. Zielke and S. L. Benning, "Augmented Avionics Cooling for Existing Aircraft," in *26th International Conference on Environmental Systems*, Monterey, 1996.

[7] DoD, "MIL-HDBK-5400: GENERAL GUIDELINES FOR ELECTRONIC EQUIPMENT, AIRBORNE," Department of Defense, 1995.

[8] AFRL/VSBE, "MIL-HDBK-310 - GLOBAL CLIMATIC DATA FOR DEVELOPING MILITARY PRODUCTS," Department of Defense, Hanscom AFB, 1997.

[9] R. P. Scaringe and L. R. Grzyll, "The Heat Pump Thermal Bus – An Alternative to Pumped Coolant Loops," in *Aerospace Power Systems Conference*, Mesa, 1999.

[10] O. Altim and S. Eser, "Carbon Deposit Formation from Thermal Stressing of Petroleum Fuels," *Am. Chem. Soc., Div. Fuel Chem.*, pp. 764-766, 2004.

[11] S. Klein, "Engineering Equation Solver [computer software]," F-Chart Software., 2019.

[12] SAE Committee AC-9, "Part 3B. Refrigeration System Design," in *SAE Aerospace Applied Thermodynamics Manual*, New York, SAE, Inc., 1969.

[13] Trane, "Considerations for Next Generation HVAC Refrigerants," Ingersoll Rand, 2015.

[14] Aircraft Systems Tech, "Aircraft Air Conditioning Systems," 2019. [Online]. Available: https://www.aircraftsystemstech.com/2017/05/vapor-cycle-air-conditioning-system.html. [Accessed 1 October 2019].

[15] R. C. Arora and M. Ramgopal, "Refrigeration and Air Conditioning," NPTEL, Kharagpur, 2009.

[16] SAE, "SAE AIR AIR1168/8 - Aircraft Fuel Weight Penalty Due to Air Conditioning," SAE Aerospace, Warrendale, 2011.

[17] A. B. Evans, "The Effects of Compressor Seventh-Stage Bleed Air Extraction on Performance of the F100-PW-220 Afterburning Turbofan Engine," NASA, Edwards, 1991.

[18] R. S. Figliola, R. Tipton and H. Li, "Exergy Approach to Decision-Based Design of Integrated Aircraft Thermal Systems," *Jorunal of Aircraft*, pp. Vol. 40, No.1, January-Feburary 2003.

[19] S. de Oliveira, Jr., "Exergy Method for Conception and Assessment of Aircraft Systems," in *Exergy - Production, Cost and Renewability*, London, Springer, 2013, pp. 265-280.

[20] L. F. Pellegrini, R. Gandolfi, G. Araújo Lima da Silva and S. de Oliveira, Jr., "Exergy Analysis as a Tool for Decision Making in Aircraft Systems Design," in *45th AIAA Aerospace Sciences Meeting and Exhibit*, Reno, 2007.

[21] C. Tona, P. Antonio Raviolo, L. Felipe Pellegrini and S. de Oliveira, "Exergy and thermoeconomic analysis of a turbofan engine during a typical commercial flight," *Energy 35*, pp. 952-959, 2010.

[22] V. Patel, M. Koerner and D. Loeffelholz, *Thermal Management and Power Generation for Directed Energy Weapons*, SAE Technical Paper 2010-01-1781, 2010.

[23] D. Scholz, R. Seresinhe, I. Staack and C. Lawson, "Fuel Consumption Due to Shaft Power Off-Takes from the Engine," in *Workshop on Aircraft System Technologies*, Hamburg, 2013.

[24] W. Chen, D. W. Fogg, M. Izenson and C. Kurwitz, "SAE 2012-01-2186: A Highly Stable Two-Phase Thermal Management System for Aircraft," SAE International, 2012.

[25] C. W. Lui, C. K. Lee and E. Schwan, "Integrated Environmental Control System and Liquid Cooling System for F/A-18 E/F Aircraft," in *1995 SAE Aerospace Atlantic Conference & Exposition*, Dayton, 1995.

[26] R. H. Zimmerman and W. Robinson, "Equipment Cooling Systems for Aircraft," The Ohio State University Research Foundation, 1954.

[27] E. Groll, *ME518 Class Notes,* West Lafayette, 2018.

[28] M. Kania, J. Koeln, A. Alleyne, K. McCarthy, N. Wu and S. Patnaik, "SAE 2012-01-2172: A Dynamic Modeling Toolbox for Air Vehicle Vapor Cycle Systems," SAE International, 2012.

[29] P. McCarthy, N. Niedbalski, K. McCarthy, E. Walters, J. Cory and S. Patnaik, "SAE 2016-01-1995: A First Principles Based Approach for Dynamic Modeling of Turbomachinery," SAE International, 2016.

[30] PC Krause, "ATTMO Toolset [computer software]," PC Krause and Associates, West Lafayette, 2019.

[31] T. Benson, "Isentropic Flow," 12 June 2014. [Online]. Available: https://www.grc.nasa.gov/www/BGH/isentrop.html. [Accessed 24 September 2019].

[32] D. P. Raymer, Aircraft Design: A Conceptual Approach, Washington, D.C.: American Institute of Aeronautics and Astronautics, 1992.

[33] E. A. Haering, Jr. and F. W. Burchman, Jr., "Minimum Time and Fuel Flight Profiles for an F-15 Airplane with a Highly Integrated Digital Electronic Control System," NASA, Edwards, 1986.

[34] T. Benson, "Mass Flow Choking," 12 June 2014. [Online]. Available: https://www.grc.nasa.gov/www/BGH/mflchk.html. [Accessed 24 September 2019].

[35] DOW, "DOWTHERM SR-1 Heat Transfer Fluid," The Dow Chemical Company, 2008.

[36] E. B. I. H. M. M. M. Lemmon, *NIST Standard Reference Database 23: Reference Fluid Thermodynamic and Transport Properties-REFPROP, Version 10.0,* Gaithersburg: National Institute of Standards and Technology, 2018.

[37] SAE COMMITTEE AC-9, "ARP731: General Requirements for Application of Vapor Cycle," SAE International, 2015.

[38] L. van Bommel, "Thermodynamic Model of a Screw Compressor," Delft University of Technology, 2016.

[39] N. Seshaiah, S. K. Ghosh, R. K. Sahoo and S. K. Sarangi, "Mathematical modeling of the working cycle of oil injected rotary twin screw compressor," *Applied Thermal Engineering*, no. 27, pp. 145-155, 2007.

[40] Howden Compressors, *Rotary Twin Screw Compressors,* Glasgow: Anderson Group Inc., 2014.

[41] Danfoss, "Brazed Plate Heat Exchanger Type PHE," Danfoss, 2009.

[42] J. R. Garcia-Cascales, F. Vera-Garcia, J. M. Corberan-Salvador and J. Gonzalvez-Macia, "Assessment of boilng and condensation heat transfer correlations in the modeling of plate heat exchangers," *International Journal of Refrigeration,* vol. 2007, pp. 1029-1041, 2007.

[43] Y.-Y. Yan, H.-C. Lio and T.-F. Lin, "Condensation heat transfer and pressure drop of refrigerant R-134a in a plate heat exchanger," *International Journal of Heat and Mass Transfer,* vol. 42, pp. 993-1006, 1999.

[44] R. M. Manglik and A. E. Bergles, "Heat Transfer and Pressure Drop Correlations for the Rectangular Offset Strip Fin Compact Heat Exchanger," *Experimental Thermal and Fluid Science,* vol. 10, pp. 171-180, 1995.

[45] M. K. Dobson and J. C. Chato, "Condensation in Smooth Horizantal Tubes," *Journal of Heat Transfer,* vol. 120, no. 2, pp. 193-213, 1998.

[46] J. e. a. Wattelet, "Heat transfer flow regimes of refrigerants in a horizontal-tube evaporator," University of Illinois at Urbana-Champaign, ACRC TR-55, 1994.

[47] B. R. Munson, D. F. Young and T. H. Okiishi, Fundamentals of Fluid Mechanics, Wiley, 1990.

[48] G. L. DeFrancesco, "SAE 932056: Condensing Cycle Air Conditioning System," *SAE Transactions,* vol. 102, no. SECTION 1: JOURNAL OF AEROSPACE, pp. 633-638, 1993.

[49] IHS Markit, "Pratt & Whitney F100," *Jane's Aero-Engines,* pp. 1-9, 25 July 2018.

[50] L. S. Ismail, C. Ranganayakulu, P. S. Reddy, D. Jyotsna and V. V. Rao, "Heat Transfer and Flow Friction correlations for Compact Wavy Plate Fin Heat Exchangers," in *19th National 8th ISHMT ASME HMT Conference*, 2008.

[51] M. R. Galvas, "Fortran Program for Predicting Off-Design Performance of Centrifugal Compressors," NASA Technical Note: NASA TN, Washington D.C., 1973.

[52] P. L. Hale, "A Method To Estimate Weight and Dimensions of Small Aircraft Propulsion Gas Turbine Engines," Garret Turbine Engine Company, 1982.

[53] C. Xu and R. S. Amano, "Empirical Design Considerations for Industrial Centrifugal Compressors," *International Journal of Rotating Machinery,* vol. 2012, p. 15, 2012.

[54] P. a. G. A. Meitner, "Computer Code for Off-Design Performance Analysis of Radial-Inflow Turbines With Rotor Blade Sweep," NASA Technical Paper 2199, AVRADCOM Technical Report, Cleveland, 1983.

[55] W. J. Godecker, J. C. Lentz, C. B. Parme, D. B. Wigmore and K. B. Winans, "Vapor Cycle System for a Fighter Aircraft - The Lantirn ECU Lessons Learned," *SAE Transactions,* Vols. 101, SECTION 1: JOURNAL OF AEROSPACE, pp. 609-617, 1992.

[56] G. A. Longo, "Heat Transfer and Pressure Drop During HC-600a (Isobutane) Condensation Inside a Brazed Plate Heat Exchanger," in *International Refrigeration and Air Conditioning Conference*, 2008.